MORPHOLOGICALLY SIMPLIFIED CONDUCTANCE BASED NEURON MODELS: PRINCIPLES OF CONSTRUCTION AND USE IN PARAMETER OPTIMIZATION

A Dissertation

Presented to

The Academic Faculty

By

Eric B. Hendrickson

In Partial Fulfillment

Of the Requirements for the Degree

Doctor of Philosophy in the School of Biomedical Engineering

Georgia Institute of Technology / Emory University

May 2010

MORPHOLOGICALLY SIMPLIFIED CONDUCTANCE BASED NEURON MODELS: PRINCIPLES OF CONSTRUCTION AND USE IN PARAMETER OPTIMIZATION

Approved by:

Dr. Dieter Jaeger, Advisor

Department of Biology

Emory University

Dr. Ronald Calabrese

Department of Biology

Emory University

Dr. Robert Butera

School of Electrical and Computer Engineering

Georgia Institute of Technology

Dr. Robert H. Lee

Department of Biomedical Engineering

Georgia Institute of Technology / Emory University

Dr. Astrid Prinz

Department of Biology

Emory University

Dr. Yoland Smith

Department of Neurology

Emory University

Date Approved: March 23rd, 2010

ACKNOWLEDGMENTS

First, I want to thank my family and friends for their support which has allowed me to devote almost five years of my life to science.

I also want to thank:

1. Dieter Jaeger for being such a careful scientist and supportive advisor. I am a much stronger scientist and writer today than I was four years ago because of his constructive criticism and encouragement.
2. Jeremy Edgerton for being an awesome collaborator and a good friend. I would not be the person I am today without his advice and friendship over the last few years.
3. Astrid Prinz for sharing with me her excitement about neuroscience. I often found myself running over to her office to show her a new result, because she was never too busy to take a look at my data.
4. Ron Calabrese for sharing with me his unique insights and extensive experience in the field of neuroscience.
5. Yoland Smith for all the stimulating discussions about experimental neuroscience in and out of journal club.
6. Bob Lee for his unique perspectives on experimental and computational neuroscience. He has always encouraged me to take my analyses to the next level, often leading to interesting results.
7. Rob Butera for his encouragement and his advice to stay focused on what is biologically important.

8. The basal ganglia journal club (Thomas, Adriana, Kalynda, Claudia, Rosa, etc) for great discussions about topics I'd never considered before.
9. Other lab mates: Nathan, Cengiz, Chris, Tom, Li Su, Selva, Wafa, Jason, for helping me get up to speed when I was just starting out and bouncing ideas around with me. Also Tomasz for his invaluable help when I was just starting to learn about evolutionary algorithms.
10. My fellow PhD classmates for good times and interesting discussions in and out of class.
11. The BME program office for their consistent encouragement and help (Beth, Leita, Sally, Shannon).
12. Sorum Panchal for her invaluable support and encouragement over the last eight months. She has helped me to find the bright side of so many things, including being holed away in the lab for the last few months.

TABLE OF CONTENTS

LIST OF TABLES

LIST OF FIGURES

LIST OF SYMBOLS OR ABBREVIATIONS

GP – Globus Pallidus

HH – Hodgkin and Huxley

Cm – Specific membrane capacitance

Rm – Specific membrane resistance

Ra – Specific axial Resistance

dS – density search

sKS – selected kinetic search

iKS – ineffective kinetic search

aKS – all kinetic search

n250 – negative 250 pA somatic current injection

p17 – positive 17 pA somatic current injection

p150 – positive 150 pA somatic current injection

NaF – fast sodium channel

NaP – persistent sodium channel

Kv2 – slow activating delayed rectifier potassium channel

Kv3 – fast activating incompletely inactivating potassium channel

Kv4 – A-type low voltage activated potassium channel

Kdr – Kv2, Kv3 and Kv4 taken together channel

KCNQ – KCNQ family potassium channel

SK – calcium activated potassium channel

CaHVA – high voltage activated calcium channel

HCN – hyperpolarization activated cyclic nucleotide-gated mixed cation channel

RMSE – root mean squared error

Eleak – reversal potential of the leak conductance

(f)AHP – (fast) afterhyperpolarization

ISI – inter spike interval

fI – spike frequency vs current injection

fF – spike frequency vs frequency of synaptic input

TSA – total surface area

R_{IN} / Z_{IN} – input resistance / input impedance

(b)AP – (backpropagating) action potential

EPSP – excitatory post synaptic potential

P2P – peak to peak

Q_{EPSP} – charge transferred during an EPSP

EA – Evolutionary algorithm

SUMMARY

The dynamics of biological neural networks are of great interest to neuroscientists and are frequently studied using conductance-based compartmental neuron models. For speed and ease of use, neuron models are often reduced in morphological complexity. This reduction may affect input processing and prevent the accurate reproduction of neural dynamics. However, such effects are not yet well understood. Therefore, for my first aim I analyzed the processing capabilities of 'branched' or 'unbranched' reduced models by collapsing the dendritic tree of a morphologically realistic 'full' globus pallidus neuron model while maintaining all other model parameters. Branched models maintained the original detailed branching structure of the full model while the unbranched models did not. I found that full model responses to somatic inputs were generally preserved by both types of reduced model but that branched reduced models were better able to maintain responses to dendritic inputs. However, inputs that caused dendritic sodium spikes, for instance, could not be accurately reproduced by any reduced model. Based on my analyses, I provide recommendations on how to construct reduced models and indicate suitable applications for different levels of reduction. In particular, I recommend that unbranched reduced models be used for fast searches of parameter space given somatic input output data.

The intrinsic electrical properties of neurons depend on the modifiable behavior of their ion channels. Obtaining a quality match between recorded voltage traces and the output of a conductance based compartmental neuron model depends on accurate

estimates of the kinetic parameters of the channels in the biological neuron. Indeed, mismatches in channel kinetics may be detectable as failures to match somatic neural recordings when tuning model conductance densities. In my first aim, I showed that this is a task for which unbranched reduced models are ideally suited. Therefore, for my second aim I optimized unbranched reduced model parameters to match three experimentally characterized globus pallidus neurons by performing two stages of automated searches. In the first stage, I set conductance densities free and found that even the best matches to experimental data exhibited unavoidable problems. I hypothesized that these mismatches were due to limitations in channel model kinetics. To test this hypothesis, I performed a second stage of searches with free channel kinetics and observed decreases in the mismatches from the first stage. Additionally, some kinetic parameters consistently shifted to new values in multiple cells, suggesting the possibility for tailored improvements to channel models. Given my results and the potential for cell specific modulation of channel kinetics, I recommend that experimental kinetic data be considered as a starting point rather than as a gold standard for the development of neuron models.

CHAPTER 1: INTRODUCTION

1.1.Specific aims

1.1.1. Aim 1:

Conductance-based neuron models are frequently employed to study the dynamics of biological neural networks. For speed and ease of use, these models are often reduced in morphological complexity. However, simplified dendritic branching structures may process inputs differently than full branching structures and could thereby fail to reproduce important aspects of biological neural processing. It is not yet well understood which processing capabilities require detailed branching structures. In order to determine which aspects of processing require dendritic branching, I reduced the morphological complexity of a full morphological globus pallidus (GP) neuron model using two different strategies: one strategy preserved the branching structure and the other did not. By analyzing the capabilities of reduced models created with each reduction strategy, I was able to offer clear recommendations to modelers about the conditions in which morphological complexity and branching structure can be safely reduced.

1.1.2. Aim 2:

The intrinsic electrical properties of neurons depend on the behavior of their ion channels. The voltage and time dependence of ion channels can be regulated in many ways, for example phosphorylation. Furthermore, the proportion of phosphorylated

channels and other modulations could vary greatly between individual neurons. Consistent failure to match certain features of neural recordings with a conductance based compartmental neuron model could suggest that ion channel properties need to be optimized for that cell. Parameter variation studies often set conductance densities free while leaving channel properties fixed. Because individual cells can tightly regulate their ion channel properties, kinetic parameters may need to be set free to achieve optimal results with automated searches. Therefore, I analyzed the added benefits of optimizing kinetic parameters over the optimization of density parameters by performing automated matching of three GP neuron models to data recorded from three different cells. My analyses allow me to offer modelers both a clear understanding of the benefits of optimizing channel kinetics and hypotheses about specific changes that may need to be made to channel properties in GP neuron models.

1.2. Origins: A century old tension between realistic and tractable neuron models

Neurons can be modeled with widely varying levels of complexity. Everything from highly tractable but unrealistic 'integrate and fire' and 'black box' phenomenological models to highly realistic but much less tractable morphologically and biophysically detailed models possessing a full complement of ion channels are currently used to test different hypotheses. The hypothesis being tested should dictate what sort of model to use, but it is only recently that modelers have had such a wide range of models to choose from. For historical or other reasons, modelers may be using neuron models which are too complicated for their hypothesis and therefore less tractable as well as

more difficult to work with than necessary. More commonly, modelers may use an oversimplified model which is handicapped in its ability to uncover the real mechanisms behind neural phenomena. The tendency to use very simplified neuron models dates back to the origins of neuron modeling. Indeed, due to a lack of a detailed biophysical understanding of the mechanisms of neuronal dynamics, the first neuron models were as mathematically simple as possible. Arguably the first neuron model was the integrate and fire neuron model published by Louis Lapicque in French in 1907 (Lapicque, 1907). In brief, an integrate and fire model integrates an input signal, for instance input from other neurons, until the integral surpasses some threshold; after exceeding the threshold, the neuron fires a spike. Since Lapicque introduced his integrate and fire model, it has generated a large amount of interest due to its mathematical tractability and its ability to describe neural phenomena without worrying about precise biophysical mechanisms (Abbott, 1999). However, a mechanistic understanding of neural phenomena has always been highly desirable. This desire led to a breakthrough a full 45 years after Lapicque's presentation of his integrate and fire model in Hodgkin and Huxley's (HH's) development of their mechanistic theory for spike generation based on the interaction between voltage-gated sodium and potassium channels in the squid giant axon (Hodgkin and Huxley, 1952). Their theory revolutionized our understanding of neuronal dynamics as well as helped to create the field of mechanistic neuron modeling, because it allowed a detailed biophysical understanding of complex neural phenomena like action potentials for the first time. Interest in the field has since exploded such that HH's paper has been cited more than 8,000 times and countless other papers have undoubtedly been published for which HH's 1952 paper forms the theoretical basis. HH's work formed the core of

our current understanding of how ion channels interact to produce complex neural behaviors, but it was not until the work of Wilfrid Rall in the late 1950s to the early 1970s that a theoretical understanding of the importance of the complex geometry of neurons was developed. The fundamental papers of Rall published during this period, together cited over 3500 times, demonstrated the importance of morphology for input processing and neuronal activity (Rall, 1959, 1960, 1962, 1964, 1967, 1969; Rall and Rinzel, 1973; Goldstein and Rall, 1974). Until Rall, despite the pioneering work of Ramon y Cajal which demonstrated that neurons possessed extremely intricate dendritic morphologies (Cajal, 1911), the role played by morphology in shaping electrophysiological activity was neglected because it was poorly understood. Indeed, neurons were generally considered to be adequately modeled as small spheres with no spatial extent. Rall's work is of particular interest to me because I attempt to understand not just the interactions between inputs and different ion channels but additionally explore the even more complex interactions between inputs, channels and morphology. This type of neuron modeling is usually referred to as compartmental conductance based neuron modeling, a field which is only about 30 years old and is expanding rapidly, with very few citations before 1990, about 20 per year in the 1990s and more than 30 per year in the 2000s. It is this type of modeling that forms the basis for my thesis work in which I first describe how far morphologies can be simplified while maintaining biological dynamics and next use my simplified morphologies to match recorded dynamics in order to highlight potential deficiencies of our HH channel models.

1.3. Morphological diversity and passive properties – is morphological complexity important?

A unique feature of neurons is that processes known as dendrites emanate from their cell body, or soma. The dendritic trees of some types of neuron are relatively simple structures while in other types they can be extremely complex; for instance; cerebellar Purkinje cells have relatively short but extensively branched dendritic trees (Deschutter and Bower, 1994). In contrast, GP neurons have very long and sparsely branched dendritic trees (Yelnik et al., 1984; Kita and Kitai, 1994). The passive processing capabilities of dendrites are extremely relevant to aim 1 of my thesis because passive decay and active processing in dendritic trees can influence inputs from other neurons profoundly before they reach the soma, where (in mammals) many inputs are integrated into an action potential. Before studying the active processing capabilities of dendrites, it is useful to study dendrites lacking 'active' ion channels (an important group of membrane bound proteins that will be discussed in the next section). Indeed, passive dendrites can act both as linear lowpass filters to attenuate dendritic inputs as they travel to the soma and as a nonlinear filter which decreases the effect of two simultaneous inputs depending on their proximity to each other (London and Hausser, 2005). Due to the importance of passive properties, in my first aim I perform careful analyses of passive differences due to branching structure before adding in active ion channels.

In addition to their morphologies, the passive electrical characteristics of neurons can profoundly alter active input processing. Therefore, it is important to experimentally constrain the passive parameters of neurons as accurately as possible before studying their active properties. The passive properties of neurons depend primarily on three

factors in addition to their morphology: the ability of membrane leak channels to act as resistors to current flow into or out of the cell, the ability of the lipid membrane to act as a capacitor which can store charge, and the ability of the intracellular fluid (cytosol) to resist the flow of current within the cell. The capacitance of the lipid membrane is fairly constant between different types of neuron and has been quite well constrained experimentally (Gentet et al., 2000; Oltedal et al., 2009). The intracellular resistivity to current flow is more variable between different cell types, but is still relatively well constrained by experiments (Stuart and Spruston, 1998; Roth and Hausser, 2001; Antic, 2003; Oltedal et al., 2009). In contrast, the resistivity of the membrane is very difficult to experimentally constrain due to its dependence on leak ion channels embedded in the membrane. Leak membrane ion channel composition can vary greatly even for different cells of the same cell type due to a large number of regulatory mechanisms that will be discussed in the next section. Therefore, membrane resistivity is a parameter that must generally be tuned by the modeler to match electrophysiologically recorded data, as I will do in aim 2.

1.4. Voltage - gated ion channels

Most modern biophysically realistic neuron models use HH's mathematical formalism to describe voltage-gated ion channels. This formalism has also heavily influenced the way that experimental ion channel data are collected through voltage-clamp analysis. Indeed, since the publication of their seminal 1952 paper, neuroscientists have been seeking to flesh out HH's limited initial framework which included only two invertebrate ion channels (sodium and potassium) and have discovered hundreds of ion

channels with unique properties. Despite this ever increasing variety of voltage-gated ion channels, the kinetics of most can be well approximated with HH's original mathematical gating model.

For the reader who may not be familiar with HH's formalism, ion channels are modeled with one or several voltage and time dependent 'gates' (Figure 1.1). The example HH channel shown is based on the properties of the fast sodium channel used in most of my models and has both activation (m) as well as inactivation (h) gates. There are actually three activation gates which must 'open' in order for current to flow through the channel, so the cube of the activation curve is also plotted (m^3). As the voltage increases, the activation gate opens at the same time that the inactivation gate closes. However, the time constant of the inactivation gate is slower than the activation gate, so the channel will open for a short time even at high voltages though it will quickly close due to the inactivation gate (in this case, after less than 1 ms).

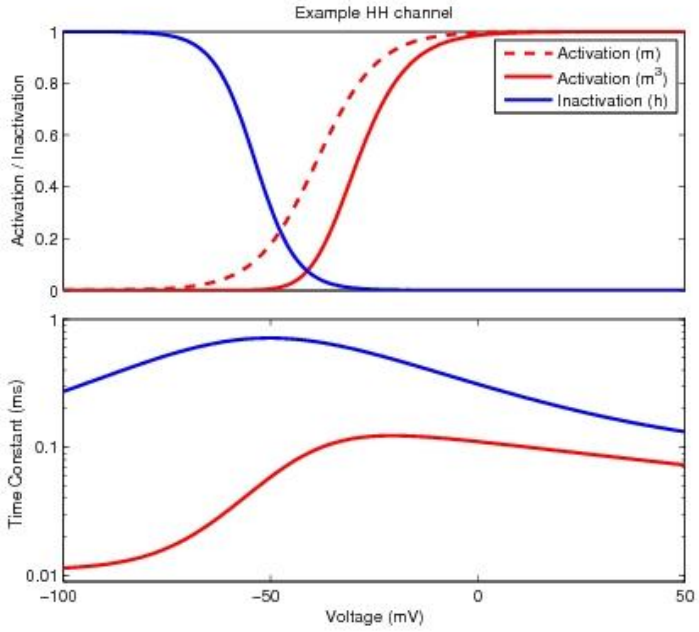

Figure 1.1: Properties of an example Hodgkin Huxley conductance.

1.4.1. Diversity of voltage-gated ion channels

Ion channels are a group of transmembrane proteins which are selectively porous for particular ions, possess an extraordinarily diverse set of functional behaviors, and often are voltage-gated or ligand gated (Hille, 2001). While ligand gated channels are extremely important due to their central role in synaptic transmission and other forms of intercellular signaling, voltage-gated channels play the largest part in defining the intrinsic electrical dynamics of neurons as well as their responses to external inputs (Llinas, 1988; Trimmer and Rhodes, 2004). Therefore, I almost always included a set of eleven voltage-gated ion channels in my computational neuron models which possessed dynamics representative of the full range of channels hypothesized to exist in GP neurons (Gunay et al., 2008) in order to maximize my ability to reproduce recorded biological activity. The set of ion channels that I used primarily included those selective for sodium, calcium or potassium ions.

Voltage-gated sodium channels rely on a transmembrane α subunit which forms a voltage-sensitive pore through which sodium ions can flow. In mammals, these α subunits are encoded by a diverse group of 10 genes (Nav1.1-1.9 and Nax) (Lai and Jan, 2006; Harmar et al., 2009). The gating properties of these different α subunits vary widely. For instance, the half-activation voltage for rat Nav1.1 expressed in Xenopus laevis oocyte was -18 mV while the half-activation voltage for Nav1.9 in rat dorsal root ganglion neurons was about -50 mV (Smith and Goldin, 1998; Cummins et al., 1999; Herzog et al., 2001). Of particular relevance to my work, voltage-gated sodium channels with Nav1.1, Nav1.2 and Nav1.6 alpha subunits are prominently featured in globus

pallidus neurons and underlie some of their most important capabilities including dendritic spike initiation and fast spiking (Hanson et al., 2004; Mercer et al., 2007). The voltage-sensing pore-forming α1 subunits of voltage-gated calcium channels exhibit a similar amount of genetic diversity to the voltage-gated sodium channels and are encoded by 10 known genes, while the α subunits of voltage-gated potassium channels are encoded by 40 known genes (Harmar et al., 2009). As for voltage-gated sodium channels, both voltage-gated calcium and potassium channels exhibit a wide range of functional gating behaviors. Unlike the selective cation ion channels just discussed, some channels are able to pass a mixture of multiple ions. For instance, the hyperpolarization-activated cyclic nucleotide-gated (HCN) channels are known to be permeable to sodium, calcium and potassium ions (Michels et al., 2008). In sum, neurons possess a very large selection of ion channels that can be placed in their membranes to generate a wide range of electrical activities. In addition to the choice of which ion channels to place in the membrane, neurons also have control over the gating properties of their ion channels through post-translational modulation and over the spatial distribution of ion channels throughout the axon and dendritic tree, which can have profound effects on the voltage environment that a channel experiences and therefore on its activity.

1.4.2. Modulation of ion channel properties

As just described, the gating properties of an ion channel encoded by a particular gene can vary by cell type. This variation is primarily due to modulation by various molecular factors, which can in principle also create variation in channel properties between cells of the same type. The molecular factors that modulate channel properties

range from kinases and phosphatases to signaling phospholipids (Suh and Hille, 2005) to additional subunits that can be added to channels. For instance, the Nav1.6 sodium channel prominent in GP neurons (Hanson et al., 2004; Mercer et al., 2007) has been shown to be modulated in at least 4 ways: 1) the binding of ankyrin-G to Nav1.6 channels modifies inactivation gating to greatly reduce persistent sodium current (Shirahata et al., 2006); 2) the binding of fibroblast growth factor homologous factor 2A to Nav1.6 channels slows the recovery from inactivation (Rush et al., 2006); 3) constitutive phosphorylation of Nav1.6 is necessary for fast deinactivation and resurgent current generation following spikes (Grieco et al., 2002); and, 4) interactions with Calmodulin decrease Nav1.6 inactivation time at depolarized potentials (Herzog et al., 2003). Therefore, a failure to perfectly match experimental electrophysiological recordings by tuning conductance densities could be due to incorrect channel kinetics, as I explore in aim 2.

Other important channels known to be present in GP are also modulated in a variety of ways in other cell types. For instance, the Kv4.2 A-type potassium channel known to be expressed by GP neurons (Tkatch et al., 2000) experienced a 15 mV depolarizing shift due to phosphorylation by either protein kinase A or protein kinase C in hippocampal CA1 pyramidal neurons (Hoffman and Johnston, 1998) and experienced greatly accelerated inactivation kinetics in Xenopus oocytes upon binding dipeptidyl peptidase 10, a putative accessory subunit of Kv4.2 (Jerng et al., 2004). While studies of channel modulation have not yet been done in GP, the evidence of a broad range of modulation mechanisms in many other cell types suggests that channels in GP neurons are likely to experience a diverse range of modulations which could vary from cell to cell

and which could prevent conductance density parameter tuning from achieving perfect matches to data.

1.4.3. Intracellular distribution

In addition to variability in gating properties, great variability exists between cell types in the intracellular distributions of ion channels (Migliore and Shepherd, 2002). The intracellular distribution of an ion channel depends on trafficking, retention and endocytosis pathways for that channel (Lai and Jan, 2006). Intracellular ion channel distributions are important to understand because they can functionally affect dendritic processing. For example, the distribution of dendritic HCN channels has been shown to allow distal and proximal synaptic events to produce somatic voltage responses with similar time courses (Williams and Stuart, 2000). In principle, all of these distribution mechanisms could vary from cell type to cell type in order to produce the variability in distributions which have been shown to exist. For instance, dendritic sodium conductance density is fairly uniform in mitral, CA1 pyramidal, and neocortical pyramidal neurons; in contrast, dendritic sodium conductance decreases rapidly with distance from the soma in thalamocortical and CA3 pyramidal neurons (Migliore and Shepherd, 2002). As another example, dendritic h-current conductance density is relatively constant for mitral and CA3 pyramidal neurons, but increases linearly with distance from the soma in neocortical and CA1 pyramidal neurons (Migliore and Shepherd, 2002). For GP neurons, most dendritic distributions of ion channels have not yet been determined; one exception is that high-voltage-activated calcium channels have been shown to be present in larger numbers in more distal dendrites (Hanson and Smith,

2002), although this study did not attempt to quantify dendritic conductance densities electrophysiologically. Therefore, when I automatically tune conductance density parameters in aim 2, I allow the densities to vary between the soma, axon and dendrites.

1.5. Active dendrites underlie functionally important neuronal behaviors in GP and other cell types

Their combination of complex morphologies and active conductances allows active dendrites to perform important computations (London and Hausser, 2005). For instance, in contrast to Cajal's long accepted law of dynamic polarization which posited a unidirectional flow of information from dendrites to soma to axon (Cajal, 1911), it has recently become clear that dendrites with sufficient densities of fast inward conductances can support back propagating action potentials which transmit information from the soma back to the dendrites (Stuart et al., 1997; Antic, 2003; Larkum et al., 2007). Furthermore, some active dendrites support the generation of dendritic action potentials which can propagate to the soma, including in GP, offering an alternative to the traditional integrate and fire concept of the neuron where the dendrites simply collect inputs to be summed at the soma (Andreasen and Lambert, 1998; Golding et al., 1999; Hanson et al., 2004). It is also known that dendritic conductances can shape the subthreshold voltage responses to synaptic inputs in a variety of ways. For instance, dendritic sodium conductance is known to amplify EPSPs (Lipowsky et al., 1996; Urban et al., 1998), while dendritic K+ conductance dampens them (Hoffman et al., 1997; Takigawa and Alzheimer, 2002). A more complex modification of EPSPs is seen with dendritic Ih conductance, which alters the size of each event to standardize the time course of the somatic voltage response

(Williams and Stuart, 2000). All of the aforementioned channels are known to exist in GP, although data on subcellular localization have only been published for sodium and calcium channels (Hanson and Smith, 2002; Hanson et al., 2004). Therefore, the capacity of the GP neuron models that I used for complex dendritic processing modes may be quite large; indeed, a significant portion of my first aim is devoted to understanding how the complex dendritic morphology of a GP neuron interacts with dendritic ion channels to influence back propagating action potentials, for instance, and whether these modes of processing can be preserved by neuron models with reduced dendritic morphologies.

1.6. Can reduced dendritic morphologies preserve realistic dendritic dynamics?

Reduced dendritic morphologies are attractive to modelers because they are computationally less expensive and more tractable to use than fully branched dendrites. However, it is not yet fully understood to what extent reduced branching structures are able to preserve the dendritic dynamics of a fully branched dendritic tree: I address this issue in my first aim. An excellent review of different types of neuron model was published recently (Herz et al., 2006) which separated neuron models into five classes: 1) detailed compartmental models with realistic morphologies and ion channels, 2) reduced compartmental models which possess simplified dendritic trees and realistic ion channels, 3) single compartment models, which possess no dendrites but generally still possess realistic ion channels, 4) Cascade models, which use nonlinear transformations and other mathematical primitives to reproduce neural dynamics, and 5) Black-box models, which can simply consist of experimentally derived probability distributions of inputs and

outputs. Here, I will consider the first 2 classes individually and lump the final three into one group. I lumped single compartment and simpler models, or 'simple models', into a third group because I will not consider their capabilities and limitations here. While simple models of various kinds have provided fundamental insights about neural dynamics, I'm choosing to ignore them here because they cannot be used to study dendritic dynamics.

Detailed compartmental models, or 'full models', are the most computationally intensive type of model, because they possess hundreds if not thousands of compartments which each contain on the order of 10 voltage gated conductance types; each of these requires multiple differential equations to be simulated at each time step. Indeed, full models are so computationally expensive that 1 second of full model simulation often takes more than 1 minute on a modern computer, which is prohibitive for studies requiring massive simulation runs such as parameter searches, databases, and large networks. Therefore, full models have been used most often when the hypothesis being tested requires a detailed morphological reconstruction. Such hypotheses tend to involve the precise interaction between dendritic events, like postsynaptic potential(s) or back propagating action potentials, and dendritic ion channels. For questions like these, full models have shown themselves to be particularly useful. For example, 27 full morphologically reconstructed CA1 pyramidal neuron models were used to show that the dendritic distribution of A-type K+ conductance had a large effect on back propagation of action potentials but did not greatly affect forward propagation of dendritic spikes (Migliore et al., 2005). However, full models are sometimes used in studies that involve little or no complex dendritic computations, in which case a reduced compartmental

model, or ‘reduced model’ would have given more clearly interpretable results with smaller computational requirements. For instance, full morphologically reconstructed models were recently used to test the abilities of different automated parameter tuning methods to match somatic current injection data; however the dendrites were left passive (Druckmann et al., 2008). With passive dendrites and without synaptic input, there is little reason to use a full morphological reconstruction of the dendritic tree rather than a simplified version. Fortunately, while studies like this may have wasted some CPU time and added some needless complexity, the results are likely to be reliable. This may not be the case if too little detail was used, as will be considered next.

Reduced models are the next most computationally expensive type of model after full models. Reduced models are frequently used in computational neuroscience to understand phenomena involving dendrites which are not believed to require the simulation of a full model. Studies using reduced models have taught us a lot about neural dynamics. For example, a network of reduced cerebellar neuron models was used to highlight the axonal delay of axo-dendritic inhibitory connections as the key determinant of resonant synchronization at frequencies from 40 to > 200 Hz (Maex and De Schutter, 2003). Another elegant study used a reduced CA1 pyramidal neuron model to show that persistent sodium conductance increased the relative refractory period following spikes while decreasing interspike interval variability in the presence of in vivo-like dendritic synaptic input (Vervaeke et al., 2006). Unfortunately, modelers rarely justify their use of reduced models versus full models. This is most likely due to the lack of a clear mechanistic understanding in the literature of when it is or is not appropriate to use reduced morphologies. This missing link leads most modelers to make a rather

arbitrary choice over a fundamental issue which, if chosen incorrectly, could undermine their best modeling efforts. Indeed, some studies using reduced models to understand dendritic phenomena may have reached very different conclusions if they had used full models. For instance, a recent study matched action potential amplitudes in the soma and dendrite of a reduced L5 pyramidal neuron model to dual recordings in slice L5 pyramidal neurons by automated parameter tuning to constrain the dendritic density gradients of voltage-gated Na+ and K+ conductances (Keren et al., 2009). Unfortunately, while real L5 pyramidal neurons possess quite thin apical dendrites whose diameters quickly taper to less than 1 μm with distance from the soma (Mainen and Sejnowski, 1996), their reduced model's single apical dendritic cylinder possessed a diameter of 5 μm. The extremely large dendritic diameter of their reduced model most likely made it very difficult for action potentials to successfully backpropagate, as I will show in aim 1; indeed, this is probably why they found that the dendritic density of voltage-gated Na+ conductance had to be almost as high as in the soma (Keren et al., 2009).

1.7. Many model parameters are not constrained by experiments and must be tuned

Tuning neuron model parameters is a prominent feature of my second aim and is a complicated task. This task is particularly daunting for multicompartmental biophysically realistic neuron models due to the possibility for variations in channel kinetics and regional variability in conductance density parameters. The number of parameters can easily exceed 20, which makes hand tuning the model an extremely tedious and time consuming task. To avoid hand tuning, modelers frequently adopt

automated or semi-automated methods of parameter tuning. One semi-automated method that has gathered much attention recently is known as a 'brute-force' database search. This type of search starts by building a parameter set database, where the neuron model has been simulated and its output characterized for all parameters sets. The database can then be searched for desired model output characteristics. For instance, a database was developed for a 1 compartment model of a lobster stomatogastric ganglion neuron with 8 parameters that provided insights about how its membrane conductances determined its response properties (Prinz et al., 2003). Unfortunately, while 1.7 million simulations were sufficient to develop this database (6 values for each of the 8 parameters: 6^8), $1.7 * 10^{20}$ simulations would be required to build a similar database with my 26 free conductance density parameter reduced compartmental models (6^{26}), which would take about 50 trillion CPU years on our machines. Therefore, when the number of parameters is large (> 10), automated parameter searches are used because, in contrast to brute force databases, they do not need to exhaustively sample parameter space in order to tune neuron models (Vanier and Bower, 1999; Van Geit et al., 2008). For instance, 11 parameters of a single compartment medial vestibular nucleus neuron were successfully optimized using the automated search known as 'simplex simulated annealing' (Weaver and Wearne, 2006), which mimics the natural process by which liquids find a low energy solid state when frozen very slowly (Cardoso et al., 1996). In another study, the output of a 10 parameter Morris-Lecar model was optimized using a genetic algorithm (Gerken et al., 2006), which mimics the natural process of genetic recombination to 'evolve' better parameter sets (Srinivas and Patnaik, 1994). Other 'evolutionary' algorithms include differential evolution (Price et al., 2005) and the particle swarm optimization algorithm

(Clerc and Kennedy, 2002). Overall, while evolutionary algorithms (including simulated annealing) have been shown to be superior to gradient descent or random searches for optimizing complex neuron model parameter spaces, there is no clear evidence that one evolutionary algorithm is better than another (Vanier and Bower, 1999; Van Geit et al., 2008). I chose to use a modified version of the particle swarm optimization algorithm for my automated searches in aim 2 because I consider it to be the most intuitive of the available evolutionary algorithms.

1.8.Experimental design

1.8.1. Aim 1:

I reduced the morphological complexity of a previously characterized full GP neuron model (Gunay et al., 2008) to conduct a detailed analysis of the limitations of two types of model reduction strategies. The first strategy preserved the detailed branching structure of the full model ('branched' models), while the second strategy only preserved the surface area and electronic length of each major dendritic branch by collapsing sub-branches ('unbranched' models). I compared many properties such as spike waveforms, spike rate versus current injection curves, spike rate responses to synaptic inputs, and precise spike times between the full, branched and unbranched models to determine which properties could be retained without adjusting channel densities. I also tested the hypothesis that the detailed dendritic branching structure was important during large dendritic events like excitatory post synaptic potentials and back propagating action potentials, particularly in the presence of fast dendritic voltage-gated conductances.

When response properties were not maintained, I conducted detailed mechanistic analyses of the models to understand why not. I performed these analyses in order to be able to offer clear guidelines about the capabilities and limitations of reduced models.

1.8.2. Aim 2:

Because the intrinsic electrical properties of neurons depend sensitively on the modifiable behavior of their ion channels, I analyzed the added benefits of optimizing kinetic parameters over the optimization of density parameters by performing automated optimization of three GP neuron models. I built and reduced these models based on three electrophysiologically characterized and morphologically reconstructed GP neurons. In order to match model output to the recorded traces, I performed two stages of automated parameter searches. For the first stage, conductance densities were set free; the best matches of this stage exhibited mismatches to the data due to limitations in our channel models. I hypothesized that kinetic searches would improve channel kinetics and allow better matches to the recorded data than were possible just by optimizing conductance densities. To test this hypothesis, I ran second stage searches which set either all kinetics free or a small group selected based on an 'error sensitivity analysis'. The error sensitivity analysis identified parameters likely to improve the match found with free densities. I found that my second stage kinetic searches consistently improved matches to data. I further hypothesized that some kinetic improvements would be consistent between cells and shed light on potential problems with our channel kinetics, which are based on data recorded in other species, cell types, or preparations (e.g. slice vs dissociated cells). Upon analysis of the data, I found that my searches sometimes did

find new values of channel kinetics which were consistent across random starting points. Overall, I analyzed my searches in order to offer modelers a clear understanding of the role that automated searches can play in optimizing model channel kinetics.

CHAPTER 2: AIM 1 – THE CAPABILITIES AND LIMITATIONS OF CONDUCTANCE-BASED COMPARTMENTAL NEURON MODELS WITH REDUCED BRANCHED OR UNBRANCHED MORPHOLOGIES AND ACTIVE DENDRITES

2.1. Abstract

Conductance-based neuron models are frequently employed to study the dynamics of biological neural networks. For speed and ease of use, these models are often reduced in morphological complexity. Simplified dendritic branching structures may process inputs differently than full branching structures, however, and could thereby fail to reproduce important aspects of biological neural processing. It is not yet well understood which processing capabilities require detailed branching structures. Therefore, we analyzed the processing capabilities of full or partially branched reduced models. These models were created by collapsing the dendritic tree of a full morphological model of a globus pallidus neuron while preserving its total surface area and electrotonic length, as well as its passive and active parameters. Dendritic trees were either collapsed into single cables (unbranched models) or the full complement of branch points was preserved (branched models). Using this reduction strategy, we were able to use the same channel density settings in the full and all reduced models to compare their dynamics. Full model responses to somatic inputs were generally preserved by both types of reduced model. The responses of the full model to dendritic inputs could be better preserved by branched than unbranched reduced models. However, features strongly influenced by local dendritic input resistance, such as active dendritic sodium

spike generation and propagation, could not be accurately reproduced by any reduced model. Based on our analyses, we suggest that there are intrinsic differences in processing capabilities between unbranched and branched models. Due to the ability of our unbranched reduced models to map full model somatic input output dynamics with identical conductance densities, one application for unbranched reduced models is to perform fast searches of full model parameter space.

2.2. Introduction

Single cell computer models can provide important insights into the mechanisms of neuronal processing. 'Full models' possessing morphologically complete dendritic trees have helped to elucidate many key functions of dendritic computation, for example by showing that the extent of action potential back propagation depends on the degree of dendritic branching (Schaefer et al., 2003). Furthermore, dendritic sub-branches have been shown to independently regulate channel densities (Losonczy et al., 2008). Due to high computational requirements, full models are frequently replaced in network simulations and even in the exploration of single neuron properties by 'reduced' models possessing fewer compartments and simplified dendritic branching structures (Herz et al., 2006). For example, reduced models were used to study the control of burst firing by dendritic NMDA receptor activation (Kuznetsov et al., 2006) and the reliance on dendritic T-currents for low-threshold Ca^{2+} spiking (Destexhe et al., 1998). Computationally efficient reduced models are also particularly useful for the simulation of large networks of neurons and have been used, for example, to study gamma-frequency synchronization through dendro-dendritic gap junctions (Traub et al., 2001).

While passive models with certain constraints can be analytically collapsed using cable theory (Rall et al., 1992; Burke, 2000), a lossless reduction of models with active dendritic properties is not possible. A clear understanding of the limitations of reduced active models with and without the preservation of the detailed branching structure is highly desirable in order to reach biologically valid conclusions regarding network computation.

In the present study, we used a previously characterized full GP neuron model (Gunay et al., 2008) to conduct a detailed analysis of the limitations of two types of model reduction strategies. The full GP model has extended thin dendrites with multiple active conductances, which makes it a good test case for possible limitations resulting from model reduction. We compared two principled strategies of model reduction that can be applied to full morphologies of all cell types. The first strategy preserved the detailed branching structure of the full model, while the second strategy only preserved the surface area and electronic length of each major dendritic branch by collapsing sub-branches. We found that both branched and unbranched model morphologies could retain many properties such as spike waveforms and fI curves of the full model without adjusting channel densities. However, when the morphology was reduced to a small number of compartments, detailed spike waveforms showed pronounced mismatches due to differences in axial current flow. Model properties dependent on local dendritic interactions between inputs and active conductances could not be fully maintained even in models with branched dendrites due to unavoidable local input impedance mismatches between full and reduced models. Overall our analysis provides clear guidelines to the limitations of reduced models and highlights specific aspects of synaptic processing

requiring full branching structures. Furthermore, we show that our reduced models can successfully reproduce many integrative properties of full models. Indeed, given the reduction strategies that we used, identical channel density settings can be mapped between full and reduced morphologies to produce the same dynamics. In particular, we show that our unbranched reduced models can map full model somatic input output dynamics, which allows them to be used as fast search engines of the full model parameter space.

2.3.Methods

2.3.1. Full Morphological GP Neuron Model:

Previously, we have described the construction and validation of a database of full GP models (Gunay et al., 2008). Models were constructed with 3 dendritic morphologies, which were obtained using Neurolucida (MicroBrightField, Inc., Williston, VT) from biocytin filled rat GP neurons in slice. One of these morphologies (s34 in Gunay et al, 2008) was selected for the full GP model used in this study: this morphology contained a soma and 511 dendritic compartments. As in Gunay et al 2008, the passive properties were set to Rm (specific membrane resistance) = 1.47 ohm-m^2, Cm (specific membrane capacitance) = 0.024 F/m^2, and Ra (specific axial resistance) = 1.74 ohm-m all compartments. Each somatic and dendritic compartment of the full model also contained 11 different voltage and calcium gated ion channels: these were fast sodium (NaF), persistent sodium (NaP), slow activating delayed rectifier (Kv2), fast activating incompletely inactivating potassium (Kv3), low voltage activated potassium ($Kv4_{fast}$ and $Kv4_{slow}$), KCNQ family potassium (KCNQ), calcium activated potassium (SK), high

voltage activated calcium (CaHVA), and H-current (HCN_{fast} and HCN_{slow}). All dendritic compartments were given the same conductance density for each channel (i.e. no gradients). A full description of channel kinetics is given in Supplemental Tables 2-1 and 2-2. See Gunay et al. 2008 for the process of parameter tuning.

Axons are generally not reconstructed from neurons recorded in brain slices, because the slicing procedure often severs the axon close to the soma. This was the case in our GP reconstructions as well, and therefore our study of full GP model properties employed a default axon comprised of multiple nodal and internodal segments (Gunay et al., 2008). Here, we replaced this artificial axon with a single axonal compartment so that it could be directly transferred to the reduced models without greatly increasing morphological complexity. This replacement required a recalibration of axonal and somatic channel densities (Supplemental Table 2-3) in order to preserve the original model activity that was tuned to match slice recordings.

The tuned parameter set used for most of this study contained a medium level of dendritic sodium conductance (gNa consisting of 40 S/m^2 NaF and 1 S/m^2 NaP) which was not sufficient to support dendritic spike initiation. However, dendritic spike initiation has been recorded in GP (Hanson et al., 2004) and other neuron types, and represents an important possible mode of synaptic integration in vivo. Therefore, dendritic spike initiation and other responses were compared between the full and reduced models using an alternative to the tuned parameter set which contained a high level of dendritic gNa (800 S/m^2 of dendritic NaF and 1 S/m^2 of dendritic NaP). This dendritic gNa density allowed frequent spike initiation with appropriate dendritic stimulation (Supplemental Fig 2-3). To assess the contribution of both levels of dendritic

gNa to mismatches between the full and reduced models, a third alternative parameter set was used which contained no dendritic gNa. Model responses with these alternative parameter sets were described in the text or shown in supplemental figures when there were important differences with the results using the tuned parameter set.

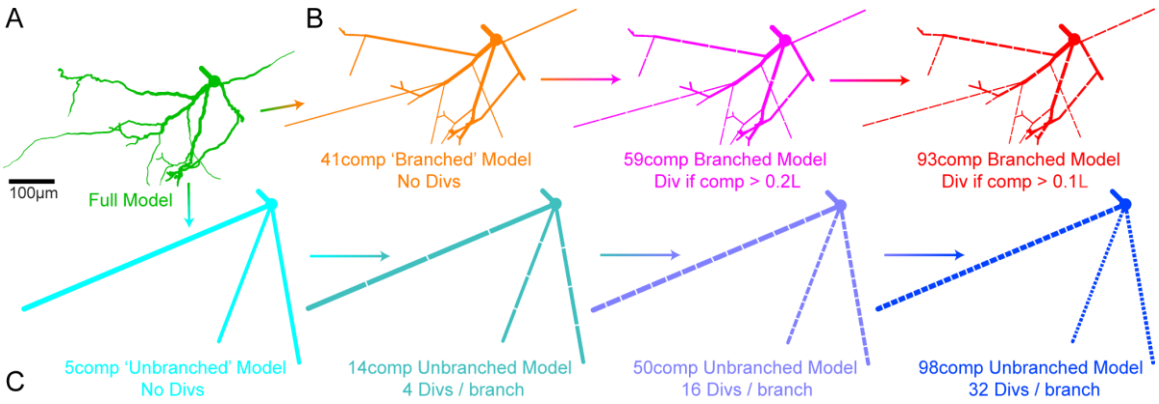

Figure 2.1: Morphological reduction.

To aid visualization, dendritic diameters are multiplied by 5 while soma diameters are multiplied by 2. A, The full GP model (green) has 513 compartments: these include 511 dendritic compartments, an axon compartment, and a soma. B, To create the simplest 'branched' reduced model (41comp, orange), the soma and axon compartment were unaltered while each group of compartments in the full model's dendritic tree not containing any branch points was collapsed into one dendritic compartment with the same total surface area and total electrotonic length (see Methods). The dendrites of the 41comp model were then divided lengthwise into equal parts until no dendritic compartment in the model was longer than 0.2L (59comp, magenta) or 0.1L (93comp, red). C, To create the first 'unbranched' reduced model (5comp, cyan), each major branch of the full model's dendritic tree was collapsed into a single dendritic compartment which preserved the total surface area and average soma-to-tip electrotonic distance for that major branch (see Methods). To create the 14comp (turquoise), 50comp (purple), and 98comp (blue) models, each dendritic compartment of the 5comp model was divided lengthwise into 4, 16, and 32 pieces, respectively. All conductance densities and passive parameters were preserved in each reduced model. The color scheme used in this figure was consistently applied to all remaining figures in Chapter 2.

2.3.2. Morphological Reductions:

We collapsed the dendritic tree of the full GP model in order to study which full model activities could be matched by morphologically reduced models. Morphological reduction could cause functional mismatches between the full and reduced model for two main reasons: first, by definition, morphological reduction must cause a decrease in the

number of compartments and an increase in average compartment size; second, morphological reduction could cause a loss of the detailed branching structure of the full model. To distinguish between these two possible causes of activity changes, two types of reduced models were created. The first type required dozens of compartments in order to preserve the detailed branching structure of the full model (Fig. 2.1*B*, 'branched' reduced models), while the second type required only a few compartments because it did not preserve the detailed branching structure (Fig. 2.1*C*, 'unbranched' reduced models).

To create the branched reduced models, all groups of dendritic compartments in the full model were found which did not span branch points: there were 39 such groups. Each group of compartments was converted into a single branched reduced model compartment such that the total surface area (TSA) and end to end electrotonic length (L) were preserved. TSA was preserved in order to maintain active current densities and cell input resistance (Destexhe, 2001; Tobin et al., 2006), while L was preserved because the electrotonic structure of a neuron strongly affects the integration of synaptic input and dendritic attenuation of somatic voltage signals (Burke, 2000; Destexhe, 2001). Holding all passive parameters including Rm and Ra fixed, the TSA and L for a given group were used to calculate the length (l) and radius (r) of the corresponding reduced model compartment using the following two equations:

$$L = l\sqrt{\frac{2 * Ra}{Rm * r}} \tag{1}$$

$$TSA = 2 * \pi * r * l \tag{2}$$

Including the soma, the axon compartment, and the 39 dendritic compartments generated this way, the simplest branched reduced model had 41 compartments (Fig. 2.1*B*, '41comp' orange model). The 41comp model possessed some compartments that were

quite electrotonically extended and could prevent the 41comp model from matching certain full model responses. Therefore, the 41comp model's extended dendritic compartments were divided such that none was longer than 0.2 L (Fig. 2.1*B*, '59comp' model) or 0.1 L (Fig. 2.1*B*, '93comp' model).

While the branched reduced models maintained the TSA and L of all detailed branches of the full model, the unbranched reduced models only maintained the TSA and L of each of the three major branches. Indeed, it is only possible to maintain all the passive electrical characteristics of a full model when reducing its branching structure if the dendritic tree meets two criteria: 1) dendrites must follow the 3/2 power branching rule and 2) all paths from the soma to dendritic tips must have equal electrotonic lengths (Rall, 1959, 1964). As for most real dendritic trees, these strict criteria were not satisfied by the GP full model. Therefore, we were forced to choose which aspects of the full model's morphology to preserve when reducing the morphology to produce the unbranched reduced models. We chose to preserve the TSA and average tip to tip L of each major branch for the same reasons that we preserved TSA and L for each branch in the branched reduced models.

For the unbranched reduced models, the TSA of each major branch was calculated by summing its compartment surface areas; the L of each major branch was estimated as the mean soma-to-tip L for all the tips in that major branch. Using equations 1 and 2 and these values for TSA and L, we reduced each major branch of the full GP model into a single compartment to create a 5-compartment unbranched reduced model (Fig. 2.1*C*, '5comp' model). Because each dendritic compartment of the 5comp model was greater than 0.5 L, we progressively divided each dendritic compartment lengthwise

to be able to analyze which features of the full model were lost due to altered branching structure and which were due to increased compartment size: each compartment of the 5comp model was divided lengthwise into 4, 16 and 32 equal pieces to form the '14comp', '50comp' and '98comp' models, respectively (Fig. 2.1*C*).

2.3.3. Synaptic Inputs:

General features: In several simulations, randomly timed synaptic events were applied to dendritic compartments. Synaptic inputs consisted of AMPA (τ_{rise} = 1 ms, τ_{fall} = 3 ms, E_{syn} = 0 mV), NMDA (τ_{rise} = 10ms, τ_{fall} = 30 ms, E_{syn} = 0mV) and GABA (τ_{rise} = 1 ms, τ_{fall} = 12 ms, E_{syn} = -80 mV) conductances. All synapses had a maximal conductance of 0.25 nS and were distributed in the full model such that each dendritic compartment received one AMPA/NMDA and one GABA synapse. In the branched reduced models, synapses were directly mapped from the full model and preserved both their locations in the detailed branching structure and their exact activation times. In the unbranched reduced models, synapses could only be approximately mapped: synapses were placed in compartments such that the electrotonic span and major branch location of each compartment determined how many synaptic inputs it received. For example, the most proximal dendritic compartment in the 14comp model's (Fig. 2.1*C*) first branch spanned from 0 to 0.14 L. In the full model's first major branch, this electrotonic span contained 20 compartments; therefore, the most proximal dendritic compartment in the 14comp model's first branch received the synapses contained in those 20 compartments. Some full model dendritic compartments were more electrotonically distal than any compartment in the unbranched reduced models. These synapses were shifted to the

most distal compartment in the unbranched reduced model; shifting synapses in this way did not cause a large shift in the average synapse position for the unbranched reduced models (Table 2-1).

Table 2-1: Comparison of basic morphological properties between the full and reduced models.
All models contained 3 major branches and possessed the same total surface area. Furthermore, the full and branched reduced models had identical soma to tip L for all branches. The unbranched reduced models were identical to each other except for the lengthwise divisions of their dendritic compartments. Note that mean compartment length (L) and mean compartment surface area (SA) decreased as model compartments were divided. Similarly, divided compartments allowed the mean synaptic position (L) to approximate the full model value in both types of reduced model. Regardless of compartment division, the unbranched reduced models possessed much smaller median ratios of compartment Ra to SA (median Ra/SA) than either the full or branched reduced models.

Property	Full	41comp	59comp	93comp	5comp	14comp	50comp	98comp
# dend comps	511	39	57	91	3	12	48	96
Mean comp length (L)	0.013	0.175	0.12	0.075	0.66	0.165	0.041	0.021
Mean comp SA (μm^2)	14.5	190	130	81.4	2468	617	154	38.6
Mean synaptic position (L)	0.512	0.734	0.577	0.537	0.733	0.548	0.497	0.488
Median Ra/SA ($M\Omega$ / μm^2)	1.752	1.402	1.652	2.055	0.143	0.143	0.143	0.143

Cluster distributions for synchronous excitation: In some experiments, excitatory inputs that were already present in each model were activated as synchronous clusters. Eight clusters, each containing thirteen compartments, were defined on different branches of the full model's dendritic tree at about 0.175L (2), 0.35L (2), 0.525L (2) and 0.7L (2).

In order to be able to directly compare synchronous and asynchronous activation, clusters were activated using common event timetables which maintained the average asynchronous activation rates of their synapses. To allow for direct comparisons with full model responses, cluster positions were directly mapped to their corresponding locations in the branched reduced models. In contrast, cluster positions could not be directly mapped into the unbranched reduced models due to the loss of the detailed branching structure. However, clusters in the unbranched reduced models did maintain major branch locations and approximate electrotonic positions. Furthermore, clusters in the unbranched reduced models included the number of compartments that best approximated the TSA of that cluster's compartments in the full model.

2.3.4. Simulations:

Simulations were performed using GENESIS 2.3 (http://www.genesis-sim.org/GENESIS/) on Linux workstations. Simulation data were analyzed in Matlab (The Mathworks, Inc, Natick, MA).

2.3.5. Statistics:

For statistical analyses, data set normality was assessed with the Lilliefors test, which showed that all of our sampled data sets were not normally distributed. The non-parametric Mann-Whitney U test was therefore used for statistical comparisons. To correct for multiple simultaneous comparisons, the Mann-Whitney U test significance

level was decreased from $\alpha = 0.05$ using the Bonferroni correction. All statistical tests were performed in Matlab.

2.3.6. Data Sharing:

Upon publication, all models along with all current injection and synaptic input patterns used in this study will be made available on the ModelDB public database (http://senselab.med.yale.edu/ModelDB/default.asp).

2.4. Results

2.4.1. Matching passive somatic and dendritic responses

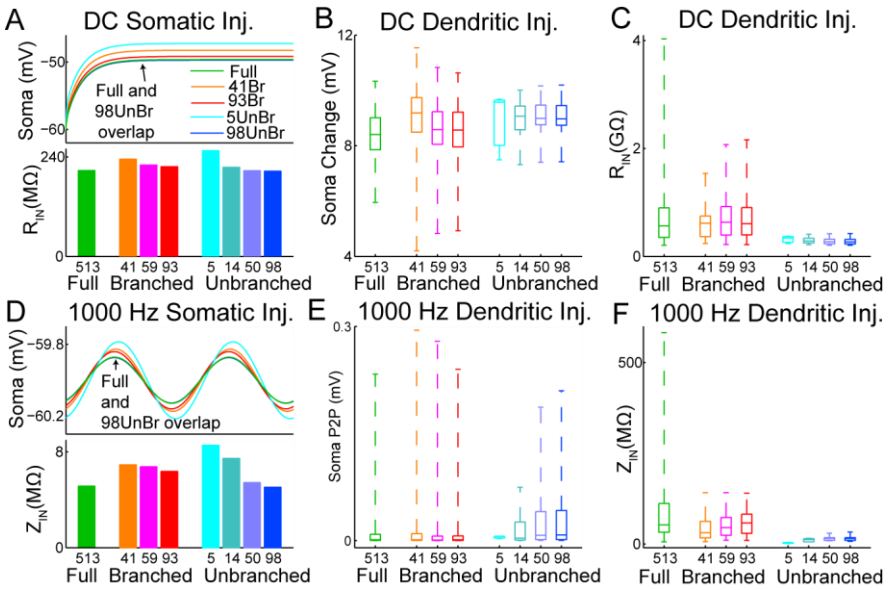

Figure 2.2: Passive somatic responses to DC or 1000 Hz current injection into the soma or individual dendritic compartments.

A, Voltage deflections (top, selected models) and R_{IN} (bottom, all models) are plotted for 50 pA current injections into the soma. R_{IN} was calculated by dividing the steady state voltage change by the DC amplitude. Note the slight increase in R_{IN} for the most reduced branched or unbranched models. B, Each dendritic compartment was separately injected with 50 pA of DC. The box and whisker plots show the amplitudes of the resulting somatic voltage deflections: the middle horizontal

bar represents the median while the upper and lower horizontal bars represent the 75th and 25th percentiles, respectively; the whiskers identify the most extreme values found. Box and whisker plots, bar graphs, and raster plots present the models in the same order consistently throughout the paper. Note that the median somatic voltage change for injection into different dendritic compartments was comparable for all models, but that branched reduced models showed slightly larger variability in somatic responses than the full model, whereas unbranched reduced models showed slightly lower variability. C, Distributions of local dendritic R_{IN} values for each model. The median and quartile values but not whisker extents were similar between the branched reduced models and the full model, whereas the unbranched reduced models had lower median dendritic R_{IN} and showed much less variability between compartments. D-F, Same plots as A-C, except the injected current was a 1000 Hz sinusoidal input with an amplitude of 50 pA. Input impedance (Z_{IN}) was calculated as the peak-to-peak (P2P) voltage deflection divided by 50 pA.

The passive properties of a neuron model strongly influence its responses in the presence of active conductances (Rall et al., 1992). Therefore, we compared the passive responses between the full model and our branched or unbranched reduced models with different numbers of compartments (Fig. 2.1). Despite the use of the same soma and axon compartments for all models as well as the preservation of certain dendritic morphological properties (see Methods), passive responses to somatic current injection were affected by dendritic properties due to axial current flow and varied by model. Both 0 Hz (DC) and 1000 Hz current injections were applied because the passive response properties of a neuron model depend on the frequency of inputs (Johnston and Wu, 1995). Mismatches between the somatic input resistance (R_{IN}) of the reduced and full models ranged from 1% for the 98comp unbranched model to 23% for the 5comp unbranched model (Fig. 2.2*C*). In contrast, the 1000 Hz input impedance (Z_{IN}) was a more challenging measure for reduced models with few compartments: the mismatches between reduced and full model somatic Z_{IN} ranged from only 2% for the 98comp unbranched model to 67% for the 5comp unbranched model (Fig. 2.2*F*). The quality of the match was greater for reduced models with mean compartment lengths which were

more similar to that of the full model, whether or not the branching structure was preserved (Table 2-1, Fig. 2.2*A*). The increased R_{IN} and Z_{IN} of the models with the largest trunk compartments near the soma (5comp unbranched and 41comp branched models) is explained by the decreased axial current that can exit the soma because of the high axial resistance (R_A) of the first dendritic compartment, which lumps together the R_A of several compartments in the full model. Therefore the dendritic trunk is charged less and the soma more by somatic current injection. This effect is larger for 1000 Hz input to the soma (Fig. 2.2*D*), and thus fast somatic currents such as those during an action potential (AP) can be expected to create larger somatic voltage deflections with a different time course in models with high R_A values in the initial trunk compartments. This dependence of fast transients on all axial currents in a neuron should be kept in mind, for example when examining the interaction between ion channel kinetics and morphology to produce smooth or kinky action potential onsets, an issue that has recently gathered much interest (Naundorf et al., 2006; McCormick et al., 2007).

Next we examined the reproduction of somatic responses to dendritic input in our reduced models. We found that the median passive somatic response amplitudes to dendritic current injections in all compartments (one by one) of branched and unbranched reduced models were respectively within 11% and 14% of the median full model response amplitude for DC injection (Fig. 2.2*B*). In contrast, with 1000 Hz injection, we found that median response amplitudes of the branched reduced models were only within 42% of the full model median response amplitude while the best matching unbranched reduced model's median response amplitude was 174% larger than that of the full model. (Fig. 2.2*E*). However, the absolute magnitudes of the differences between reduced and

full model median response amplitudes were only about 2 μV with 1000 Hz injection because the somatic response amplitudes for 1000 Hz dendritic injections were generally very small.

In contrast to the small (absolute) differences between the somatic passive responses of the full, branched and unbranched reduced models to dendritic input, the local dendritic responses diverged between branched and unbranched model reductions. Indeed, mismatches between the median local dendritic DC R_{IN} of the branched reduced and full models ranged from only 7% to 12% while mismatches for the unbranched reduced models ranged from 40% to 52% (Fig. 2.2*C*). For the more challenging measure of median local dendritic Z_{IN} with 1000 Hz input, the mismatches between the branched reduced and full models ranged from only 10% to 41% while unbranched reduced model mismatches ranged from 71% to 93% (Fig. 2.2*F*). The unbranched reduced models possessed lumped branches which were thicker than those of the full or branched reduced models and therefore exhibited smaller local R_{IN}s and Z_{IN}s because their dendritic compartments possessed much smaller median R_A relative to surface area (Table 2-1). Due to this unavoidable characteristic of unbranched models, current flowed away from the injection site more easily and did not charge the membrane locally as much as in the full or branched reduced models. This difference between branched and unbranched models could be quite important for modeling studies of excitatory postsynaptic potential (EPSP) amplification, for instance, because the amount of amplification depends non-linearly on the dendritic voltage reached (Golding and Spruston, 1998).

Despite matching the median dendritic R_{IN} and Z_{IN} of the full model, the branched reduced models lacked dendritic R_{IN}s or Z_{IN}s as large as some present in the full model.

Indeed, the full model possessed maximum dendritic DC R_{IN}s and 1000 Hz Z_{IN}s which were respectively about twice and four times as large as any possessed by a branched reduced model (box plot whiskers in Fig. 2.2*C,F*). Furthermore, the full model possessed 105 compartments which had larger 1000 Hz Z_{IN}s than any exhibited by a branched reduced model compartment. The unbranched reduced models showed even less variability in local dendritic R_{IN}s and Z_{IN}s, due to their lack of small side branches.

In conclusion, the unbranched reduced models matched the full model's passive somatic responses but failed to match its dendritic R_{IN}s and Z_{IN}s. In contrast, the branched reduced models matched both the somatic and median dendritic passive responses of the full model to current injection. However, the branched reduced models lacked a population of dendritic R_{IN}s or Z_{IN}s as large as many present in the full model. These similarities and differences in passive properties between the reduced and full models provide much of the basis for emerging similarities and differences in the active models.

2.4.2. Using 'mock' action current injection to predict differences in AP size

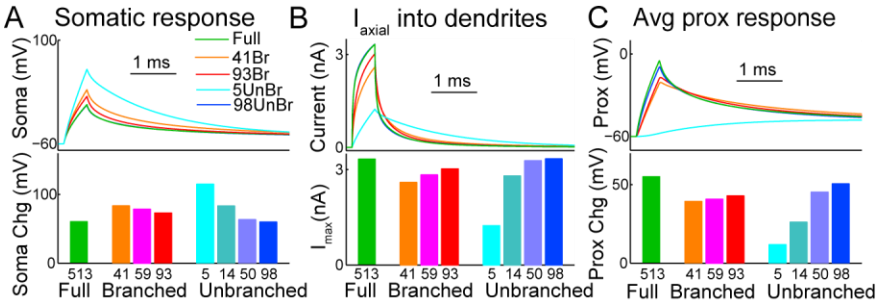

Figure 2.3: The passive somatic response amplitude to a mock action current depended on dendritic axial resistance.

The stimulus was a brief (0.5 ms) large (5 nA) somatic current pulse which caused a voltage response in the passive soma that mimicked the amplitude and rise-time of an AP in the absence of voltage gated conductances (mock AP). A, The mock AP was smallest in the full model and the most subdivided (50comp and 98comp) unbranched reduced models. The ability of the reduced models to match the full model mock AP response improved as compartments were divided. B, Models with

more finely-divided compartments allowed larger axial currents to exit the soma into the dendrites during the mock AP. C, Models with larger axial currents exiting the soma exhibited larger average voltage deflections in their most proximal dendritic compartments (those directly connected to the soma).

The detailed spike shape is a frequently studied electrophysiological feature (Bean, 2007) which can depend on a neuron's morphology (McCormick et al., 2007). It is therefore an interesting question whether reduced computer models should be expected to faithfully reproduce this feature of the experimental data. The results shown above suggest that purely passive differences in axial current flow between full and reduced models could confound studies of how active conductances determine the detailed spike shape. Unfortunately, isolating differences in spike shape due to axial current flow in the presence of voltage-gated conductances is complicated due to the non-linear interactions between the membrane voltage trajectory and conductance activation. The injection of a fixed 'mock AP current' into the passive models allowed us to determine which differences in the active AP should be expected based on passive properties alone. For a mock AP, we used a square current pulse injection with 5 nA amplitude and 0.5 ms duration, which produced a voltage spike with an amplitude and rise time similar to a Na^+ action potential. We found that the mock AP voltage deflection was within 1% of the full model's value for the 98 comp unbranched model; however, as the average electrotonic size of compartments increased, the closeness of reduced model voltage deflections to that of the full model decreased (Table 2-1, Fig. 2.3*A*). Indeed, the mock AP voltage deflection showed a steeper onset and was 55% larger in the 5comp unbranched model than in the full model due to the reduced axial currents flowing into the high Ra dendritic trunk of the 5comp model (Fig. 2.3*B*). For the same reason, the mock action current led to a much decreased voltage deflection in the dendrites of this model (Fig. 2.3*C*). Note

that the same factors contributed to considerable dendritic mock AP size differences between the 14comp unbranched model and full model, and that even the branched reduced models showed smaller dendritic mock AP sizes due to larger Ra values of the trunk dendritic compartments. Overall, our results with mock AP current injection show that large dendritic trunk compartments can lead to differences in AP size. Additionally, decreased passive back propagation of the AP could influence the activation of dendritic voltage gated currents and therefore could further exacerbate differences in integrative properties for the most reduced models. Nevertheless, both branched reduced models and unbranched models with > 10 compartments generally exhibited close matches to full model somatic mock AP size.

2.4.3. Analysis of detailed somatic shape of sodium APs for different levels of model reduction

After isolating the influence of reduced model architectures on voltage transients for fixed current injection pulses, we added the full complement of ion channels back in to compare Na^+ AP shapes between the full and reduced models. This set of simulations allowed us to determine the influence of the described passive mismatches on voltage-gated channel activation, which could further exacerbate spike shape mismatches.

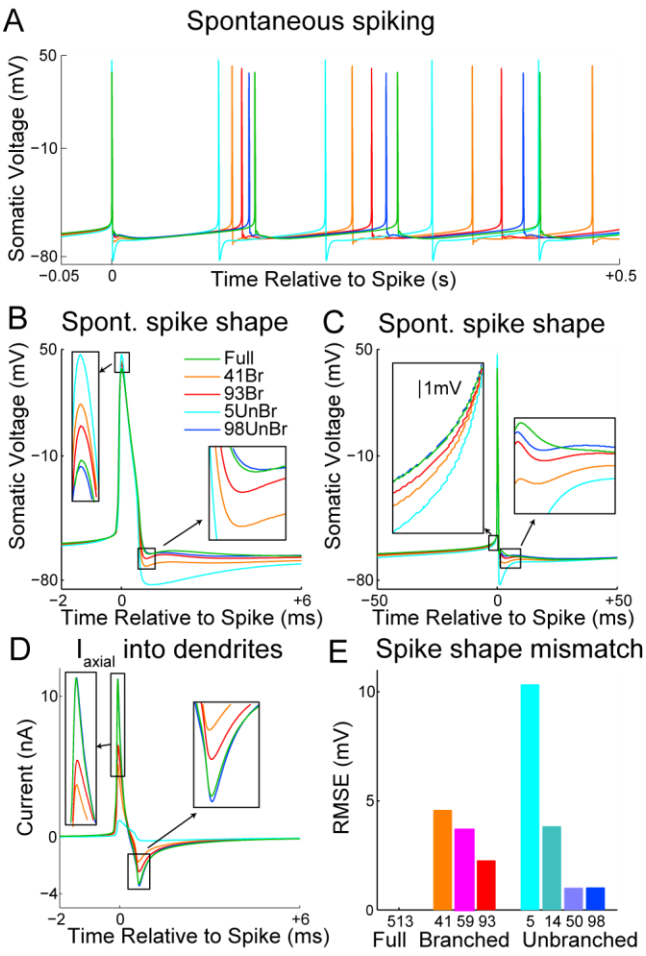

Figure 2.4: Shape analysis of spontaneous somatic APs in fully active models.

Models at all levels of reduction possessed identical somatic, axonal and dendritic conductance densities. A, Spontaneous spiking is shown for the full and reduced models. B, The relative spike heights in the active models (left inset) corresponded directly to the relative mock AP response amplitudes shown in Fig. 2.3A. Models with shorter spike heights possessed shallower fast afterhyperpolarizations (fAHPs) as well (right inset). C, Expanded time scale shows steeper rise time to spike onset in the most reduced models (left inset) and extended differences in fAHP potential (right inset). D, Axial current between soma and dendritic trunk compartments. The spike depolarization led to a large positive current into the dendrites; somatic spike size was increased in models with less axial current due to high Ra values. During the somatic fAHP, the axial current reversed, and current flowing back into the soma from the depolarized dendrites led to a decrease in fAHP amplitude. Therefore fAHP was largest in the most reduced models because they had the highest Ra values into the dendritic trunk compartments directly connected to the soma. E, The 'mismatch' with the full model spontaneous spike shape shown in B was calculated for each model as the root mean squared error (RMSE) of the voltage traces from 2 ms before to 6 ms after the spike peak. Spikes were aligned so that they crossed 0 mV at the same time.

Using the same active conductance parameter set that was shown to reproduce physiological GP neuron activity in the full model (see Methods) for all models, the active full and reduced models each exhibited tonic, regular spontaneous spiking (Fig. 2.4*A*). Spikes were always initiated in the axon compartment due to its high NaF conductance. Despite identical conductance densities, spike shapes differed somewhat depending on each model's morphology. As predicted by the mock AP comparisons, the somatic spikes of the 5comp model were taller than those of the full model (by 7.9 mV). Spikes in the other reduced models were also taller than those in the full model, but not by as much, and they followed the same pattern as for the height of the mock AP (Fig. 2.4*B* left inset). It should be kept in mind, however, that the amount of variability in spike height between the full and reduced models (7.9 mV) was not large relative to the variability seen between different GP cells in vitro (standard deviation = 10.8 mV) (Gunay et al., 2008). Note that AP height depended on the average dendritic compartment length rather than on the preservation of the detailed dendritic branching structure (see Table 2-1). Spike height differences were due to variations in the amount of axial current leaving the soma during a spike (Fig. 2.4*D*, left inset): models with less axial current exiting the soma during a spike (Fig. 2.4*D*, compare positive peaks) possessed taller action potentials (Fig. 2.4*B*, left inset) because more current remained in the soma to charge the somatic membrane. Models with less axial current flow also exhibited slightly more hyperpolarized spike initiation thresholds (Fig. 2.4*C*, left inset) because less positive driving current was able to exit the soma into the dendrites during spike onset. The medium dendritic gNa level in our default full model was too low to propagate active dendritic APs, but a parameter set with high dendritic gNa allowing

active dendritic spiking showed quite similar results for the dependence of spontaneous spike shape on model reduction (Supplemental Fig. 2-1), indicating that these findings generalize to spiking and non-spiking dendrites.

A direct consequence of smaller axial current flows into the dendrites during a mock AP was less depolarization of the dendrites (Fig. 2.3*C*, passive case). Less depolarized proximal dendrites contributed less positive axial current back to the soma immediately following the spike during the fast afterhyperpolarization (fAHP) (Fig. 2.4*D*, right inset). Indeed, fAHPs were deeper in models with smaller axial current flows back into the soma immediately following a spike (e.g. the 5comp model, Fig. 2.4*B* right inset, Fig. 2.4*D* inset). In contrast to the small spike height differences, the difference between the full and 5comp model fAHPs was 17.3 mV, about six times larger than the experimental variability for this measure (Gunay et al., 2008). Deeper fAHPs in the 5comp model lasted for many milliseconds following a spike (Fig. 2.4*C*, right inset). In sum, axial current flow was a key determinant of spike shape differences: the reduced models that exhibited axial current flows most similar to those of the full model (e.g. the 50 and 98comp unbranched models) also provided the best matches to the full model's spike shape (Fig. 2.4*E*). The larger mismatch in the branched models, even the one with 93 compartments, was due to the fact that their trunk dendritic compartments were still electrotonically longer than those of the unbranched models since a large number of compartments was necessary simply to reflect the entire branching structure of the full model (see Table 2-1).

We considered the possibility that manipulation of conductance densities in the 5comp model could allow a better match to the full model's spike shape. The full

model's spike was shorter (by 7.9 mV) and its fAHP shallower (by 17.3 mV) than that of the 5comp model. By hand-tuning the 5comp model's conductance densities, these mismatches in spike height and fAHP depth respectively could be decreased by 97% and 77%. This level of error reduction was achieved through a 4-fold decrease in the somatic and axonal NaF conductance densities and a 16-fold decrease in Kv2, Kv3, and Kv4fast/slow. While our hand-tuning allowed a much better match of spike height and fAHP depth, these conductance density changes also caused the spike width at -20 mV to increase from 0.53 ms to 0.88 ms (the full model spike width was 0.58 ms). Because spike width was a key determinant of calcium entry through HVA channels in the model, increasing the spike width lead to an increase in SK channel activation that secondarily altered multiple model properties. Overall, hand-tuning conductance densities in reduced models away from the full model parameter set always produced trade-offs in our experience, and it was not possible to fully compensate for mismatches incurred by morphological differences. In addition, the channel densities that made the reduced model spike shapes most similar to electrophysiological recordings were several-fold different from the original channel densities in the full morphology, and thus the biological interpretation of such models would need to take this fact into consideration.

2.4.4. Analysis of back propagating APs (bAPs) at different levels of model reduction

A neuron model's bAP amplitudes have important consequences for the modeling of spike time dependent synaptic plasticity (Caporale and Dan, 2008). If a reduced model's bAP amplitudes were appreciably different from those in a full model,

coincident bAPs and EPSPs in the dendrites would fail to evoke similar local responses. To examine the effect of model reduction on bAP amplitudes during fast spiking activity as may be expected for GP neurons in vivo, 75 Hz spiking was elicited in each model by somatic DC injection. We normalized bAP amplitudes to somatic AP height so that models with taller somatic spikes did not mistakenly appear to have more effective back propagation. In most dendritic compartments of the full and reduced models, bAP amplitudes decayed at about the same rate with electrotonic distance from the soma (Fig. 2.5*A*). However, in the most highly reduced models even the trunk dendritic compartments were at a considerable electrotonic distance from the soma (Fig. 2.5*A*), and therefore the initial decrease in bAP amplitude was much more pronounced. A further difference between the reduced and full models was that variability in bAP amplitude for different dendritic branches at a given electrotonic distance from the soma was much larger in the full model. In particular, one full model branch had a greatly increased bAP amplitude (Fig. 2.5A_1, black arrow). Indeed, the bAP amplitude at the end of this branch ($L \approx 0.5$) was 49% of the somatic AP height, while the largest bAP amplitudes observed at this electrotonic position in any branched or unbranched reduced models were respectively only 13% or 16% of somatic AP height. This large bAP disappeared in the full model without dendritic gNa (Supplemental Fig. 2-2*A*), which meant that the large amplitude was due to local amplification by gNa. Thus even when the branching structure of the full morphology was maintained, morphological reduction still resulted in significant functional changes in the presence of active conductances.

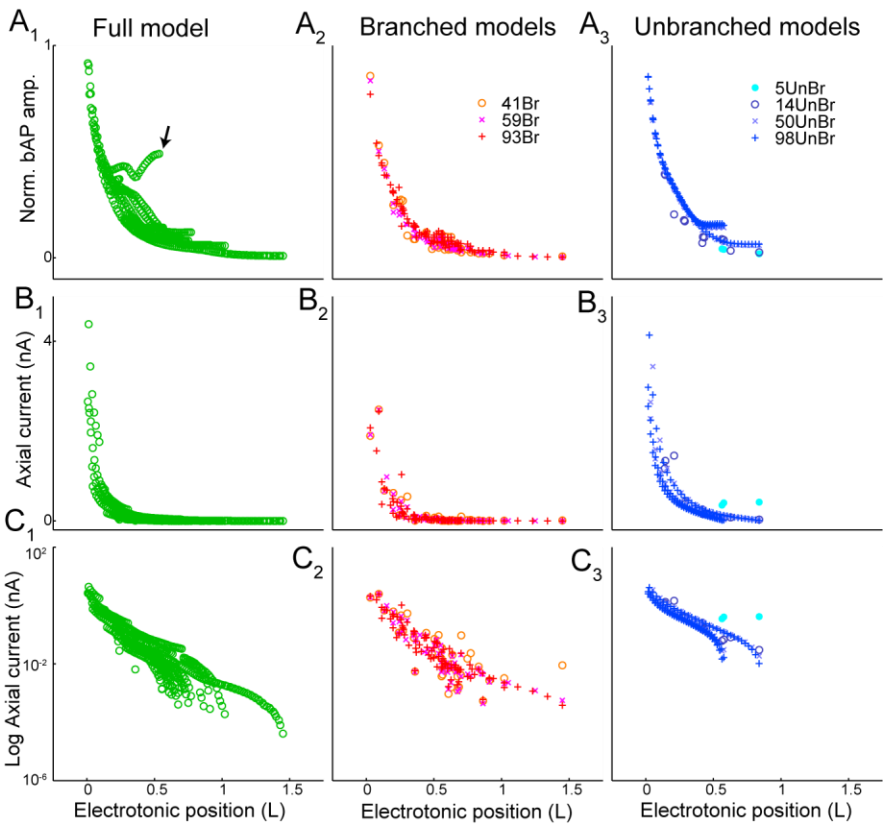

Figure 2.5: Back propagating AP (bAP) amplitudes can be much larger in the full model than in the reduced models due to larger local dendritic high frequency Z_{IN}s.

All models were driven to fire at 75 Hz +- 0.1% with DC somatic injection. A, The bAP amplitude in each compartment was normalized to the soma spike amplitude and plotted against the electrotonic distance from the soma for the full model (A_1), branched models (A_2) and unbranched models (A_3). Most models showed a similar decay in bAP amplitude with electrotonic distance. However, the 5comp and 14comp unbranched models showed much smaller bAP sizes in their proximal dendrites because these compartments were already electrotonically quite distant from the soma. In addition, the full model showed more variable bAP amplitudes in different branches (see black arrow) than even the most detailed branched reduced models. B, The maximum amount of axial current flowing into each compartment during a spike (referred to simply as axial current) is plotted against electrotonic distance from the soma. C, Log scale representation of the plots shown in B. Note that the decay of axial current with electrotonic distance is approximately log-linear and is quite similar between the full and reduced models.

The primary cause of bAPs lies in the propagation of axial current. The peak axial current during a bAP quickly decayed with electrotonic distance at about the same rate in the full and reduced models (Fig. 2.5*B*) such that only a small fraction of the initial axial current at the soma boundary even reached intermediate dendritic positions at 0.5 L (Fig. 2.5B_1). The peak axial current reaching distal locations (e.g. 1.0 L) was quite

variable between dendritic branches (Fig. 2.5*C*) though the variability was diminished by either removing dendritic gNa or setting it to a high density that supported active spike back propagation (Supplemental Fig. 2-2). However, the peak axial current reaching any given compartment did not determine the local bAP amplitude. Instead, the amplitude was primarily determined by the local Z_{IN} at each location. For example, in the full model at 0.54 L, the branch with the largest bAP amplitude (1000 Hz Z_{IN} of 304 MΩ) received only 35% of the axial current received by the branch with the smallest bAP (1000 Hz Z_{IN} of 76 MΩ). Such a large spread in 1000 Hz Z_{IN} was not observed in any of the reduced models, explaining the smaller spread of bAP amplitudes (Fig. 2.5*A*). While the branched reduced models possessed the same branches as in the full model, their 1000 Hz Z_{IN}s were smaller due to their larger compartment sizes, leading to the observed mismatches in bAP amplitudes. These differences between the full model, branched reduced models and unbranched reduced models should be considered when using modeling to study bAPs.

2.4.5. Effects of model reduction on the somatic spike frequency vs. current Injection (fI) curves

The somatic fI curve is a basic neuronal input-output function which is frequently recorded by cellular electrophysiologists due to the important information that it yields about neuronal excitability. Possible mismatches in the somatic fI curve due to model reduction could result in consequential changes with respect to excitability in the presence of synaptic input. To assess the extent of such mismatches, we compared somatic fI curves between the full model and the branched or unbranched reduced models

(Fig. 2.6*A*). All models exhibited spontaneous spiking which could be eliminated by injecting between -31 pA and -41 pA of DC into the soma. For positive current injection amplitudes between 0 pA and 500 pA, the full and reduced models exhibited nearly linear increases in spike rate. However, the somatic fI curve was steeper in some of the reduced models than in the full model. This slope mismatch was related to differences in somatic R_{IN} between the full and reduced models (compare Fig. 2.2*A* with Fig. 2.6*A*). Models with larger somatic R_{IN} allowed more somatically-injected current to charge the somatic and axonal membranes instead of flowing into the dendrites. This difference was most pronounced for the 5comp unbranched model, since this model had by far the highest somatic R_{IN} (Fig. 2.2*A*). Overall, the differences in spike rate between the full and reduced models were small (e.g. spontaneous rate varied by only 2.4 Hz) relative to the variability that is observed between different GP cells recorded in vitro (standard deviation for spontaneous rate = 5.9 Hz) (Gunay et al., 2008). Therefore our data indicate that somatic fI curve mismatches are not one of the important limitations of reduced models, with the possible exception of highly reduced models with severely limited axial currents such as our 5comp model.

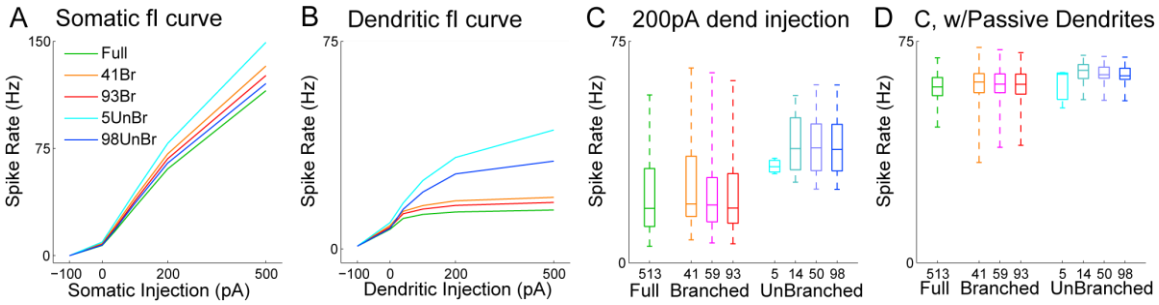

Figure 2.6: The spike frequency response to somatic and dendritic DC injection (fI curve) at different levels of model reduction.

DC injection amplitudes ranged from -100 pA to +500 pA to elicit the full physiological range of spike rates. A, fI curve of each model for somatic current injections. Models with higher

somatic RINs (see Figure 2.2A) exhibited steeper somatic fI curves. Note that subdividing the compartments of the reduced models allowed closer matches to the somatic fI curve of the full model. B, fI curve of each model for DC injection into a sample dendritic compartment at an electrotonic distance of 0.83 L from the soma. The injected compartment was positioned on the same sub-branch in the full and branched reduced models and on the same major branch in the unbranched reduced models. Note that the branched reduced models closely matched the dendritic fI curve of the full model while the unbranched reduced models did not provide close matches. C, Box plots for distributions of spike frequency responses for 200 pA DC injections into each dendritic compartment of each model. The median spike frequency response to dendritic injection was much higher in the unbranched reduced models than in either the full model or the branched reduced models. The minimum spike frequency response to dendritic injection was also much higher in the unbranched reduced models than in either the full model or the branched reduced models. D, Same as C except that all channels were removed from the dendrites. Note the much closer match between all models and the strong correspondence to the relationships shown in Fig. 2.2B.

We again considered the possibility that the somatic fI curve of the 5comp model could be improved relative to that of the full model by hand-tuning its conductance densities. Indeed, by decreasing axonal NaP by 12.5% and increasing somatic SK by 50%, the 5comp model's somatic fI curve closely matched that of the full model. However, these manipulations did not appreciably decrease the discrepancy between the 5comp model's spike rate responses to dendritic current injection relative to those of the full model: this discrepancy will be addressed in the next section.

2.4.6. Effects of model reduction on fI curves for dendritic current injection

While the somatic fI curve is an important measure of the excitability of a neuron, it does not take into account input processing taking place in active dendrites. Active dendrites are capable of many types of input processing, depending on their precise morphology and their complement of ion channels (London and Hausser, 2005). As a first step towards characterizing the influence of model reduction on dendritic processing, we recorded the spike frequency with different dendritic DC injection amplitudes at a

relatively distal location (~0.8 λ) in each model. As shown in Fig. 2.6*B*, the dendritic fI curves were much steeper in the unbranched reduced models than in the full or branched reduced models. To test whether mismatches in dendritic fI curves depended on the particular dendritic location chosen, we injected 200 pA of DC into every dendritic compartment of each model and compared the distribution of spike frequencies between models (Fig. 2.6*C*). For all dendritic compartments, the median spike frequencies of the unbranched reduced models were about twice as large as those in the full or branched reduced models (Fig. 2.6*C*). In addition, the minimum spike frequency was much larger in the unbranched reduced models than in the full or branched reduced models (Fig. 2.6*C*). However, this difference was sensitive to the dendritic gNa level: with high dendritic gNa, the full model responded to dendritic current injection with high spike frequencies that matched the unbranched models, although the spread of spike frequency responses remained much higher in the full model (Supplemental Fig. 2-4*C*). Overall, these results showed that differences between full and reduced models in their dendritic fI curves were large, and furthermore depended on the complement of ion channels.

Next, we sought to understand more fully the relationship between dendritic current injection and somatic spike rate. To examine the possibility that different spike frequency responses were simply related to the electrotonic distance of each injected compartment to the soma, we compared the spike rate response during 200 pA DC dendritic injection to the electrotonic position of each injected dendritic compartment. Perhaps surprisingly, there was considerable variability between spike rate responses to current injections at matching electrotonic positions in different sub-branches of the full model and branched reduced models, but not for the unbranched reduced models (Fig.

2.7*A*). Similar levels of variability were seen when we compared the relationship between local dendritic R_{IN} and electrotonic distance from the soma (Fig. 2.7*B*), which prompted us to consider that local dendritic R_{IN} might a better predictor of spike frequency responses. Indeed, we found a very close relationship between high values of local dendritic R_{IN} at the site of current injection and low values of somatic spike frequency regardless of model reduction level (Fig. 2.7*C*). Since the unbranched models lacked compartments with high local R_{IN}s due to their collapsed branching structures (Fig. 2.2*C*), their minimum spike frequency responses to dendritic current injections were higher (Fig. 2.6*C*).

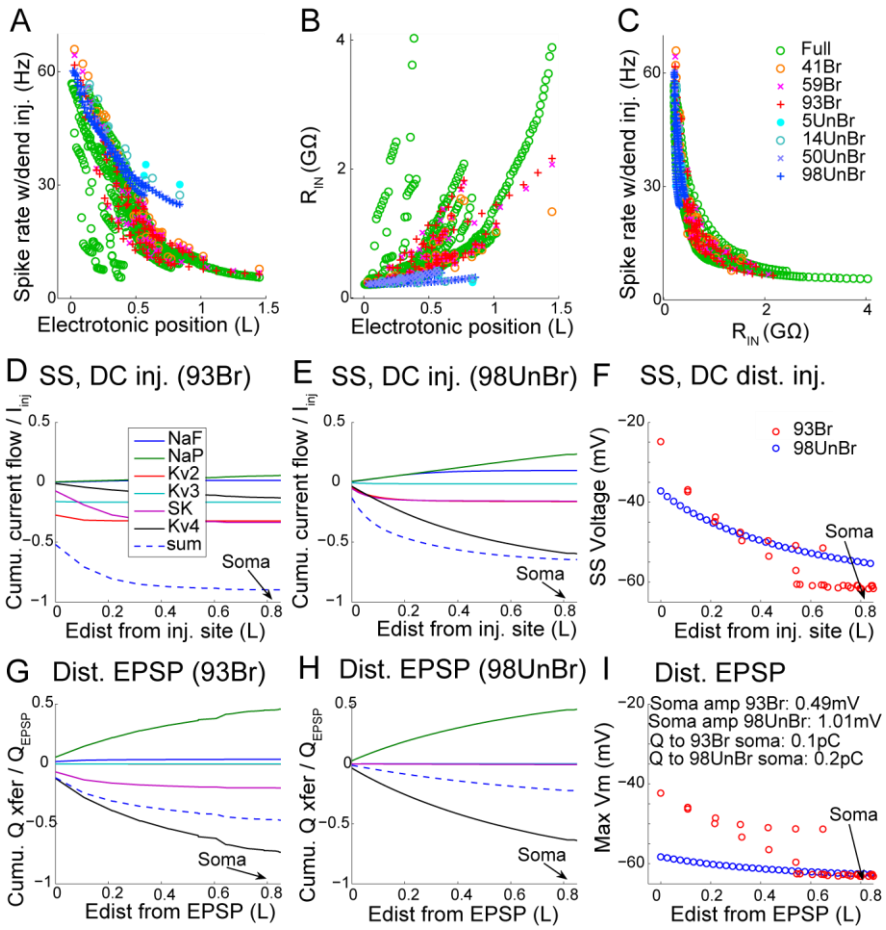

Figure 2.7: R_{IN} was a better predictor than electrotonic position of the spike rate response to dendritic injection due to the activation of dendritic conductances.

The R_{IN} of a dendritic compartment was calculated as for Fig. 2.2. A, The spike rate response during 200 pA DC injection into each dendritic compartment depended weakly on electrotonic distance from soma. B, The R_{IN} of a dendritic compartment also depended weakly on electrotonic distance. C, The spike rate response during 200 pA DC injection into a dendritic compartment depended strongly on the injected compartment's R_{IN}. D-F, A 200 pA DC injection was applied to sites approximately 0.8 L from the soma in both models on the same major branch. In each plot, "Edist from inj. site" refers to the electrotonic distance of another compartment in the model from the injection site. $Kv4_{fast}$ and $Kv4_{slow}$ had similar profiles in all cases, so we summed them and plotted the sum as 'Kv4'. Some conductances were not plotted because they were not activated noticeably by these protocols. The sum of all active currents is plotted as a blue dashed line. The electrotonic position of the soma relative to the injection or EPSP generation location is noted in each plot. D,E, Cumulative current flow refers to the sum total of current flow at steady state ('SS') through each conductance for all compartments that are within a particular electrotonic distance of the injection site. Cumulative current flow was normalized to the amplitude of current injected ('Cumu. Current flow / I_{inj}'). F, The steady state voltage was plotted in each compartment. G,H, Similar to D and E, except that instead of DC injection, an EPSP was generated in the same compartment by applying a 1nS excitatory synaptic conductance. Cumulative charge transfer refers to the sum total of charge transferred through each conductance during the first 100 ms following EPSP onset for all compartments that are within a particular electrotonic distance of the distal EPSP initiation site. The cumulative charge transfer was normalized to the charge transferred into the model by the excitatory conductance ('Cumu. Q xfer / Q_{EPSP}'). I, The maximum voltage reached from conductance onset to 200 ms later was plotted for each compartment. 'Soma amp 93Br' refers to the maximum voltage reached in the 93comp soma during the 200 ms period following EPSP

generation minus the steady state voltage, while 'Q to 93Br Soma' refers to the total amount of axial charge reaching the soma during this period.

We hypothesized that the large depolarization caused by positive current injection at a site with high local R_{IN} would cause increased activation of dendritic potassium conductances, allowing more of the injected current to leak out and thus leading to a lower spike rate in the branched models relative to the unbranched models. To understand which channels might contribute to this phenomenon, we removed both somatic and axonal active conductances. We then recorded the total currents flowing through each type of dendritic conductance at steady state during 200pA DC injection into distal dendritic compartments at approximately the same electrotonic position in the 93comp branched (high R_{IN}) and 98comp unbranched (low R_{IN}) reduced models. As we suspected, local dendritic voltages and local active current flows were larger at the high R_{IN} injection site in the 93comp model than at the low R_{IN} injection site in the 98comp model (Fig. 2.7*D-F*). The dendritic voltage in the 93comp model decayed faster with electrotonic distance from the injection site than in the 98comp model due to larger local dendritic current activations. These large local current activations were primarily due to potassium conductance, which shunted away much of the injected current thus preventing it from reaching the soma. Indeed, about 50% of the injected current was shunted away in the injected compartment alone in the 93comp model, while only about 10% was shunted away in the injected compartment in the 98comp model (Fig. 2.7*D,E*). Consequently, the steady state voltage reached in the soma of the 93comp model was about 5 mV more hyperpolarized than the soma of the 98comp model, despite equivalent electrotonic positions of current injection (Fig. 2.7*F*). The detailed spatial pattern of

voltage-gated current flow induced in active dendrites by current injection was actually quite complex, since some currents with a high voltage threshold such as Kv2 (red trace in Fig. 2.7*D,E*) were activated predominantly at the site of injection by a high local voltage transients, whereas others with a lower voltage activation range such as Kv4 (black trace) produced the bulk of current further away from the stimulation site. Such complex spatial dependencies between voltage transients and current activation indicate that any morphological model simplification will lead to some degree of mismatches in dendritic current.

Because DC dendritic injection is not very similar to synaptic input for a neuron in vivo, we also tested to what extent dendritic R_{IN} would affect the activation of voltage gated conductances due to an excitatory postsynaptic conductance to elicit an EPSP (Fig. 2.7*G-I*). Similar to the case with DC injection, we found that the EPSP was larger at the generation site in the 93comp model, that more of the EPSP's charge was shunted locally in the 93comp model, and that the EPSP decayed faster with electrotonic distance. Indeed, the increased dendritic shunting of charge through active conductances in the 93comp model resulted in a somatic EPSP that was less than half as large as that recorded in the 98comp model. Based on these results, comparable synaptic events in branched or unbranched models should not be expected to yield equivalent somatic responses in the presence of active dendritic conductances.

To confirm that dendritic conductances were primarily causing the differences in spike rates with dendritic DC injection, we removed all dendritic conductances and reproduced the box plots shown in Fig. 2.6*C*. As expected from the above analysis, passive dendrites allowed close matches between all models regarding spike rate

responses to dendritic DC injections (Fig. 2.6*D*). Because the reduction of local dendritic R_{IN} is unavoidable when multiple branches are collapsed, these results suggested that reduced models with dendritic active conductances but without a full branching structure will always show noticeable mismatches in their responses to dendritic synaptic input due to differential activation of voltage-gated conductances. These mismatches can lead to either decreased or increased spiking based on the relative predominance of inward or outward dendritic currents.

2.4.7. Comparison of spike frequency response to synaptic inputs at a range of input frequencies across models.

The integration of distributed synaptic inputs into spiking output is one of the fundamental computational functions of a neuron (Destexhe et al., 2003; Gulledge et al., 2005). Accurate synaptic integration relative to a full model or biological neuron is particularly important for a reduced model that will be incorporated into network simulations. A first order approximation of the input/output function of a neuron model is frequently represented by fF curves, which compare spike frequency vs. input frequency at different mixes of inhibition and excitation. We generated fF curves for all models by recording the spike frequencies for increasing rates of asynchronous excitatory input to all dendritic compartments at 3 levels of inhibition. We applied identical synaptic conductance activation patterns between all models (see Methods). We found that the fF curves of all reduced models matched the full model better than the fI curves for dendritic current injection had suggested (Fig. 2.8*A*, compare to Fig. 2.6*B,C*). Nevertheless, the unbranched models showed a somewhat larger spike frequency increase

with increasing excitatory input rates as suggested by the dendritic fI curves, whereas the divided (59comp and 93comp) branched reduced models presented a close approximation to the fF curves of the full model. As we observed with dendritic fI curves, the degree to which the fF curves matched between the models was sensitive to the dendritic gNa level. With high dendritic gNa, no reduced model was able to match the steep fF curves of the full model due to differences in dendritic spike initiation and propagation (Supplemental Fig. 2-5).

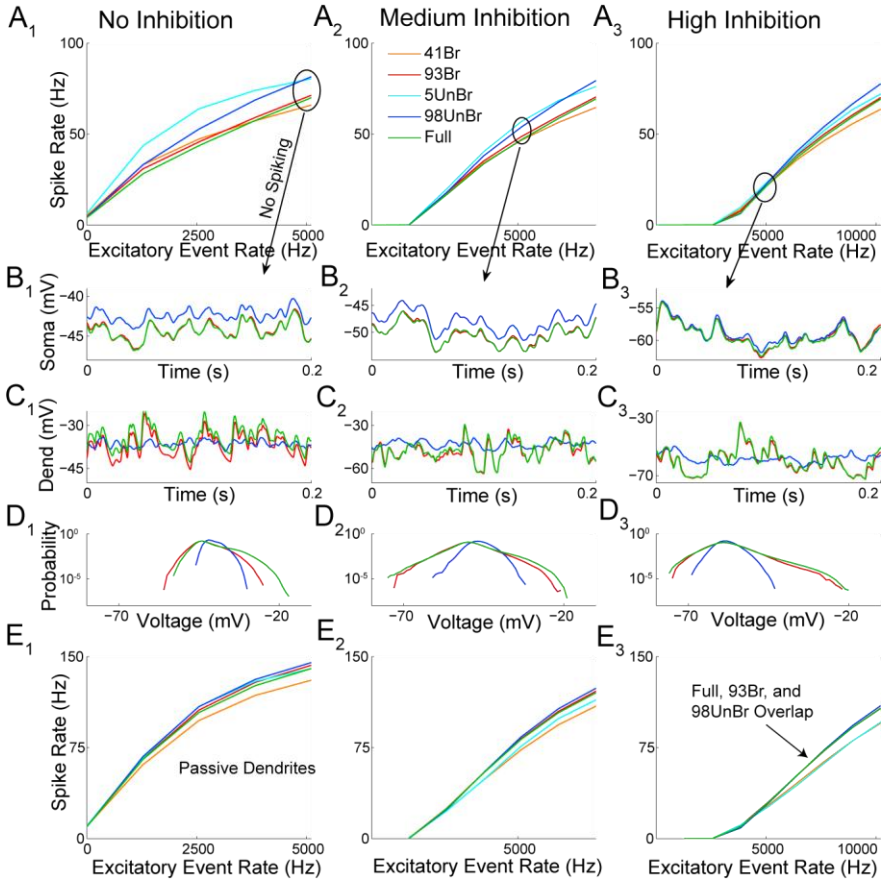

Figure 2.8: The spike frequency (f) responses of the full model to different event frequencies (F) of synaptic input (fF curves) were well matched by the divided branched reduced models but less well matched by the other reduced models.

A, With asynchronous excitation, the divided branched reduced models consistently provided the best match to the fF curves of the full model (59comp model responses not shown, but similar to those of the 93comp model). Note that the fF curves of the unbranched models were generally steeper than those of the full model, but that the mismatch depended on the precise

combination of excitation and inhibition. 'No', 'Medium', and 'High' inhibition respectively refer to average rates for each inhibitory synapse of 0, 10, and 20 Hz. Each fF curve was constructed from 100 s simulations for each data point. B-D, somatic and axonal conductances were removed to prevent spiking. B, Short somatic voltage traces are shown in each type of model. Note that the full and branched somatic voltages were practically identical while the unbranched 98comp model exhibited slightly different fluctuations with no or medium inhibition. Further note the correspondence of these somatic voltage fluctuations to the relative firing rates of each model. C, Short voltage traces are shown from an example dendritic compartment at approximately the same electrotonic position and branching structure (if possible) in each type of model. The full and branched dendritic compartments experienced larger voltage fluctuations than did the compartment in the unbranched model. Note the close correspondence of the full and 93comp branched reduced model's dendritic voltage fluctuations. D, The probability that a particular voltage was reached by any dendritic compartment at any time during synaptic input is plotted for each model. The ranges of voltages reached by the dendrites of the full and branched models were larger than the range of voltages reached by the dendrites of the unbranched model. E, After removing all active dendritic conductances, the fF curves were reproduced. Note the much better fF curve matches, particularly between the 98comp unbranched reduced model and the full model.

To understand the fF curve mismatches of the unbranched models with medium dendritic gNa, we studied the somatic and dendritic voltage fluctuations of the 93comp, 98comp and full models after removing their somatic and axonal active conductances (Fig. 2.8*B-D*). The somatic voltages were shifted relative to one another in a manner consistent with the relative firing rates in the fF curves. However, the magnitude of somatic voltage fluctuations was similar between the full and reduced models (Fig. 2.8*B*). In contrast, the dendritic voltage fluctuations in the unbranched 98comp model were much smaller than in the full or branched 93comp model at each level of inhibition (Fig. 2.8*C,D*; note the close similarity between the local fluctuations of the full and 93comp branched models). We hypothesized that these different dendritic voltage fluctuations influenced dendritic conductances in a complex manner and prevented the 98comp model from precisely matching the fF curves of the full model. To test this, we removed all dendritic conductances from each model and reproduced the fF curves. As we predicted, the fF curves of the full and reduced models without dendritic conductances were much more similar to each other than in the case with dendritic conductances (Fig. 2.8*E*).

2.4.8. Many of the precise spike times of the full model were preserved by the branched and unbranched reduced models

While synaptic rate coding is used for many neural computations, some circuits such as those involved with processing transient sensory inputs must use the information contained in the timing of the first spike (VanRullen et al., 2005). In network models of circuits employing precise spike timing as a coding mechanism, the exact firing times of the component neuron models therefore become important. If the spike times of a reduced branched or unbranched model differ from those of a biological neuron or full model, the degree of spike time preservation should be understood before a particular morphological reduction method is used to construct neurons for such networks. Therefore, we evaluated the preservation of precise full model spike times by branched or unbranched reduced models in the presence of identical synaptic inputs.

To study the precision of spike timing with synaptic inputs, we first constructed a set of asynchronous distributed inputs where each of the 511 excitatory synapses was randomly activated with a mean rate of 5 Hz, and each of 511 inhibitory synapses with a mean rate of 10 Hz. Because input synchronization is generally thought to be an important aspect in neural coding and occurs naturally for example due to oscillatory activity (Ward, 2003), we also constructed a synaptic stimulus in which clusters of synapses were activated synchronously (see Methods). Spike time preservation was defined as the percentage of the full model's spikes that were generated by the reduced model within ±5 ms of the full model's spike time, a method we previously employed in dynamic clamp studies to examine spiking precision (Gauck and Jaeger, 2000).

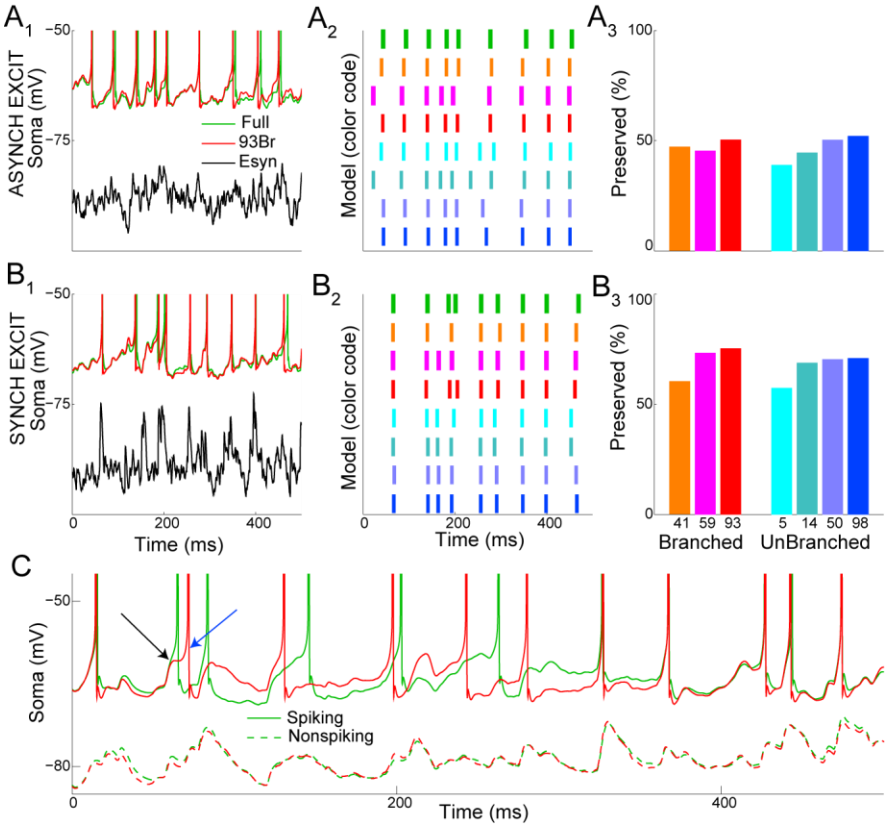

Figure 2.9: Precise full model spike times were often preserved by the reduced models in the presence of synaptic input.

A, Spike time preservation during asynchronous synaptic bombardment. A1, Somatic voltage traces for the full model and 93comp branched reduced model are shown along with the combined synaptic reversal potential (Esyn, shifted down by 20mV for easier visualization). A2, Raster plot showing the spike times for each model during the simulation segment in A1. A3, The percent of preserved spikes was generally about 50% for all the reduced models. B, Same as A, but with synchronous excitation. Note the improved preservation percentages for each reduced model. Further note that none of the reduced models preserved more than about 75% of full model spike times. C, Somatic voltage traces are shown in the full and 93comp models during a short period when precise full model spike times were not preserved. The dashed traces represent the somatic voltages of the models without somatic or axonal conductances (nonspiking, shifted down by 20 mV to aid visualization), while the solid traces are from the active models. Note the extremely close match of the nonspiking somatic voltage fluctuations, the point when the full model spikes but the 93comp model does not (black arrow), and the 93comp spike which follows soon after (blue arrow). Synaptic input distributions were identical to those used for Fig. 2.8. Medium excitation (5Hz) and medium inhibition (10Hz) were used for all panels of this figure. Preservation of full model spike times was calculated as the percentage of the full model's spikes that were generated by the reduced model within ±5 ms of the full model's spike time. The colors used in the raster plots in this figure were the same as those used for the rest of the figures.

Interestingly, preservation of ±5 ms spike timing did not vary widely between the branched and unbranched reduced models (Fig. 2.9*A1-3*). Preservation was generally about 50% with asynchronous excitation (Fig. 2.9$A_{1\text{-}3}$), and from 50% to 75% with synchronous excitation (Fig. 2.9$B_{1\text{-}3}$), for branched or unbranched reduced models. Coincident excitatory inputs increased spike time preservation because powerful events were more likely to overcome small differences in activity between the models to drive spikes at a precise time. With spike time preservation, as with previous functional measures, the dendritic gNa level was an important determinant of how well the reduced models matched the full model. Preservation of spike timing was greatly diminished by high dendritic gNa whether inputs were asynchronous or synchronous. With 10Hz inhibition and 5Hz excitation, spike time preservation for the high-dendritic-gNa models was often less than 20% due to differences in dendritic spike propagation and initiation with the full model (data not shown). Conversely, removing dendritic gNa altogether caused spike time preservation to improve by 5% relative to the case with medium dendritic gNa for the 93comp model, suggesting that dendritic sodium was amplifying coincident EPSPs differently in the different models (data not shown). Removing the remaining dendritic conductances did not further improve spike time preservation for the 93comp branched model, most likely because close somatic voltage fluctuation matches were observed even with all dendritic conductances present (e.g. Fig. 2.8*B*). In light of the close somatic voltage fluctuation matches between the full and 93comp branched model, the inability of the 93comp branched model to preserve a greater proportion of the full model's spike times was surprising.

To understand the inability of the 93comp branched model to preserve more than 75% of the full model's precise spike times even in the presence of synchronous coincident excitatory inputs, we compared somatic voltage responses from the models that possessed the full complement of somatic and axonal conductances (spiking) to responses from models without somatic or axonal conductances (nonspiking). We observed a close match between the somatic responses of the full and 93comp models in the nonspiking case (Fig. 2.9*C*, dashed traces). However, in the spiking models with exactly the same synaptic inputs, one model would occasionally fire a spike while the other model would not quite reach threshold (e.g. Fig. 2.9*C*, black arrow). If a spike-triggering synaptic event occurred for both models immediately after this event, then the model that just fired a spike would not fire again, while the other one would (e.g. Fig. 2.9*C*, blue arrow). This kind of sequence tended to cause spikes in the subsequent few hundred milliseconds to be misaligned between the two models and accounted for most of the unpreserved spike times. Indeed, due to the fact that near-threshold events can lead to spike initiation in one condition but fail to cause spike initiation in a closely parallel condition, a fully precise control of spike timing by synaptic input may be impossible. This observation is supported by previous work with dynamic clamp stimuli, showing that the same neuron recorded in a brain slice with multiple repetitions of the same conductance pattern also only shows a preservation of about 60% of spike timing at a precision of 5 ms (Gauck and Jaeger, 2003).

2.4.9. Conductance parameter sets yielding disparate reduced model output can be mapped back into the full model to produce similar output

Researchers using full models commonly face the problem of hand-tuning conductance densities to match target output: this is always a laborious task and dissatisfying in that only a single - possibly arbitrary - solution is found. Therefore, there has been great interest in finding algorithms to optimize the conductance densities of a model automatically (Vanier and Bower, 1999; Huys et al., 2006) and to determine the parameter space of similar solutions with database approaches (Prinz et al., 2003; Prinz et al., 2004; Gunay et al., 2008). However, even with such algorithms it is still demanding to find a suitable parameter set for a full model because of the long simulation times required to run thousands of parameter combinations in such models. This time requirement can be drastically decreased by applying the search algorithm to a reduced model, as long as the resulting conductance densities can be mapped back into the full model to produce similar output.

To examine which reduction strategy could be used to efficiently search the parameter space of the full model, 100 random parameter sets were generated by varying each conductance density independently between 25% and 400% of its default value. In the reduced models, these parameter sets produced widely varying somatic and dendritic fI curves and spike shapes (e.g. Fig. 2.10A_1). Of these parameter sets, two parameter sets were chosen to illustrate the quality of mapping between the full and reduced models; these two sets yielded quite different somatic and dendritic fI curves and spike shapes (Fig. 2.10, 'RandSet1' and 'RandSet2'; for conductance densities see Supplemental Table 2-3).

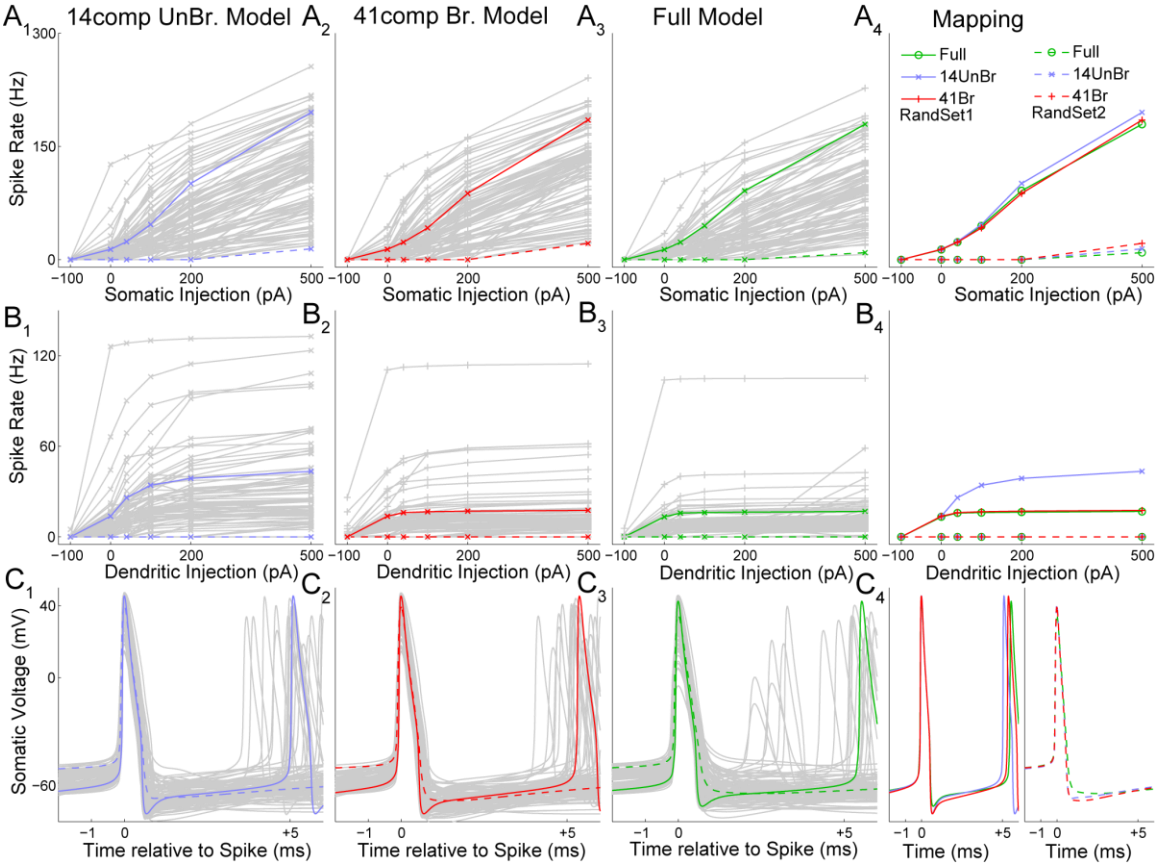

Figure 2.10: Reduced model activity patterns generated by many random conductance density sets were reproduced by the full model.

One hundred conductance density parameter sets were randomly generated by varying each conductance density between 25% and 400% of its original value. Two of these were selected to illustrate mapping between morphologies, because they yielded very different output. These two were referred to as randSet1, a parameter set producing a steep somatic fI curve, represented by colored solid lines, and randSet2, a parameter set producing a shallow somatic fI curve, represented by colored dashed lines. The remaining 98 random parameter sets are displayed in light gray. Model spike shapes were compared during 500 pA somatic DC injection because this level of current injection caused every morphology to spike with each random parameter set tested. A1,B1,C1, Each random parameter set was inserted into the 14comp unbranched morphology. For each parameter set, the somatic fI curve (A_1), distal dendritic fI curve (B_1) and spike shape during 500 pA somatic injection (C_1) are displayed. Note the wide range of fI curve gains and spike shapes. A_2,B_2,C_2, Same as the first column but for the 41comp branched morphology. While the somatic fI curves and spike shapes were similar between the two morphologies, the distal fI curve gains were generally smaller in the 41comp than the 14comp morphology. A_3,B_3,C_3, Same as the first two columns but with the full model morphology. Note that the somatic fI curves and spike shapes were quite similar to those observed in the reduced morphologies, while the dendritic fI curves from the full morphology were most similar to those of the 41comp branched morphology. A_4,B_4,C_4, The somatic fI curves, distal fI curves, and spike shapes in response to 500 pA somatic injection were superimposed for all 3 morphologies for the randSet1 and randSet2 conductance density parameters. Note that mapping back to the full morphology from either type of reduced morphology (14comp unbranched or 41comp branched) was successful for the somatic fI curves and spike shapes, but that mapping of the

dendritic fI curves was only successful from the 41comp branched morphology back to the full morphology.

To compare mapping quality between reduced models, we calculated the root mean squared error (RMSE) between the full and reduced model output for each measure (6 rate points for each fI curve and 801 voltage points for each spike shape) for all 100 random parameter sets. This yielded a set of 100 RMSEs for each measure in each reduced model. For the branched reduced models, we found that there were no significant measure improvements when switching from the 41comp model to the 59comp model. In contrast, for the unbranched reduced models, we found that using the 14comp model instead of the 5comp model yielded significant improvements in the median somatic fI curve RMSE (by 12.6 Hz, p = 2.9e-7, Mann-Whitney U test) and in the median spike shape RMSE (by 6.0 mV, p = 9.7e-13, Mann-Whitney U test). These measures also improved significantly when using the 50comp model instead of the 14comp model, but the improvements were only about half as large as those achieved when switching from the 5comp to the 14comp model. In contrast, using the 98comp model instead of the 50comp model did not yield significant improvements for any measure.

To illustrate the quality of mapping between the full and reduced models, we chose to present the 14comp unbranched and the 41comp branched models because they provided the best mix of computational efficiency and accuracy for their respective reduced model types. The somatic fI curves and spike shapes were very well preserved when parameter sets were mapped from the 14comp or 41comp models back into the full model (Fig. 2.10*A*,*C*). Note that even the doublet firing of the full model with randSet1

was preserved by both reduced models (Fig. 2.10*C*$_4$). In contrast, the dendritic fI curves were not closely preserved when mapping the parameter sets from the 14comp unbranched reduced model to the full model but were closely preserved when mapping from the 41comp branched reduced model to the full model (Fig. 2.10*B*$_4$). Indeed, the median dendritic fI curve RMSE was 7.2 Hz larger for the 14comp model than for the 41comp model ($p = 2.6e\text{-}9$, Mann-Whitney U test). The differing ability of the branched and unbranched reduced models to map dendritic responses back to the full model was very similar to the differing ability of the two types of reduced models to match the dendritic responses of the full model with the tuned parameter set (Fig. 2.6). The similar deviations between models for these 100 randomly generated parameter sets support the general validity of our analysis tracing these differences back to axial current and dendritic R_{IN} mismatches.

Overall, we found that identical conductance densities allowed our unbranched reduced models to map somatic input output dynamics back to the full model, while the branched reduced models additionally allowed dendritic input driven somatic output dynamics to map back to the full model.

2.5. Discussion

We developed a principled strategy to construct branched or unbranched reduced dendritic neuron models with few compartments and multiple active conductances that allowed us to keep the same channel densities as in a full morphological model. Using these models we demonstrate that full model responses to somatic stimuli can be matched well by both branched and unbranched reduced models. In contrast, because of

unavoidable differences in the local dendritic input resistance of unbranched reduced model dendrites, responses to dendritic input are less well matched by this type of model if dendrites contain voltage-gated currents, even if the remaining major dendrites are subdivided into many compartments. Some full model properties could not be matched even by branched reduced models, in particular when it came to matching either bAP amplitudes with medium dendritic gNa or spiking responses to synaptic input with high dendritic gNa. We found that particular aspects of the passive structure of reduced models explained particular unavoidable mismatches with full model activity. Specifically, the lumping of axial resistances in models with few compartments led to mismatches in spike shapes and fI curves, while local dendritic R_{IN} and Z_{IN} differences led to mismatches in responses to dendritic stimuli and bAP amplitudes.

Despite these mismatches, we show that many aspects of full model activity, including rate and time coding with dendritic inputs, can be well replicated by principled model reduction strategies and that different sets of voltage gated conductances result in matching activity patterns for each type of model.

2.5.1. Principles of morphological reduction

In passive models, precise input responses can be maintained if the dendritic tree of a full model meets two criteria: 1) all branches follow the 3/2 power branching rule and 2) there is equal electrotonic length from the soma to each dendritic tip (Rall, 1959, 1964). Like most realistic dendritic trees, the dendritic tree of the full GP model did not meet either of these criteria. Furthermore, a principled understanding of what can and cannot be preserved by active model reductions is not yet available. It is certain,

however, that one can't preserve all response properties in a morphologically reduced active model. Most notably, local voltage responses with dendritic input and hence activation of local active properties can't be completely preserved due to changes in local input resistance.

To understand the extent to which active full model dynamics can be preserved by morphologically reduced models, we chose to examine the consequences of two particular morphological reduction methods to create simplified dendritic neuron models, one that preserved detailed dendritic branching structure and one that did not. Different strategies have been employed among previously used dendritic morphological reduction methods, usually without a detailed examination of the consequences. Some studies use reduced models that maintain only a qualitative relationship between full and reduced morphologies without preserving any particular morphological features (Traub et al., 1991; Wilson and Bower, 1992; Davison et al., 2000). Another study examined the reduction of a full model with somatic but not dendritic conductances carefully, and described a method that conserves the full model Ra at the expense of TSA (Bush and Sejnowski, 1993). Previous studies have also employed reduction methods that preserve the TSA and R_{IN} of the full model while ignoring its Ra (Destexhe, 2001; Tobin et al., 2006). Our morphological reduction methods were similar to those of (Destexhe, 2001) and (Tobin et al., 2006), because our reduced models preserved full model TSA and approximated somatic R_{IN} when compartments of the most reduced models were sequentially subdivided. In addition, we preserved the electrotonic length of major dendritic branches (our unbranched models) or of every dendritic branchlet (our branched models). Our method, as with the methods of Tobin and Destexhe, can be used to

construct reduced models both from previously existing full models, but also to construct reduced models directly from reconstructed morphologies and electrophysiological data. Furthermore, our method, like that of Tobin et al, allows channel densities to be mapped bi-directionally between full and reduced models to produce matching electrophysiological activity with somatic stimulation at all levels of model reduction. This capability allows our reduced models to be used as fast search engines of full model parameter space.

2.5.2. The suitability of different levels of model reduction for different applications

2.5.2.1.If complex dendritic processing is not required, then unbranched reduced models suffice:

Computational efficiency is an important consideration when choosing which neuron models to incorporate into large networks, and in this respect unbranched reduced models are preferable to branched reduced models because far fewer compartments are needed to yield satisfactory matches to somatic input-output functions. For example, the unbranched reduced models presented here, particularly the 14comp model, could be incorporated into existing GP network models which currently use single compartment or simpler models (Terman et al., 2002; Rubchinsky et al., 2003). These models replicated the rate coding function for somatic current injection well without altering the channel densities of the full morphological model. Thus, they would allow the study of how individual voltage-gated conductances may contribute to important features of somatic processing. Of course, if mathematical tractability of analyzing network activity patterns

is desired, then even more simplified neuron models such as exponential integrate and fire neurons or low dimensional dynamical system models are preferable (Izhikevich, 2004; Herz et al., 2006).

2.5.2.2.Network models in need of accurate synaptic coding with active dendritic conductances can employ branched reduced models:

We showed that branched reduced models can match the spiking responses of the full model to dendritic current injection or synaptic input quite well, while the unbranched reduced models provided less precise matches. However, the matches even of branched reduced models became significantly worse if a high level of dendritic gNa allowed dendritic spike initiation. Overall, we found no reduced model that could accurately reproduce the pattern of dendritic spike initiation shown by the full model, since this response is highly sensitive to the amplitude of local dendritic voltage fluctuations, which are not generally matched by reduced models due to unavoidable deviations in local input resistances. In contrast, bAPs could be matched fairly well in branched reduced models, although in a particular regime of intermediate dendritic gNa densities some branches showed increased amplification of bAPs only in the full model. The interaction of bAPs is often considered important for spike time dependent plasticity rules (Gulledge et al., 2005; Letzkus et al., 2006), which could therefore generally be employed in network models using branched reduced models, while unbranched models would be less suitable (though not completely inaccurate).

2.5.2.3.Applications that involve locally non-linear dendritic processing should only use full models:

Our analysis of the dendritic properties of reduced and full models revealed that dendritic R_{IN}s, and especially Z_{IN}s for brief or fast-changing signals, cannot be matched for all regions of the dendrite in any model reduction. The local dendritic Z_{IN}s determine the local voltage response to synaptic input and therefore directly influence the amount of activation of voltage-gated conductances. This is particularly apparent in models that allow dendritic spike initiation due to a high dendritic gNa, but also becomes important for fast transient events like bAPs.

2.5.2.4.Using reduced models to search the channel density parameter space:

Several studies have shown that it is of significant interest to explore the parameter space of full morphological models through evolutionary algorithms (Achard and De Schutter, 2006) or database methods (Prinz et al., 2003; Gunay et al., 2008). A large number of simulation runs are also required to determine the sensitivity of a model to channel density variations (Weaver and Wearne, 2008). These methods are computationally expensive to carry out in full morphological models. Because our model reduction method was designed so that channel densities can be mapped back to full models, it can increase the efficiency of parameter space exploration by 10 to 100 fold.

2.5.3. Conclusion

Reduced models are widely used, particularly in network simulations due to their computational efficiency. Careful validation of dendritic activity in reduced models is

likely important to achieve biologically realistic processing in large network simulations. Our findings indicate that carefully constructed reduced models with 10-50 times fewer compartments than a full morphological model can accurately reproduce somatic spontaneous and most synaptically driven activities, while extremely simplified 1-5 compartment models cannot. While some deviations from full morphological models were found for all reduced models, these were generally no larger than the biological variability of the same features in the same cell type. The detailed dendritic branch structure made important contributions to processing only in the presence of strong dendritic non-linearities, such as local Na^+ spike initiation, and should be considered in models employing such mechanisms.

2.6. Supplemental Material

2.6.1. Supplemental Figures

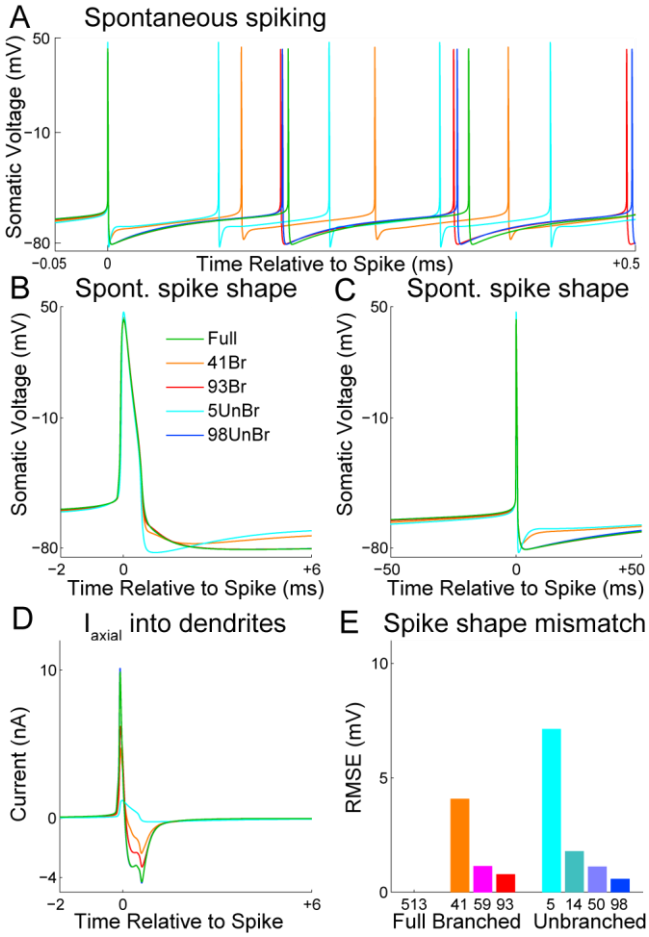

Supplemental Figure 2-1: High dendritic gNa density did not affect the ability of the reduced models to match the full model's spike shape.

A, Spontaneous spiking is shown for the full and reduced models. B, Note that both the 93comp branched and 98comp unbranched models provide a very close qualitative match to the full model's spike shape, while the 5comp unbranched and 41comp branched models show mismatches starting with the fast AHP. C, Note the wider time window compared to that in B. The 93comp and 98comp models again provided close qualitative matches to the full model's spike shape, while the 5comp and 41comp models did not. D, The differences in somatic spike shape between the models were due to differences in axial current flow. The large positive axial current flow out of the soma into the dendrites occurred during the somatic spike. The subsequent negative axial current flow denotes the flow of current from the dendrites back into the soma following the spike. E, The 'match' to the full model spontaneous spike shape shown in B was calculated for each model as the RMSE of the voltage traces from 2 ms before to 6 ms after the spike. Smaller RMSEs represented better matches. Spikes were aligned so that they crossed 0 mV at the same time.

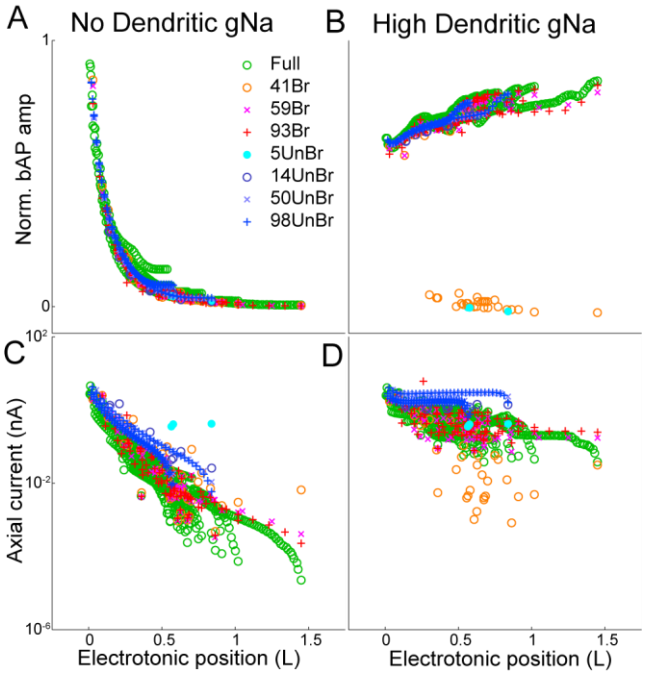

Supplemental Figure 2-2: bAP amplitudes were quite similar between most models with either no or high dendritic gNa density.

All models were driven to fire at 75 Hz +- 0.1% with DC somatic injection. Under these conditions, all models were plotted together in the same panels because different models exhibited quite similar bAP amplitudes. A, The bAP amplitude in each compartment of each model was plotted against that compartment's electrotonic distance from the soma. With no dendritic gNa, bAP amplitude decayed with electrotonic distance at about the same rate in all the models. B, With high dendritic gNa, bAP amplitude slightly increased with electrotonic distance at about the same rate in all models. However, the bAP amplitude decayed sharply in the 5comp and 41comp models. C, The log of the maximum amount of axial current flowing into each compartment during a spike (referred to simply as axial current) was plotted against electrotonic distance from the soma. With no dendritic gNa, the axial current decayed with electrotonic distance at approximately the same rate in each model. D, With high dendritic gNa, axial currents decayed with electrotonic distance quite slowly due to successfully back propagating spikes in most of the models.

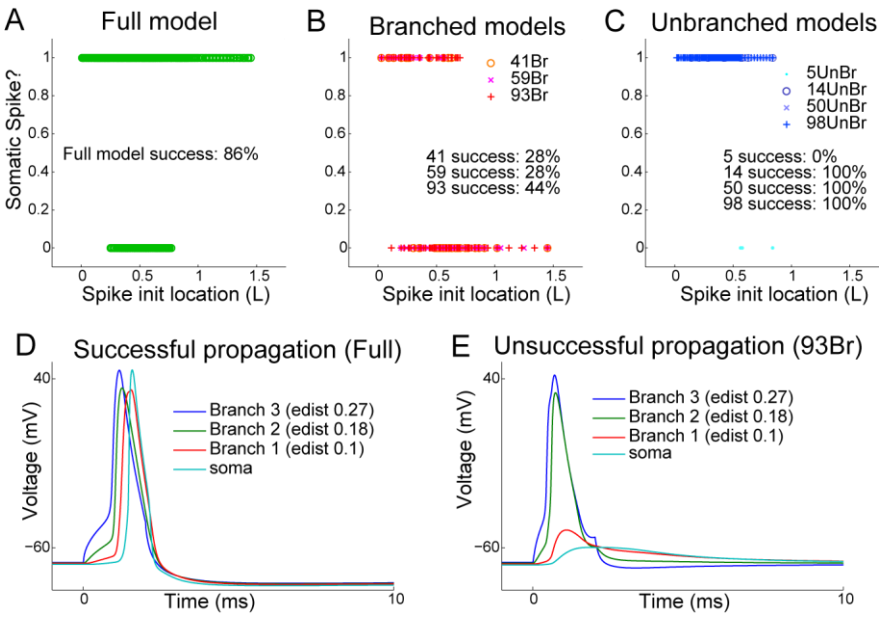

Supplemental Figure 2-3: In the models with high dendritic gNa, dendritically initiated spikes propagated to cause somatic spikes with success rates that varied by model type.

To assess dendritic spike propagation to the soma, each model was prevented from firing spontaneously with -41 pA somatic DC injection. Dendritic spikes were initiated with brief (2 ms) but powerful (400 pA) current injections in each dendritic compartment of each model. Dendritically initiated spikes were considered to have successfully propagated to the soma if they caused the soma to spike. A, Dendritically initiated spikes propagated to the soma successfully from most (86.5%) dendritic initiation sites in the full model. B, In contrast to the full model, dendritically initiated spikes rarely propagated to the soma successfully in the branched reduced models. The branched reduced model with the highest success rate (93comp, 44.0%) had only about half the success rate of the full model. C, Also in contrast to the full model, dendritically initiated spikes always propagated to the soma in the divided unbranched reduced models, while they never did in the 5comp model. D-E, A comparison of dendritic spike propagation showed that the full model allowed dendritic spikes to propagate to the soma while the 93comp branched model did not, despite identical spike initiation locations in 'Branch 3'.

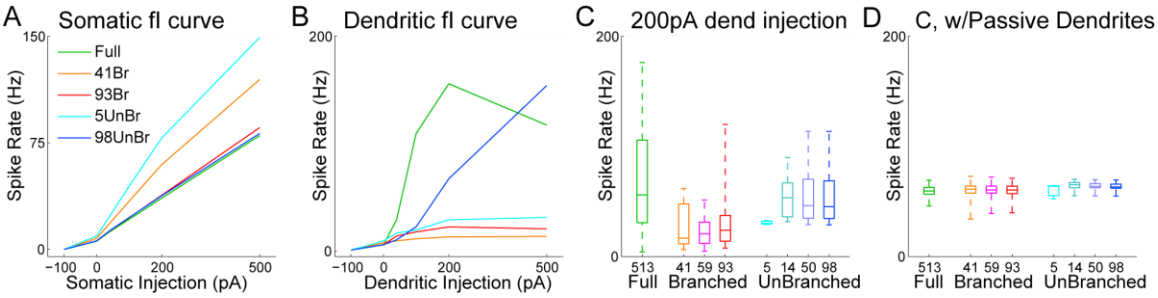

Supplemental Figure 2-4: Models with high dendritic gNa that allowed dendritic spike initiation still exhibited close matches to the full model's somatic fI curves but did not exhibit close dendritic fI curve matches.

DC injection amplitudes ranged from -100pA to +500pA to explore the full physiological range of model spike frequencies. A, The somatic fI curves plotted here were quite similar to those with medium dendritic gNa (Fig. 2.6A). B, The spike frequency of each model was plotted for each level of DC injection in the same dendritic compartments featured in Fig. 2.6B. In contrast to the somatic fI curves, the dendritic fI curves with high dendritic gNa were quite different from those with medium gNa (Fig. 2.6B). Note that the full and 98comp models fired many times faster than the 5comp, 41comp or 93comp models at most amplitudes of positive current injection. C, The spike frequency response was plotted for 200 pA DC injections in each compartment of each model. In contrast to the case with medium dendritic gNa (Fig. 2.6C), the branched reduced models exhibited slower median firing rates than the full model. While the unbranched reduced models possessed comparable median firing rates to those of the full model, the full model's wide range of firing rates was not matched by any reduced model. D, Same as C, but with all dendritic channels removed. Data are identical to those shown in Fig. 2.6D, but are reproduced here for easier comparison. Note the close match between the responses of all the models.

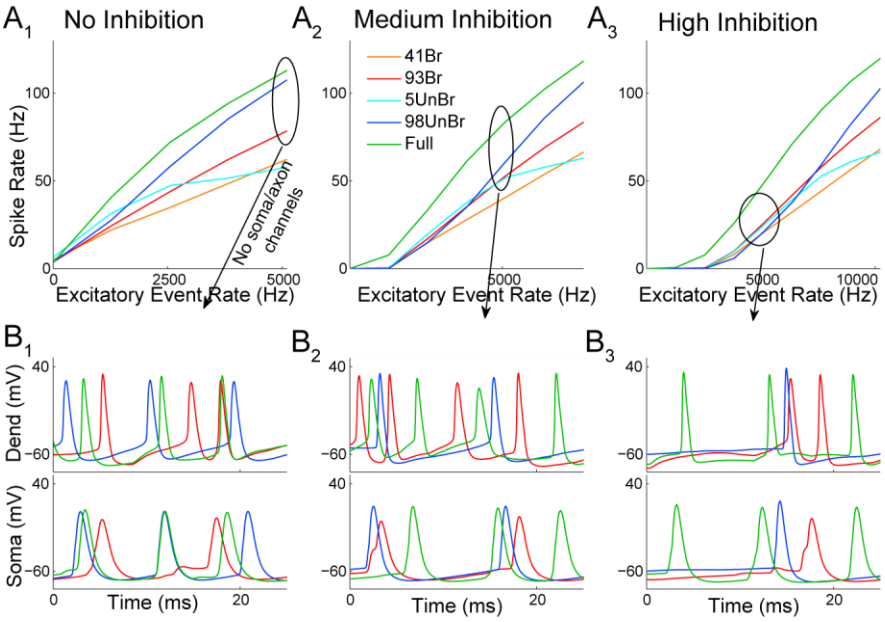

Supplemental Figure 2-5: The full model's fF curves with high dendritic gNa could not be matched by any reduced model.

This figure is similar to Fig. 2.8 except that the density of dendritic sodium conductance was increased to 800 S/m2 to allow dendritic spike initiation. A1-3, In contrast to the case with medium dendritic gNa, the full model had steeper fF curves than any reduced model at every combination of inhibition and excitation tested. B1-3, Somatic and axonal conductances were removed to prevent somatic spike generation. The steeper fF curves of the full model were due to its high ability to generate dendritic spikes given its large dendritic voltage fluctuations in response to synaptic input (e.g. Fig. 2.8C) coupled with its high ability to propagate dendritic spikes to the soma (e.g. Supplemental Fig. 2-3). Note that most of the spikes observed in the example dendritic location propagated to the full model's soma, while many fewer dendritic spikes propagated to the soma in the 93comp branched model (see Supplemental Fig. 2-3). Further note that, in general, fewer dendritic spikes were initiated in the dendrites of the 98comp model due to lower dendritic voltage fluctuations (e.g. Fig. 2.8C).

2.6.2. Supplemental Tables

Supplemental Table 2-1: Voltage-dependent gates.

Steady-state equation for all voltage-dependent gates:

$$X_{inf}(V_m) = Min_{inf} + [(1 - Min_{inf}) / (1 + \exp ((V_{0.5inf} - V_m) / K_{inf})]$$

Standard kinetic equation:

$$\tau(V_m) = \tau_{min} + [(\tau_{max} - \tau_{min}) / (\exp ((V_{0.5\tau} - V_m) / K_{\tau 1}) + \exp ((V_{0.5\tau} - V_m) / K_{\tau 2}))]$$

Kinetics for Na_P slow inactivation (s) gate:

$$\alpha(V_m) = [(A_\alpha * V_m) + B_\alpha] / [1 - \exp ((V_m + (B_\alpha / A_\alpha)) / K_\alpha)]$$

$$\beta(V_m) = [(A_\beta * V_m) + B_\beta] / [1 - \exp ((V_m + (B_\beta / A_\beta)) / K_\beta)]$$

$$\tau(V_m) = 1 / (\alpha(V_m) + \beta(V_m))$$

For a more detailed description of the voltage dependent gates used in this study, see Gunay et al 2008.

Channel	Gate	Pwr	Min_{inf}	$V_{0.5inf}$ mV	K_{inf} mV	τ_{min} ms	τ_{max} ms	$V_{0.5\tau}$ mV	$K_{\tau 1}$ mV	$K_{\tau 2}$ mV
Na_F	m	3	0	-39	5	0.028	0.028	NA	NA	NA
Na_F	h	1	0	-48	-2.8	0.25	4	-43	10	-5
Na_F	s	1	0.15	-40	-5.4	10	1000	-40	18.3	-10
Na_P	m	3	0	-57.7	5.7	0.03	0.146	-42.6	14.4	-14.4
Na_P	h	1	0.154	-57	-4	10	17	-34	26	-31.9
Na_P	s	1	0	-10	-4.9					
K_V2	m	4	0	-33.2	9.1	0.1	30	-33.2	21.7	-13.9
K_V2	h	1	0.2	-20	-10	3400	3400	NA	NA	NA
K_V3	m	4	0	-26	7.8	0.1	14	-26	13	-12
K_V3	h	1	0.6	-20	-10	7	33	0	10	-10
K_V4_{fast}	m	4	0	-49	12.5	0.25	7	-49	29	-29
K_V4_{fast}	h	1	0	-83	-10	7	21	-83	10	-10
K_V4_{slow}	m	4	0	-49	12.5	0.25	7	-49	29	-29
K_V4_{slow}	h	1	0	-83	-10	50	121	-83	10	-10
KCNQ	m	4	0	-61	19.5	6.7	100	-61	35	-25
Ca_{HVA}	m	1	0	-20	7	0.2	0.2	-20	NA	NA
HCN_{fast}	m	1	0	-76.4	-3.3	0	3625	-76.4	6.56	-7.48
HCN_{slow}	m	1	0	-87.5	-4	0	6300	-87.5	8.9	-8.2

Channel	A_α mV^{-1} ms^{-1}	B_α ms^{-1}	K_α mV	A_β mV^{-1} ms^{-1}	B_β ms^{-1}	K_β mV
Na_P	-2.88×10^{-6}	-4.9×10^{-5}	4.63	6.94×10^{-6}	4.47×10^{-4}	-2.63

Supplemental Table 2-2: Calcium-dependent gate.

SK channel calcium dependence (n = the Hill Coefficient):

$X_{inf}([Ca^{2+}]) = [Ca^{2+}]^n / ([Ca^{2+}]^n + (EC_{50})^n)$

SK channel kinetics:

--for $[Ca^{2+}] < [Ca^{2+}]_{Sat}$, $\tau([Ca^{2+}]) = \tau_{max} - ([Ca^{2+}] * [(\tau_{max} - \tau_{min}) / K_{\tau\text{-}Ca}])$

--for $[Ca^{2+}] > = [Ca^{2+}]_{Sat}$, $\tau([Ca^{2+}]) = \tau_{min}$

Channel	Gate	Pwr	$[Ca^{2+}]_{Sat}$ (µM)	EC_{50} (µM)	$K_{\tau\text{-}Ca}$ (ms/µM)	Hill Coeff
SK_{Ca}	m	1	5	0.35	14.4	4.6

Supplemental Table 2-3: Model conductance density parameter sets used in this study.

The tuned parameter set was used in most figures. 'RandSet1' and 'RandSet2' were two of the randomly generated parameter sets used in Fig. 2.10. RandSet1 and RandSet2 were chosen to demonstrate mapping of reduced model parameter sets back to the full model because they respectively produced the fastest and slowest spiking with 500pA somatic current injection.

Conductance	Tuned Densities (S/m2)	RandSet1 (fast)	RandSet2 (slow)
NaF soma	2500	9955	2953
NaP soma	1	3.863	1.672
Kv2 soma	320	121.3	439.6
Kv3 soma	640	2281	277.1
Kv4fast soma (Kv4slow = 1.5*Kv4fast)	160	174.1	242.5
KCNQ soma	0.4	0.123	0.268
SK soma	50	29.68	56.16
CaHVA soma	2	5.982	5.132
HCNfast soma (HCNslow = 2.5*HCNfast)	0.2	0.506	0.144
NaF dend	0 / **40** / 800	10.07	18.66
NaP dend	0 / **1**	1.475	1.629
Kv2 dend	64	148.3	25.89
Kv3 dend	128	63.15	196.8
Kv4fast dend (Kv4slow = 1.5*Kv4fast)	160	47.79	186.3
KCNQ dend	0.4	0.207	0.43
SK dend	4	1.330	5.848
CaHVA dend	0.15	0.143	0.079
HCN dend	0.2	0.160	0.071
NaF axon	5000	3597	2990
NaP axon	40	116.9	10.76
Kv2 axon	640	513.5	1250
Kv3 axon	1280	703.0	2485
Kv4fast axon (Kv4slow = 1.5*Kv4fast)	1600	457.2	3761

KCNQ axon	0.4	0.184	0.104

CHAPTER 3: AIM 2 – THE USE OF AUTOMATED PARAMETER SEARCHES TO IMPROVE ION CHANNEL KINETICS FOR NEURAL MODELING

3.1. Abstract

The intrinsic electrical properties of neurons depend on the behavior of their ion channels. The voltage and time dependence of ion channels can be regulated in many ways, notably phosphorylation, interaction with phospholipids, and binding to auxiliary subunits. However, obtaining a quality match between recorded voltage traces and the output of conductance based compartmental neuron models depends on accurate estimates of the kinetic parameters of the channels in the biological neuron. Many parameter variation studies have set conductance densities free while leaving kinetic channel properties fixed as the experimental constraints on the latter are usually better than on the former. Because individual cells can tightly regulate their ion channel properties, we suggest that channel property parameters may be profitably set free after density searches in order to both improve matches to data and learn about variability in kinetic parameters between cells. To this end, we analyzed the parameter optimization of reduced models of three electrophysiologically characterized and morphologically reconstructed GP neuron models. We performed two automated searches with different types of free parameters. First, conductance density parameters were set free; even the best matches exhibited unavoidable problems which were due to limitations in our channel models. We next set channel kinetics free which improved the unavoidable mismatches. Additionally, some kinetic parameters converged onto new values in

multiple cells, suggesting the possibility for tailored improvements to channel models. Overall, we suggest that experimental channel property data should not be considered a gold standard for modelers, particularly when the channels were characterized under different experimental conditions than recorded data to be matched by a model.

3.2. Introduction

Neurons possess complex intrinsic electrical properties which depend on the precise kinetics of diverse populations of membrane bound voltage dependent ion channels. The voltage and time dependence of ion channels can be regulated in many ways. The most common regulation mechanism is probably given by the phosphorylation state of ion channels. Indeed, the kinetics of many channels can be modulated by (de)phosphorylation at multiple cytoplasmic sites (Rossie, 1999; Park et al., 2008) by, for instance, protein kinase C or calcineurin. Both enzymes are regulated by Ca^{2+}, which allows coupling to neuromodulation or cellular activity (Newton, 1995; Rusnak and Mertz, 2000). For example, calcineurin mediated dephosphorylation of the constitutively phosphorylated Kv2.1 channel causes a hyperpolarizing shift in its activation curve and a decrease in its activation time constant which both serve to increase activation (Park et al., 2006). Similarly, the protein kinase C (or protein kinase A) mediated phosphorylation of Kv4.2 channels causes a depolarizing shift in the voltage-dependent activation curve which decreases activation (Hoffman and Johnston, 1998). In addition to (de)phosphorylation, channel activity can be regulated by diffusible or membrane bound factors. For instance, recovery from inactivation of Nav1.6 channels is slowed by interaction with fibroblast growth factor homologous factor 2A (Rush et al.,

2006). Unfortunately, understanding the functional implications of channel regulations like these in the intact neuron is extremely difficult due to the relative lack of experimental tools to simultaneously determine the status of multiple regulation mechanisms.

Using conductance based compartmental neuron models, it may be possible to detect multiple subtle modulations like those described above by varying channel property parameters while comparing model output to electrophysiological recordings. Both database and automated search methodologies have been used to explore the parameter space of neuron models (Prinz et al., 2003; Keren et al., 2005; Van Geit et al., 2008). Due to the high dimensionality of a neuron model's parameter space, researchers often vary conductance density parameters while leaving channel kinetics fixed, which has been a successful method for matching many recorded features (Prinz et al., 2003; Druckmann et al., 2008; Gunay et al., 2008). To extend this work, we set out to examine whether free channel kinetics can be constrained by automated searches and how much improvement is possible over density searches.

We present an analysis of the optimization of three neuron models to match electrophysiological data recorded for each neuron. Our sample of neurons was recorded in rat brain slices from the GP, but the methods we develop in this study are not in any way customized to the analysis of GP neurons. In order to distinguish the capabilities of free density and kinetic parameters, we performed two stages of automated parameter searches using a modified particle swarm evolutionary algorithm (Clerc and Kennedy, 2002) to match model output to recorded traces. For the first stage, conductance densities were set free; the best matches of this stage exhibited unavoidable mismatches which we

can attribute to fundamental limitations in our channel models through careful analysis. To correct these limitations, the second stage of searches set either all channel property parameters free or a small group which were selected based on an 'error sensitivity analysis'. The second stage searches improved the match for every neuron, including some of the unavoidable mismatches identified in the first stage by optimizing channel properties. Indeed, some kinetic parameters converged onto new values in different sample neurons in second stage searches with both sets of free parameters (all free or just a selected group), indicating specific improvements to our original channel models. Finally we present evidence that these channel kinetics are independent of morphological model simplifications and improve performance equally well in full morphological compartmental models.

3.3.Methods

3.3.1. Description of morphologies and recordings

We recorded current clamp data and reconstructed the detailed morphologies of three GP neurons as described previously (Hanson et al., 2004). These three neurons were recorded and reconstructed during the preparation of a much larger physiological database of 146 GP neurons (Gunay et al., 2008). The amount of variability in the properties of the three neurons selected for use in this study approximated the amount of variability that we observed in our larger database of GP neurons (Gunay et al., 2008).

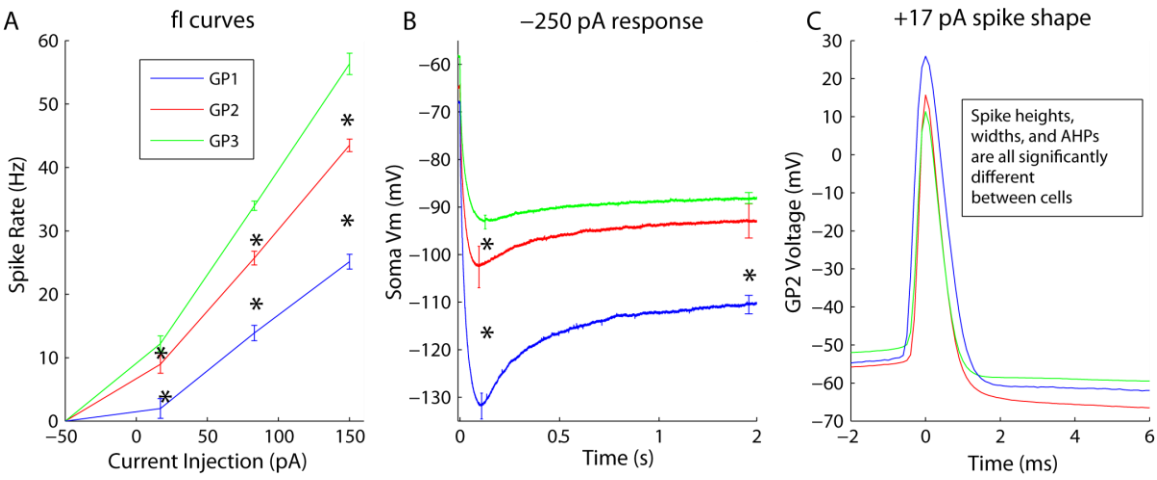

Figure 3.1: Each recorded neuron possessed unique electrophysiological properties.

Neurons were recorded in slice in the presence of synaptic blockers (see Methods). Stars denote statistically significant differences. A, The spike frequency versus somatic current injection (fI) curves are shown for all three cells. Each current injection level was repeated five times, so each point is the mean ± standard deviation (error bars) for those five repetitions. Each spike rate at each positive current injection level was significantly different for all cells ($p < 0.05$, Student's t-test). B, Average responses to -250 pA of somatic injection are shown. The minimum voltage reached was significantly different for each cell relative to the other two ($p < 0.05$, Student's t-test); additionally, the steady state voltage reached was significantly lower for GP1 than for GP2 or GP3 ($p < 0.05$, Student's t-test). C, The average spike shape during +17 pA injection is plotted. All 'steady state' spikes were collected from 0.5 s to 1.5 s following onset of injection. Spikes were aligned by their spike time, which was estimated as the midpoint between the times that a spike was 5 mV below its peak on the rising and falling phases. Spike widths, peak voltages, and AHP depths (recorded at +5 ms relative to the spike) were all significantly different between each cell and the other two ($p < 0.05$, Student's t-test for spike widths, Mann-whitney U test for peak voltages and AHP depths).

Briefly, morphologies were obtained using Neurolucida (MicroBrightField, Inc) from biocytin filled rat GP neurons in slice. Current clamp data were recorded in the presence of the synaptic blockers AP-5 (100 µM), CNQX (10 µM) and Picrotoxin (40 µM). The responses of each neuron to -250 pA (n250), +17 pA (p17), and +150 pA (p150) were recorded. The p17 recording was taken because it allowed us to capture spike shapes from spontaneously silent neurons at a spike rate close to the spontaneous activity of GP neurons. Spike shapes varied between the p17 and p150 injection conditions such that p150 spikes tended to be shorter and wider. In the three neurons

pursued for modeling one was spontaneously silent while the others showed pacemaking activity. The recordings were corrected both for a 9 mV liquid junction potential error and for series resistance error. The three neurons exhibited different input resistances (Fig. 3.1*B*), firing rates during current injection (Fig. 3.1*A*), and spike shapes (Fig. 3.1*C*). The three neurons also exhibited a different amount of sag in response to -250pA injection as well as different spike height and frequency accommodation in response to positive current injection. Further, their morphology showed differences in soma diameter, total surface area, dendritic electrotonic extent, and dendritic branching structure (Fig. 3.2*A*).

3.3.2. Construction of Full and Reduced Models

Using Neurolucida reconstruction files, we created three full GP model morphologies for use in the GENESIS (version 2.3) neural simulator (http://www.genesis-sim.org) (Fig. 3.2*A*). In addition to the soma and dendrites, a single compartment axon (length = 40um and diameter = 2.25um) was added to each model morphology so that each model could possess a spike generation site separate from the soma to allow for an axonal contribution to the determination of action potential shape (McCormick et al., 2007). Specific axial resistance (Ra) was set to 1.0 ohm-m which is a value that agrees with studies in neocortical pyramidal neurons (Stuart and Spruston, 1998) and cerebellar Purkinje cells (Roth and Hausser, 2001). Specific membrane capacitance (Cm) was set to 0.01 F/m^2 based on several studies which have found values very similar to this in multiple neuronal cell types (Gentet et al., 2000; Oltedal et al.,

2009). Specific membrane resistance (Rm) was left as a free parameter, because leak channel density can not be expected to be uniform among neurons.

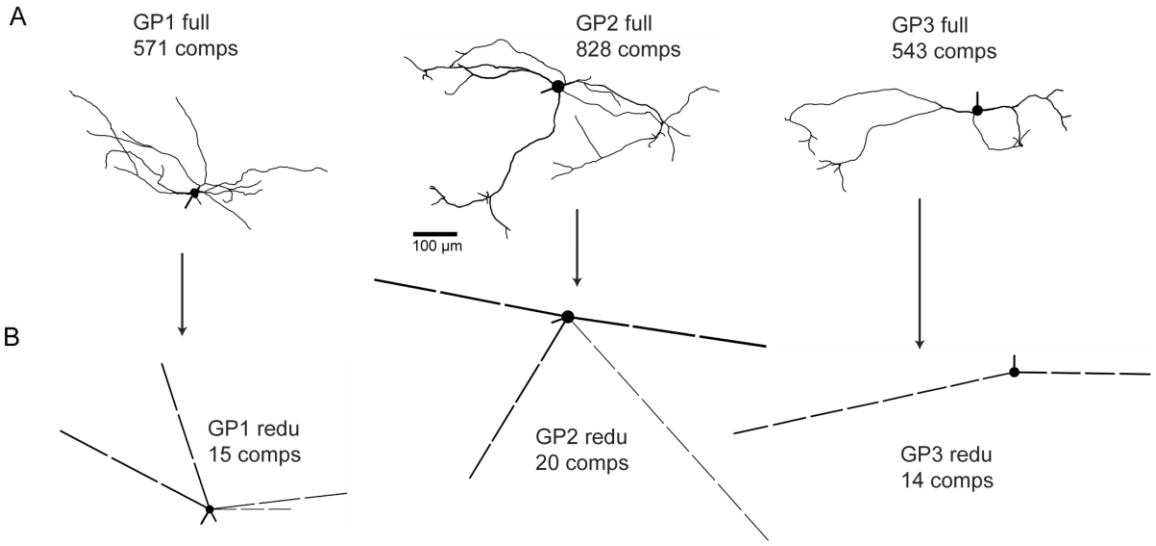

Figure 3.2: Model morphologies.

To aid visualization, all diameters are multiplied by 2. Each column contains a full model above and a reduced model derived from it directly below. See methods and Chapter 2 for details on morphological reduction. All models include a soma and an axon compartment, which are unchanged between a full model and its corresponding reduced model. A, The full GP1, GP2 and GP3 model morphologies. B, The GP1, GP2 and GP3 reduced model morphologies. Each reduced model contained about 40 times fewer compartments than its corresponding full model.

We have recently shown that the morphology of a full model can be greatly reduced if the dynamics of interest of not heavily dependent on dendritic processing of local inputs (Chapter 2). Because the full models possessed from 543 to 828 compartments (Fig. 3.2*A*), running the millions of simulations required for parameter searching would be extremely computationally intensive. Therefore, the morphological complexity of each full model was reduced such that each major branch was collapsed into a single compartment possessing the same total surface area and average tip to tip electrotonic length (Fig. 3.2*B*). Each dendritic compartment was then divided evenly so

that no compartment's electrotonic length exceeded 0.2 L (see Chapter 2 for a detailed explanation and justification of this type of morphological reduction process). The reduced models did not preserve full model detailed branching structure, but detailed branching does not need to be preserved unless dendritic voltage fluctuations must be matched (Chapter 2). The reduced models each possessed about $1/40^{th}$ the number of compartments of their corresponding full models (between 14 and 20 compartments), and were possible to simulate at close to real-time on our machines (Emory EHPCC Linux cluster, http://it.emory.edu/showdoc.cfm?docid=8869).

Each compartment was endowed with voltage and calcium dependent conductances. The conductances that we included were the same as for Chapter 2: NaF, NaP, Kv2, Kv3, $Kv4_{fast}$ and $Kv4_{slow}$, KCNQ, SK, Ca_{HVA}, and HCN_1 and HCN_2 (see Supplemental Tables 3-1 and 3-2 for channel kinetics). The steady-state activation and inactivation curves for all voltage-dependent gates were determined by three parameters: Min_{inf}, the minimum value of activation or inactivation; $V_{0.5inf}$, the voltage at which the gate was 50% activated or inactivated; and, K_{inf}, the slope of the transition from minimal to maximal activation or inactivation. This steady state equation was sigmoidal in form and was consistent with the standard Hodgkin Huxley mathematical formalism:

$$X_{inf}(V_m) = Min_{inf} + [(1 - Min_{inf}) / (1 + \exp ((V_{0.5inf} - V_m) / K_{inf})] \quad (1)$$

The kinetic equation for most voltage-dependent gates (see Supplemental Table 3-1 for NaP, which was unique) was described by five parameters: τ_{max} and τ_{min}, respectively the maximal and minimal values of the time constant; $V_{\tau max}$, the voltage at which the time

constant was maximal; and, $K_{\tau 1}$ and $K_{\tau 2}$, respectively the slope of the time constant curve in the hyperpolarized and depolarized regimes.

$$\tau (V_m) = \tau_{min} + [(\tau_{max} - \tau_{min}) / (\exp ((V_{\tau max} - V_m) / K_{\tau 1}) + \exp ((V_m - V_{\tau max}) / K_{\tau 2}))] \quad (2)$$

For more details including the original parameter values and the equation for the calcium dependent gate of the SK conductance, see Supplemental Tables 3-1 and 3-2.

Our lab previously explored the parameter space of these conductances in GP neuron models using a brute force database approach (Gunay et al., 2008) and found that a qualitatively satisfactory approximation to experimental data is possible with these conductances, though some mismatches remain.

3.3.3. Classification of Model Output by an 'Error Function'

We developed 30 measures to characterize model output during three different levels of current injection (see supplemental material for a complete list of each error measure). Our measures were based on features recorded in current clamp to avoid space clamp issues (Bar-Yehuda and Korngreen, 2008). Measures included characterizations of spike rate, spike shape, spike pattern, accommodation to positive current injection, and the voltage response during and after negative current injection. Experimental spike shapes at both levels of positive current injection (p17 and p150) were compared to model spike shapes, because p150 spikes tended to be shorter and wider than p17 spikes and potentially contained additional information about the dynamics of the recorded cell. Slow changing features of raw voltage traces, such as the afterhyperpolarization from +2

ms to +10 ms following a spike, were compared by calculating the root mean squared error (RMSE) between the two traces. To allow for the additional capture of slope information, fast changing features of raw voltage traces including spike shapes were compared using a phase plane error measure adapted from a previous study (Keren et al., 2005) (Supplemental Fig. 3-1).

Each measure was assigned an error value. To calculate each error value, the raw (undivided) error between model output and the average physiological response for the cell to be matched was calculated; this raw error was then divided by an 'experimental variability unit', which represented the experimental variability in that cell's responses over five trials. The experimental variability unit for a measure was defined as the average of the raw errors between the measure for each individual trial and the average measure for all five trials (Supplemental Fig. 3-2). For a few error measures in individual neurons, a measurement of experimental variability was not available: for instance, the spike rate following offset of negative current injection for cell GP1 was zero in all five trials. In these cases, we hand-tuned the normalization factor to allow good search performance.

3.3.4. Optimization of Parameters Using Search Algorithms

For automatic searches of parameter space, we used a modified version of the 'particle swarm' algorithm, which is in the class of 'evolutionary algorithms'. Evolutionary algorithms have been used successfully many times in computational neuroscience to optimize the parameters of neuron models (Vanier and Bower, 1999; Davison et al., 2000; Bush et al., 2005; Keren et al., 2005; Gerken et al., 2006; Weaver

and Wearne, 2006). The evolutionary algorithm that we used to optimize the parameters of our reduced models was the particle swarm optimization algorithm. The particle swarm is effective at finding good solutions and not getting trapped in local minima (Clerc and Kennedy, 2002). To make search behavior more predictable, we slightly modified the standard particle swarm algorithm. Each search was run three times in parallel to allow for comparisons between the parameter values found by each run. Each search also included at least two sequential sets of these parallel runs to ensure achievement of optimized results (see supplemental material for a detailed description of our particle swarm search algorithm, including termination criteria).

In addition to our particle swarm, for some control simulations we also used the Conjugate Gradient descent algorithm (CG algorithm) of Vanier and Bower 1999, which can be found in the Genesis 2.3 distribution (http://www.genesis-sim.org/GENESIS/).

For both algorithms, the total combined error for all measures was inverted and defined as the 'fitness'. The goal of each algorithm was to maximize the fitness of parameter sets.

3.3.5. Selection of Free Parameters

A typical compartmental neuron model possesses several hundred parameters that can be varied to produce different model output. Because channel properties like time constants and voltage dependencies are generally more effectively constrained by experiments than are channel densities, channel densities are frequently used as free parameters during automated tuning. Indeed, experiments counting the mRNA number for different channels in identified neurons have demonstrated that significant variability

in channel densities is possible (Schulz et al., 2006). Therefore, it makes sense to set channel densities as free parameters during the automated tuning of neuron models. However, setting channel property values as free parameters during automated tuning may also make sense. Experimental estimates of channel property values possess some degree of uncertainty due to noisy recordings. Furthermore, channel property values may be different between the cell that must be matched and the cells in which they were initially characterized, because channel properties can vary depending on phosphorylation state and other factors.

Our first stage searches were run with conductance density parameters free, and will be referred to as 'density searches' (also abbreviated 'dS' in figures). Separate free conductance density parameters were defined for the soma, axon and dendrites. The soma and the dendrites possessed all 11 conductances while the axon only possessed 7 (NaF, NaP, Kv2, Kv3, $Kv4_{fast/slow}$, and KCNQ). To decrease the number of free parameters, the densities of $Kv4_{fast}$ and $Kv4_{slow}$ were linked with a fixed multiplier because they were the same in every way except for the amplitude of their inactivation time constants. Similarly, the densities of HCN_1 and HCN_2 were linked with a fixed multiplier because the two conductances are very similar to each other (see Supplemental Table 3-1). Therefore, there were 9 somatic, 9 dendritic, and 6 axonal conductance density parameters, which totaled 24 free density parameters. Axonal densities of spike conductances (NaF, NaP, Kv2, Kv3, and Kv4) were forced to maintain a ratio of between 5 and 50 to their corresponding somatic densities. The dendritic density of NaF was forced to remain below 100 S/m^2 to avoid dendritic spike initiation, which decreases the ability to map dynamics between full and reduced models (Chapter 2). In addition to

density parameters, the reversal potential for the leak conductance (Eleak) and Rm were left as free parameters, because neither is well constrained by experiments. Therefore, there were 26 free parameters in the density searches. The initial values for all parameters were the same for all three cells and were based on the values used in Chapter 2 and Gunay et al 2008. Each parameter (densities and Rm) was varied independently between 20% and 500% of its initial value and Eleak was varied from -10 mV to +10 mV relative to its initial value to create the three starting populations of 1000 parameter sets each for the first set of parallel runs. For the second set of parallel runs, the best values found by each of the first set of parallel runs were used as initial values to generate the starting parameter set populations. A third set of parallel runs was performed for two cells to serve as a control case for the second stage kinetic searches.

Second stage searches allowed both density and channel properties to vary as free parameters. Some searches set all channel properties free, while the free parameters for other searches were chosen using an error sensitivity analysis, which will be described in the following section. Densities were only set free in this stage if a property for that channel had been set free; dendritic and axonal conductance densities were set in a fixed proportion to the somatic densities based on the ratios found by the best results of the density searches. The initial values for all kinetic parameters were the same for all three cells and were based on the values used in Chapter 2 and Gunay et al 2008. While most kinetic parameters could be widely varied without greatly decreasing overall fitness, large or small values for some parameters led to large decreases in fitness. We initially varied such parameters narrowly to avoid generating starting populations of parameter sets with very low fitness. To determine which parameters should be varied narrowly, we

measured overall fitness after setting each parameter to a small value (20% for multiplicative parameters like time constants, -10 mV for additive voltage dependencies) and a large value (500% for multiplicative parameters, +10 mV for additive parameters). If the average fitness with the very small and very large values for a parameter was at least 50% of the original fitness value (optimized by the density search) then that parameter was varied widely (20% to 500% for multiplicative parameters, -10 mV to +10 mV for additive parameters). Otherwise, that parameter was varied narrowly (90% to 110% for multiplicative parameters, -1 mV to +1 mV for additive parameters). Narrowly varied parameters were most often those that described steady state (in)activation curves, although some parameters describing time constant curves were also identified as those that should be varied narrowly. As for the first two sets of density searches, 1000 parameter sets were randomly generated to initiate each of two sets of three parallel runs.

3.3.6. Error Sensitivity Analysis

While setting all channel kinetic parameters free simultaneously could provide very close matches to recorded data, interpreting the results of a search with so many free parameters is difficult. Therefore, we performed an error sensitivity analysis to find a limited set of kinetic parameters which were likely to account for a large share of the improvement of second stage searches over first stage searches. To this end, our error sensitivity analysis varied each parameter one by one in order to identify those which were capable of improving individual error measures by at least 1 unit of experimental variability without severely decreasing overall fitness (a 5% decrease was allowed). We allowed a small decrease in overall fitness because very few parameters were capable of

improving any error measures without decreasing fitness somewhat. Scalar parameters like maximal time constants were scaled from ~0.1 to ~10, while additive parameters like half activation voltages were shifted by -27 mV to +27 mV (see supplemental material for the equations used to generate the scalars and shifts along with the actual values used, which included scalars very close to 1 and shifts very close to 0). Because the effect of varying a model parameter can be highly context dependent, we performed this sensitivity analysis using the same conductance density parameter set in all 3 reduced models; we also performed this sensitivity analysis using a different conductance density parameter set (each density was randomly doubled or halved) in one of the reduced models. The relative capabilities of parameters were quite similar between different contexts, so the effects for each parameter were averaged between contexts.

3.3.7. Simulations

Simulations were performed using GENESIS 2.3 (http://www.genesis-sim.org/GENESIS/) on the Emory high-performance computer cluster running RedHat Linux. Simulation data were analyzed in Matlab (The Mathworks, Inc, Natick, MA).

3.3.8. Statistics and Data Analysis

For statistical analyses, data set normality was assessed with the Lilliefors test, which showed that some data sets were not normally distributed. In cases where data were normally distributed, Students t-test was used to test for significant differences in the mean. In the remaining cases where data were not normally distributed, the non-

parametric Mann-Whitney U test was used for statistical comparisons. To correct for multiple simultaneous comparisons, the significance level was decreased from $\alpha = 0.05$ using the Bonferroni correction. All statistical tests were performed in Matlab. Correlations were calculated using the Spearman correlation coefficient because it is tolerant of non-linearity in the data (Myers and Well, 2003). All correlations were significant at $\alpha = 0.05$ due to the very large number of data points.

3.3.9. Data Sharing

Upon publication, all models along with all current injection patterns and a selection of the most relevant parameter sets used in this study will be made available on the ModelDB public database (http://senselab.med.yale.edu/ModelDB/default.asp).

3.4.Results

3.4.1. Optimized conductance densities resulted in close model fits with current clamp traces, but some specific mismatches remained

When modelers attempt to fit simulation output to recorded data, they frequently set conductance densities free while leaving everything else fixed because conductance densities are generally among the least experimentally constrained parameters of a neuron model (Prinz et al., 2003; Bush et al., 2005; Gunay et al., 2008). In keeping with this strategy, before attempting to set kinetic channel properties free to further optimize data fits, we used our particle swarm search algorithm to optimize conductance densities, ELeak and Rm ('density searches'). Searches were conducted for 3 different GP neurons,

and 2 sets with 3 parallel runs each explored between 43,000 and 111,000 parameter combinations per run before termination criteria were met (see Methods). As has been found in previous studies which have optimized conductance densities to match electrophysiological recordings, our searches converged onto parameter settings that improved overall fitness from starting values of about 0.001 to best values near 0.01 after the first set of parallel runs, with decreasing improvements for subsequent sets of parallel runs (Figure 3.6). During the parameter optimization, our particle swarm algorithm explored wide regions of parameter space but used the most simulation time to explore regions with high average fitness (Supplemental Fig. 3-3). However, we did not generally observe parameter value convergence for the best matches. This could have been due either to the presence of multiple free density settings in different parts of the neuron for the same conductance or to complex interactions between conductances (Taylor et al., 2009).

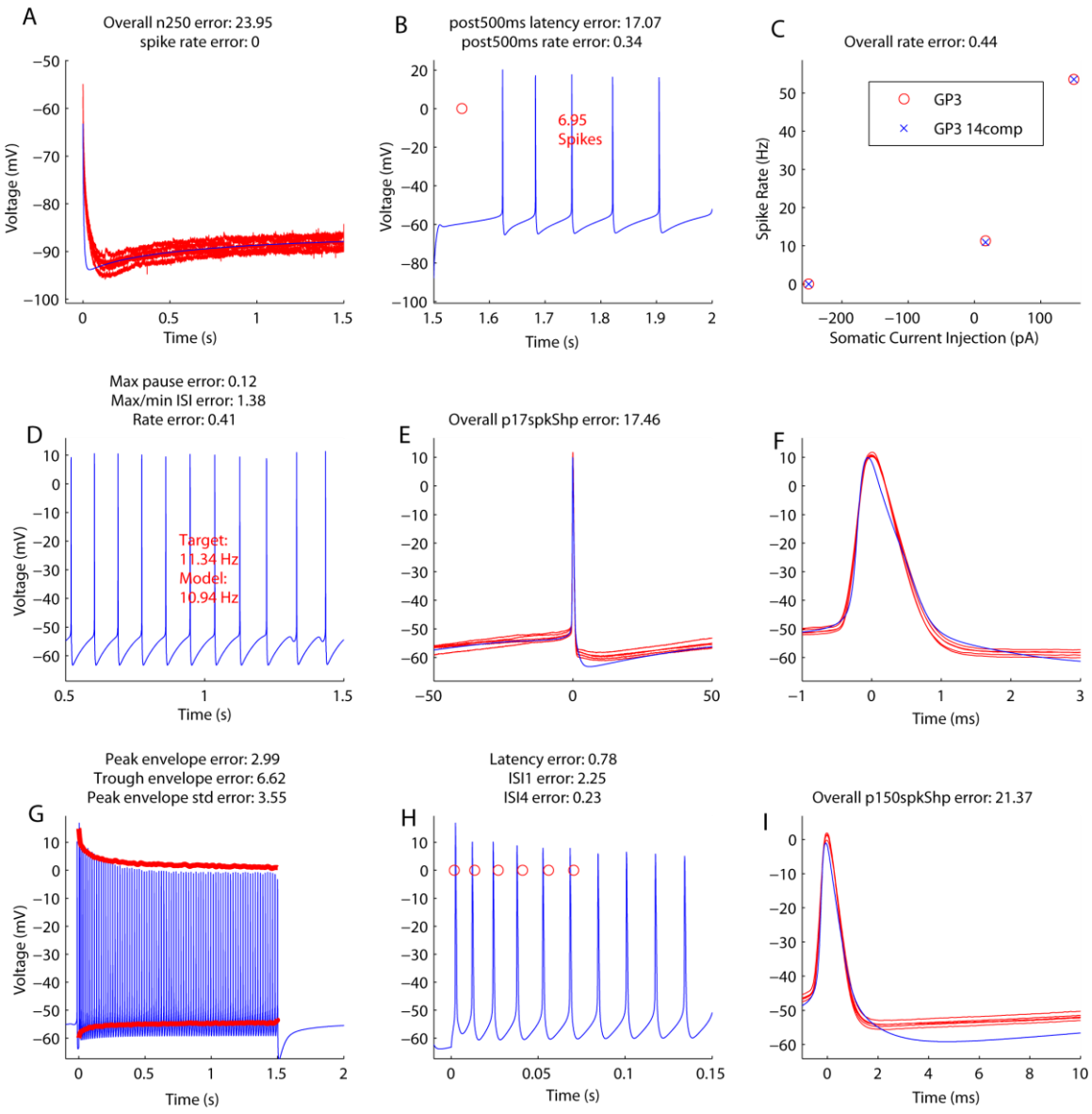

Figure 3.3: A typical example of how optimized conductance densities allowed reduced models to match most features of the electrophysiological recordings.

This figure shows the best parameter set found by the density searches for the GP3 reduced model, with an overall fitness of 0.0106 (total combined error = 94.43). A, The response to -250 pA injection (n250) is shown. The reduced model matched the steady state voltage and sag of the recordings but failed to match the time course of hyperpolarization in the first 50 ms. B, The average spike latency of the recordings following n250 offset is shown as a red circle with error bars showing the standard deviation. The reduced model fired much later than did the actual cell. C, fI curve. The reduced model matched the recorded fI curve. D, Tonic spiking with +17 pA injection (p17). The reduced model exhibited regular interspike intervals (ISIs) without pauses, as did the recordings. E, p17 spike shape. The reduced model matched the p17 spike shape of the recordings with the exception of the first 10-20 ms of the AHP. F, Close up view of the p17 spike shape. G, Accommodation to +150 pA injection (p150). The average curves of the best fits to the spike peaks and troughs of the recordings are plotted in red. The peaks and troughs of the reduced model were hyperpolarized relative to those of the recordings. H, The first 15 ms of the p150 trace. The average spike times of the first six spikes in the recordings are shown as red circles. The reduced model

matched the latency of the first spike, the first ISI and the fourth ISI well. I, p150 spike shape. The reduced model matched the recorded p150 spike shape from -1 ms to +2 ms but exhibited a hyperpolarized AHP from +2 ms to +10 ms.

Analyzing the optimization of three neuron models in parallel allowed us to discover whether certain features of our recordings were consistently difficult to match, or whether difficulties were limited to just one cell. We found that the quality of the matches varied between cells and that some characteristics which could be well matched for one cell were difficult to match for another cell. In terms of overall fitness, the match of the reduced GP3 model using the best parameter set found in the second set of density searches was typical (Fig. 3.3). For this example GP3 parameter set, most of the voltage response to negative current injection was matched, with the exception of the first ~50 ms (Fig. 3.3*A*). The latency to first spike after offset of negative current injection was not closely matched (Fig. 3.3*B*, red dot denotes mean experimental spike latency), but the model's spike rate following offset of negative current injection was close to the experimental mean (Fig. 3.3*B*, 'rate error'). Additionally, the experimental fI curve was well matched by the model (Fig. 3.3*C*). Other well matched experimental features include the long time scale portions of the p17 spike shape (Fig. 3.3*E*), most of the p17 and p150 spike shapes within ~1 ms of the spike peak (Fig. 3.3*F,I*), the spike peak voltages during p150 injection (Fig. 3.3*G*), and the spike pattern during the onset of p150 injection (Fig. 3.3*H*). In contrast, the AHP from about +2 ms to about +10 ms for spikes at both levels of positive current injection was not closely matched to experimental responses (Fig. 3.3*E,G,I*). Overall, most features of the electrophysiological recordings were qualitatively well matched, but there were some obvious remaining mismatches

which varied by cell and which we summarize here. For GP1, which obtained the least overall fitness of the three cells, the best density matches for all three parallel runs exhibited too little sag with negative current injection, fired too fast with p150 injection, and exhibited spikes with peaks that were too short, widths that were too narrow and afterhyperpolarizations (AHPs) that were too deep at both levels of positive current injection (Supplemental Fig. 3-4). For GP2, the only notable problem for the best density matches of all three parallel runs was that p150 spikes (and to some extent p17 spikes) were narrower than the recorded spikes, particularly near the spike peak (Supplemental Fig. 3-5, which also shows a mismatch in spike peak voltages with p150 injection (panel G) that was not consistent for all GP2 density search results). For GP3, which was almost as well matched as GP2, a remarkably consistent problem observed in all of the 2109 density matches with $\geq$ 95% of the best fitness was that the AHP was too deep at both levels of positive current injection (e.g. Fig. 3.3*E,I*). The consistent appearance of deep AHPs across multiple random runs of the GP3 density searches presented an attractive opportunity to try to understand the root causes of the mismatch mechanistically, which we will do in the next section.

3.4.2. An unavoidable mismatch in the spike AHP was due to limitations in the available potassium channels

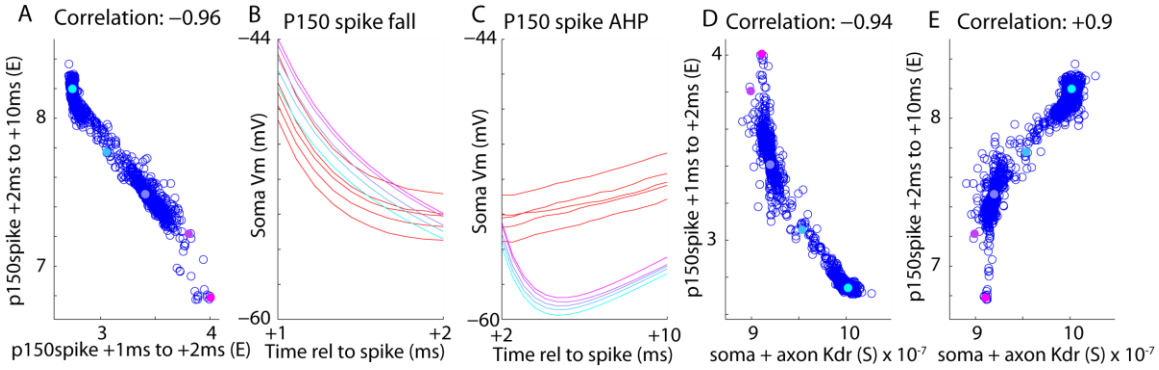

Figure 3.4: An unavoidable mismatch in the spike AHP was due to limitations in the available potassium channels.

For scatter plots, values are shown for all GP3 density parameter sets with fitness at least 95% that of the best GP3 density parameter set; there were 2109 such sets. A, The error ('E') for the p150 AHP was negatively correlated with the error for the p150 falling phase (r = -0.96, Spearman correlation). B, The p150 falling phase. The falling phase is shown for five different parameter sets presenting the range of observed behaviors (a color progression of blue to magenta circles in panels A, D and E). The falling phase was steeper in the model than in the recordings. C, The p150 AHP. As for the falling phase, the AHP is only shown for the same five sets. The AHP was deeper in the model than in the recordings. D, The error for the p150 falling phase was negatively correlated (r = -0.94, Spearman correlation) with the combined value of somatic and axonal Kdr (Kv2, Kv3, $Kv4_{fast}$, and $Kv4_{slow}$) conductance (soma + axonal Kdr). E, The error for the p150 AHP was positively correlated with soma + axonal Kdr (r = +0.90, Spearman correlation).

For a neuron model to match recorded electrophysiological data, an automated search limited to free conductance density parameters relies on accurate channel models for success. If channel models are inaccurate, it may be impossible to match recorded data regardless of channel densities. We hypothesized that the failure of the GP3 density search to match the +2 ms to +10 ms AHP with p150 injection ('p150 AHP') could be due to inaccurate channel descriptions (see Fig. 3.3*I* for a depiction of this mismatch). This mismatch was present in every density match for GP3 with 95% of the fitness of the best set from the whole search including all three parallel runs (N = 2109, Fig. 3.4*A*,*C*; see Supplemental Fig. 3-6*A*, which represents all parameter sets with at least 95% of the

fitness of the best set in just their run). Interestingly, we found a strong negative correlation between the error of the p150 spike shape from +1 ms to +2 ms ('p150 falling phase') and the p150 AHP ($r = -0.96$ for sets with $\geq 95\%$ of the best fitness, Spearman correlation), suggesting that there was a tradeoff between the two error measures for GP3 matches (Fig. 3.4*A*). This tradeoff arose because the p150 falling phase was generally depolarized relative to the recordings while the p150 AHP was hyperpolarized relative to the recordings (Fig. 3.4*B,C*); therefore, improving the p150 falling phase match required hyperpolarization which led to a deepening hyperpolarization in the immediately following p150 AHP. We hypothesized that the tradeoff between the p150 falling phase and AHP was due to a parameter which simultaneously influenced both error measures but in opposite directions, which would prevent the optimization of both at once. Therefore, we looked for parameters which simultaneously influenced both error measures at once. We found that the combined somatic and axonal Kdr (Kv2 + Kv3 + Kv4) conductance (soma + axonal Kdr) was negatively correlated with the P150 falling phase ($r = -0.94$ for sets with $\geq 95\%$ of the best fitness, Spearman correlation) but positively correlated with the P150 AHP ($r = +0.90$ for sets with $\geq 95\%$ of the best fitness, Spearman correlation). Large values of soma + axonal Kdr were associated with a low error for the P150 falling phase but a high error for the P150 AHP and vice versa (Fig. 3.4*D,E*). Therefore, if soma + axonal Kdr were increased by the search algorithm in order to optimize the P150 falling phase, the error for the P150 AHP would simultaneously increase. When parameter sets were separated into 3 groups, one for each parallel run, these correlations were present in every run (Supplemental Fig. 3-6) suggesting that this result is robust to random starting populations of parameter sets. The

failure of any level of Kdr conductance to optimize both error measures simultaneously suggested a problem with the gating properties of our Kv2, Kv3, and/or Kv4 channel models for cell GP3 and therefore a mismatch that was unavoidable during our density searches with fixed kinetics.

3.4.3. Error sensitivity analyses allowed selection of kinetic parameters that improve specific error measures for inclusion in a kinetic parameter search

To understand which channel property parameters might be able to improve mismatches like the one just highlighted, we performed error sensitivity analyses for the best density matches from each of the three parallel runs for each cell. By varying each parameter individually over a wide range, we determined which parameters could improve any of the 30 error measures by at least 1 unit of experimental variability while maintaining at least 95% of overall fitness for each cell. In addition to the 24 conductance densities, ELeak, and Rm, we varied 111 parameters in this way. These 111 parameters included 4 ion reversal potentials, 44 parameters describing voltage or calcium dependent activation or inactivation curves, and 63 parameters describing voltage or calcium dependent time constant curves. For a complete list of all varied parameters and the underlying equations see Supplemental Tables 3-1 and 3-2.

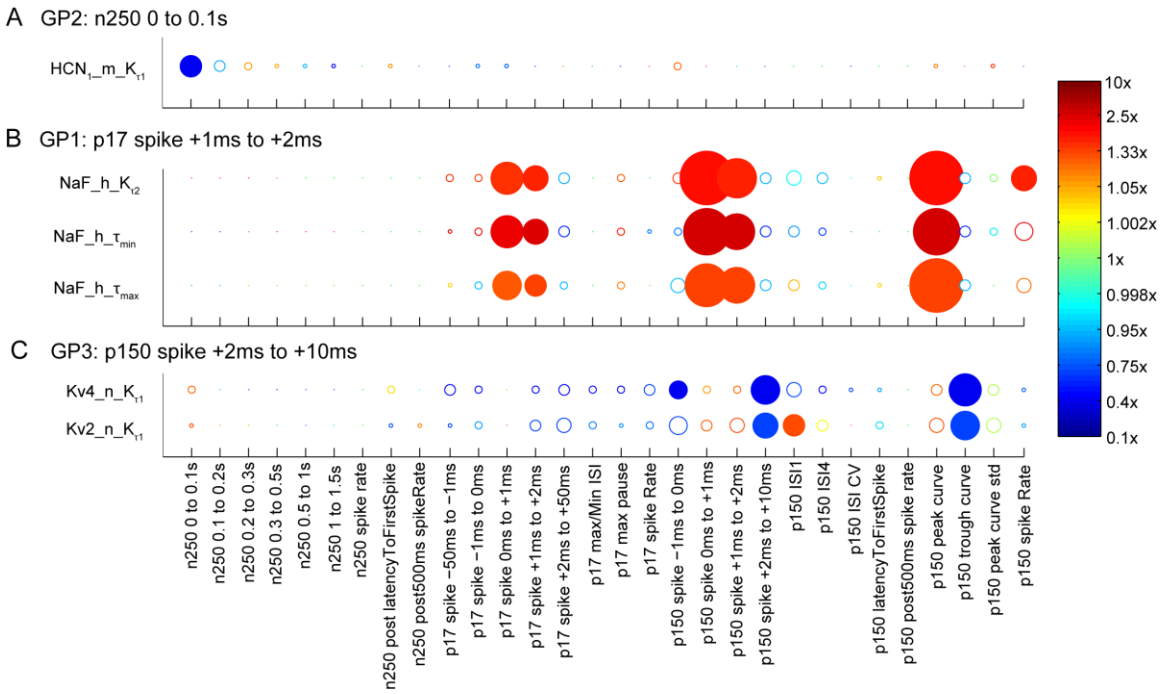

Figure 3.5: Error sensitivity analyses revealed that many kinetic parameters could specifically improve particular error measures.

Each row represents the results of variations of one parameter for a particular cell (see supplemental material for details about the range of variation). Circle area is proportional to the maximal amount that a measure's error could be decreased by any parameter variation while maintaining at least 95% fitness. Each circle is color coded: for example, blue means that a large decrease in a parameter's value yielded the maximal improvement (see color bar). Each panel focuses on a given measure: only parameters which decreased that measure's error by ≥ 1 are shown. Solid and hollow circles represent decreases in a measure's error of ≥ 1 and < 1, respectively. A, Only one parameter, HCN1_m_Kτ1 (which affects the kinetics of HCN1 activation in the hyperpolarized regime), was able to decrease the error of the first 100 ms of the n250 traces by ≥ 1 for the GP2 reduced model. B, Three parameters, all from the h-gate of the NaF conductance, were able to decrease the error of the p17 spike from +1 ms to +2 ms by ≥ 1 for the GP1 reduced model. C, Two parameters from different conductances, Kv4_n_Kτ1 (which affects the kinetics of Kv4 activation in the hyperpolarized regime) and Kv2_n_Kτ1 (which affects the kinetics of Kv2 activation in the hyperpolarized regime), were able to decrease the error of the p150 spike shape from +2 ms to +10 ms for the GP3 reduced model.

We found that a sizable number of parameters met our criteria. In the simplest case, only one parameter met our criteria for a given error measure (e.g. Fig. 3.5*A*) and was therefore selected for our subsequent sensitivity analysis based kinetic searches (sKS). In other cases, multiple parameters met our criteria for a given error measure but had very similar capabilities (e.g. Fig. 3.5*B*); to minimize the number of free sKS

parameters, only the best of these was selected (see Supplemental material for an explanation of this selection process). In general, parameters from the same channel gate had very similar capabilities; however, there were two cases where multiple parameters were chosen from the same channel gate because they provided unique capabilities (NaF fast inactivation (h) gate for the GP2 search and Kv2 fast activation (n) gate for the GP1 search, see Supplemental Table 3-3). Finally, in some cases multiple parameters met our criteria for a given error measure and were all selected because they possessed unique capabilities (Fig. 3.5*C*). When a channel's kinetics were set free, that channel's conductance density was also set free (see Methods) because its previously optimized density value could be incompatible with its newly optimized kinetics. With parameters selected this way, there were fewer free sKS parameters for each cell (10 to 15) than the 26 free density search parameters. To validate our parameter selection method, we also chose a parallel set of 'ineffective' free parameters to run searches with (ineffective kinetic searches, abbreviated 'iKS'). iKS parameters were chosen from the same channel gates as the sKS parameters described above, but they performed the worst on the error sensitivity analysis of all the parameters for that gate. iKS parameters included many important half-activation voltages like that for NaF and Kv4 which may seem like excellent parameters to set free in the absence of an error sensitivity analysis (see Supplemental Table 3-3 for a list of all sKS and iKS parameters, including the associated free conductance densities).

3.4.4. Optimized kinetic parameters improved on results from density searches for the reduced models

Searches which set free either all kinetic parameters (all kinetic searches, abbreviated 'aKS') or just those selected based on our error sensitivity analyses improved upon the results of the density searches (Fig. 3.6*A,B,C*). These improvements were much larger than those seen either with added iterations of density searches or with ineffective kinetic parameters (Fig. 3.6*A,B,C*). To compare the results of density and selected kinetic searches, we show GP3 model output for the best sKS result which used the previously highlighted best density search result for most of its channel densities, Rm and ELeak (compare Fig. 3.3*B,E,G,I* to Fig. 3.7*A,B,C,D*; see Supplemental Fig. 3-8 for the best iKS result). For this cell, fitness improved by about 25% between the density and selected kinetic searches, which was a typical improvement (Fig. 3.6*C*). An important component of this improvement was that the p150 AHP became shallower and approached the experimental p150 AHP (Fig. 3.3*I* vs. Fig. 3.7*D*). Fitness improved even more if all kinetic parameters (120, including the associated free densities) were set free, although about 50% of the improvement over density search results could be achieved by the free parameters selected by the error sensitivity analysis alone (10 to 15, including associated free densities) (Fig. 3.6*C*).

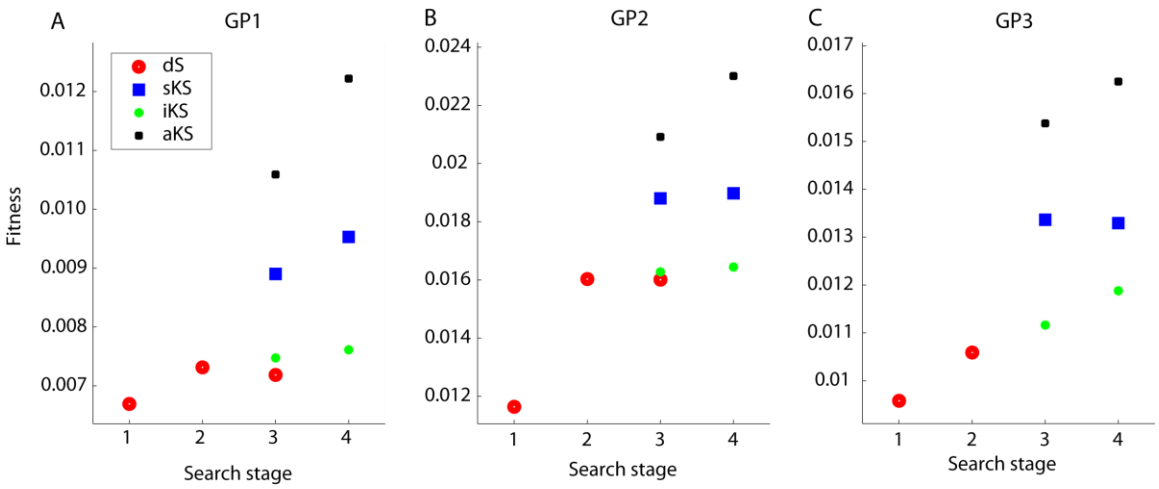

Figure 3.6: Fitness improved with each additional search, particularly with free kinetic parameters. **Three sequential sets (see Methods) of density searches were run for the GP1 and GP2 models. Two sequential sets were run for every other search. The first sets of selected kinetic, ineffective kinetic, and all kinetic searches are plotted as set three because they start with the best results of the second set of the density searches. A, GP1 fitness improved with subsequent searches. The best fitness found by the all kinetic searches was higher than that found by the selected kinetic searches, which was higher than the best fitness found by either the ineffective kinetic or density searches. B, GP2 fitness improved with subsequent searches. This panel is the same as A, but for GP2 instead of GP1. C, GP3 fitness improved with subsequent searches. This panel is the same as A, except that a third stage of the density search was not run due to computational cost.**

After running the kinetic search with selected free parameters, the mismatch in the p150 AHP decreased by 49% for GP3. Notably, the value of Kv4_n_$K_{\tau 1}$ (which affects the slope of the Kv4 activation time constant curve in the hyperpolarized regime) decreased to 15% of its original value for the overall best GP3 sKS result as the error sensitivity analysis predicted it could in order to improve the p150 AHP (see Fig. 3.5*C*). This result is nontrivial because another parameter, Kv2_n_$K_{\tau 1}$ (which affects the slope of the Kv2 activation time constant curve in the hyperpolarized regime), could also have decreased to improve the p150 AHP (see Fig. 3.5*C*); however, it actually increased by 10% in order to optimize the first p150 ISI as the error sensitivity analysis predicted it could (Fig. 3.5*C*). Decreasing Kv4_n_$K_{\tau 1}$ to 15% of its original value decreased

(de)activation time constants in the -60 mV to -50 mV range and decreased the time constant for activation/deactivation of Kv4 at -60 mV from ~3.4 ms to ~0.75 ms for the best sKS result (Fig. 3.8*C*). With faster deactivation time constants at hyperpolarized potentials, the Kv4 conductance could deactivate faster during the falling phase of spikes to allow for shallower AHPs (compare Fig. 3.3*I* to Fig. 3.7*D*). To test whether the shift in Kv4_n_$K_{\tau 1}$ was actually responsible for these shallower AHPs, we set Kv4_n_$K_{\tau 1}$ back to its original value: the fitness decreased to 79% of its optimized value primarily due to a decrease in the match to the p150 AHP (data not shown). It may be argued that Kv4_n_$K_{\tau 1}$ shifted in our searches with selected free parameters because it was compensating for other fixed values in the model. However, we found that even with all kinetic parameters free simultaneously, Kv4 activation time constants in the -60 mV to -50 mV voltage range decreased for all three parallel GP3 runs in order to improve the p150 AHP by accelerating deactivation of Kv4 following a spike (Fig. 3.8*A*-*C*). The consistency of this decrease suggests that the Kv4 activation time constants for this cell did not correctly reflect the kinetics of this channel in our current clamp recordings.

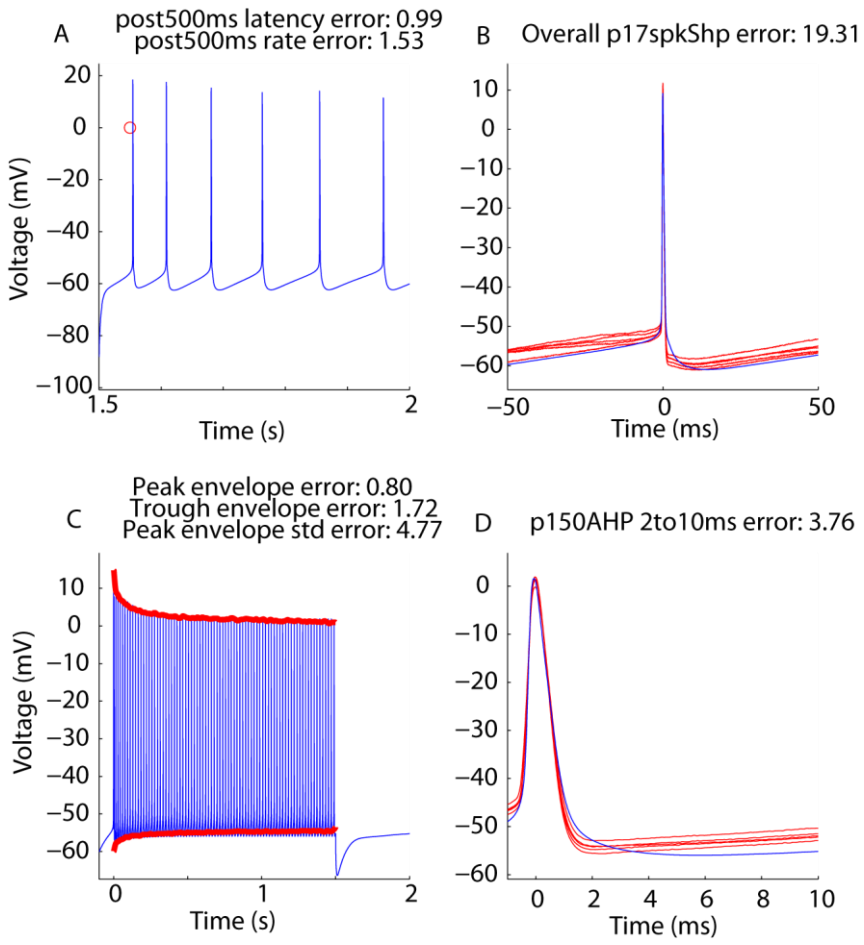

Figure 3.7: A typical example of how optimized channel properties improved the density matches.

This figure shows the best parameter set found by the densities plus properties search for the GP3 reduced model, with an overall fitness of 0.0133 (total combined error = 75.37). Only important differences with Figure 3.3 are shown. A, The reduced model fired at the same latency as the recorded cell following offset of -250 pA injection. B, p17 spike shape. The reduced model matched the p17 spike shape of the recordings, including the first 10-20 ms of the AHP. However, the short latency AHP (+1 ms to +3 ms) of the reduced model was depolarized relative to the recordings. C, Accommodation to +150 pA injection (p150). The peaks and troughs of the reduced model's p150 spikes matched those of the recordings. D, p150 spike shape. The reduced model still exhibited a hyperpolarized AHP relative to the recordings, but the mismatch was much smaller than in Figure 3.3.

After running the selected kinetic searches, we found that the value of NaF_s_τ_{max}, the maximal time constant of slow inactivation kinetics for the fast sodium channel, increased to 200-300% of its original value in both the GP1 and GP2 searches (Fig. 3.9*A*,*B*). To test whether this result depended on the initial range of variation, we ran

kinetic searches for GP2 where the starting range of variation for NaF_s_τ_{max} was from 5% to 125% of the original value (instead of from 20% to 500% of the original value as was done previously). Despite these smaller starting values, the search also shifted NaF_s_τ_{max} to 200-300% of its original value (Fig. 3.9*C*). It may be argued that NaF_s_τ_{max} shifted in our searches because it was compensating for other fixed values in the model. However, we found that the shift in the slow inactivation time constant curve for NaF observed in our kinetic searches with selected free parameters was conserved in all three parallel GP1 and GP2 runs of our kinetic searches with all parameters free (Fig. 3.8F). These shifts allowed the p150 spike peak voltages to more precisely match the experimental data by slowing down the onset of NaF inactivation (Fig. 3.8*D*,*E*). These shifts in the NaF slow inactivation time constant curve, which were conserved across three runs and two cells, suggest that NaF slow inactivation may have been slower in these two cells.

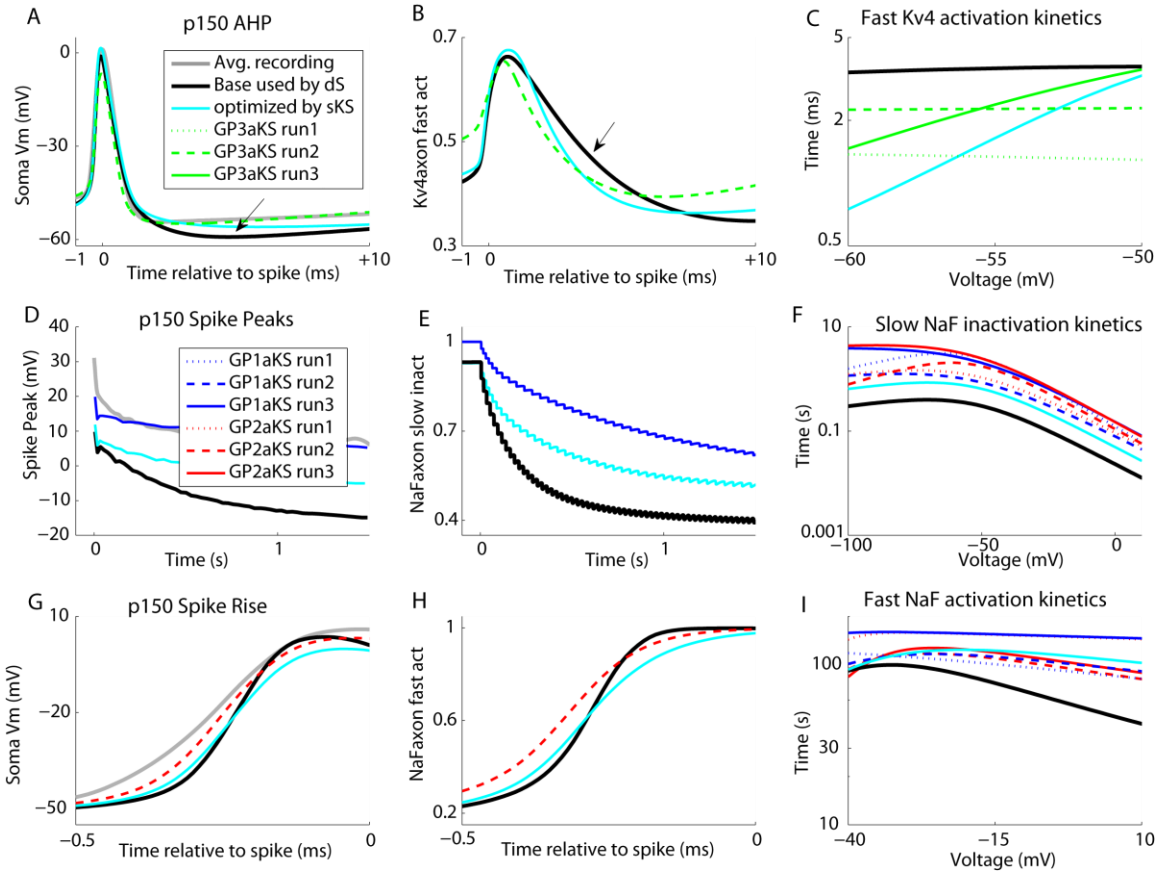

Figure 3.8: Kv4 and NaF gating kinetics shifted in searches with both selected kinetics and all kinetics free.

A, The p150 spike shape matches to the average GP3 recorded spike shape are shown for the best result of one run of the density, selected kinetic and all kinetic searches. The black arrow highlights the major mismatch between the density search result and the recordings during the AHP. B, The average value of the fast activation variable (n) of the axonal Kv4 conductance is shown during the spike cycle for the same search results as in A. The axonal conductance is shown because most of the Kv4 conductance was concentrated in the axon compartment due to our enforced axonal to somatic density ratio. The black arrow highlights the slower deactivation kinetics of the Kv4 conductance for the density search results relative to the kinetic search results. C, In the voltage range which is important for the formation of the AHP by Kv4 (-60 mV to -50 mV), the time constant of activation for Kv4 decreased for the best result of all three parallel runs of the all kinetics search as well as for the best results of the selected kinetics searches (only one is shown for simplicity). D, The p150 spike peak curve matches to the average GP1 recorded spike peak curve are shown for the best result of one run of the density, selected kinetic and all kinetic searches. The best match was exhibited by the all kinetic search result. E, The value of the slow inactivation variable of the axonal NaF conductance is shown for the same search results as in D. Inactivation was fastest using the density search result and slowest using the all kinetic search result. F, The time constant of slow inactivation for NaF increased for the best result of all three parallel runs of the all kinetics search as well as for the best results of the selected kinetics searches (only one is shown for simplicity) for both GP1 and GP2. G, The rising phases of the p150 spike shape matches to the average GP2 recorded rising phase are shown for the best result of one run of the density, selected kinetic and all kinetic searches. The best match was exhibited by the all kinetic search result. Note that the match was calculated using a phase plane error measure rather than a pure voltage comparison. H, The value of the fast activation variable of the axonal NaF conductance is shown for the same search results as in G. The activation value more sharply increased for the density search result than for the kinetic

search results. I, In the voltage range important for spike shape in our models (-40 mV to +10 mV), the time constant of fast activation for NaF increased for the best result of all three parallel runs of the all kinetics search as well as for the best results of the selected kinetics searches (only one is shown for simplicity) for both GP1 and GP2.

We also found a deceleration of NaF activation kinetics in the depolarized regime (-40 mV to +10 mV) that was conserved across all aKS runs for GP1 and GP2 (Fig 3.8I). This deceleration allowed the p150 spike rising phase to become more shallow and therefore more similar to the experimental spike rising phase as calculated by our phase plane error measure (Fig. 3.8*G,H*). This deceleration in NaF activation time constants, consistent between three runs and two cells, suggests that NaF activation may have been slower in these two cells than the original NaF channel model would suggest.

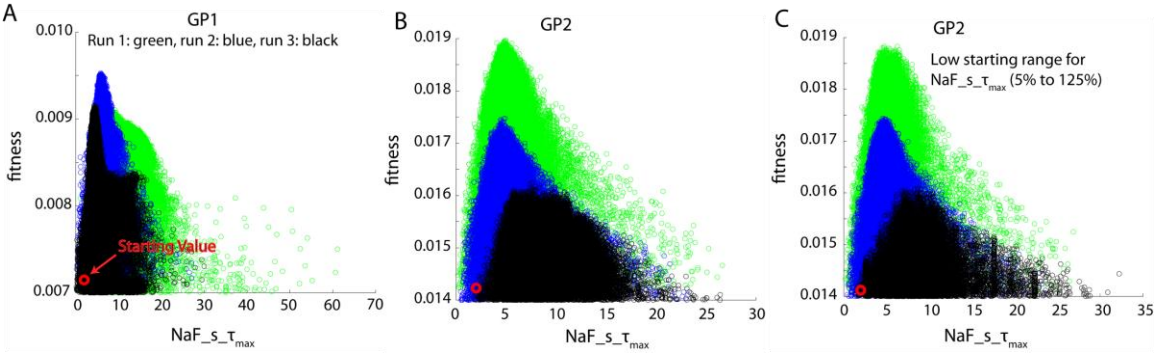

Figure 3.9: NaF_s_τmax robustly converged onto a larger value than it started with.

NaF_s_τmax was a free parameter in the GP1 and GP2 selected kinetic searches, so results for those two cells are shown. The value of NaF_s_τmax was plotted for all parameter sets with fitness at least 75% of the best fitness for that search. For each search, runs 1, 2 and 3 are represented by green, blue and black circles, respectively. The starting value of NaF_s_τmax was 2 s (red circles). A, For the GP2 densities plus properties search, the value of NaF_s_τmax converged on ~5 s as fitness increased in all three runs. The initial range was 0.4 s to 10 s. B, For the GP1 densities plus properties search, the value of NaF_s_τmax converged on ~6 s as fitness increased in all three runs. The initial range was 0.4 s to 10 s. C, For the GP2 densities plus properties search, the value of NaF_s_τmax converged on ~5 s as fitness increased in all three runs. The initial range was 0.1 s to 2.5 s (5% to 125% of the starting value).

Overall, our results suggest that when the kinetic parameters of our models were optimized we could achieve specific matching improvements which were not achieved by the density searches.

3.4.5. Optimized kinetic parameters also improved full model matches

We have argued that optimized kinetic parameters were necessary to improve the matches of our reduced models to recorded data. However, we have shown previously that full and reduced model dynamics do not match perfectly even with identical parameter sets due to morphological reduction, particularly for dendritic responses (Chapter 2). This implies that our kinetic optimization may only have been necessary to compensate for problems due to morphological reduction rather than to improve channel kinetics. However, we also showed in Chapter 2 that full model somatic input output functions can be well preserved by carefully constructed reduced models like those that we use in this article. To determine whether kinetic optimizations were merely compensating for morphological problems, we mapped the best reduced model parameter sets found in each search stage back into the full models and calculated full model fitness. We found that, similar to the reduced models, full model fitness was higher for the best kinetic search results than for the best density search results (see Supplemental Table 3-4). In terms of overall fitness and quality of mapping, the first sKS run for GP2 was typical (Fig. 3.10). Mapped dynamics were very similar for the responses to negative current injection onset (Fig. 3.10A) and offset (Fig. 3.10B). Mapped fI curves were also similar, although the full model fired a bit slower than the reduced model with positive current injection, which is a predictable result based on Chapter 2 (Fig. 3.10*C*). Spike patterns

mapped well for all three levels of current injection (Fig. 3.10*B,D,G,H*), but spike shapes were a bit shorter and wider, which is also a predictable result based on Chapter 2 (Fig. 3.10*F,I*). The overall result of successful mapping was that errors which were optimized by the kinetic searches for the reduced models also improved when those optimized kinetic parameter sets were employed in the full models. For instance, due to optimization of the activation time constant for Kv4 (Fig. 3.8*C*), the p150 AHP error decreased by 49% for the GP3 reduced model and by 59% for the GP3 full model when comparing the results of the density and selected kinetic searches. Similarly, optimization of the slow inactivation time constant of NaF allowed the p150 spike peak curve error to decrease by 63% for the GP1 reduced model and by 60% for the GP1 full model. In contrast to these two cases in which optimization of channel kinetics led to impressive decreases in errors for both full and reduced models, the optimization of the fast activation time constant of NaF may have been mostly necessary to compensate for morphological reduction (see Supplemental Fig. 3-9*D-F* for passive differences in fast responses to current injection between full and reduced models). Indeed, while the p150 spike rising phase (-1 ms to 0 ms) error decreased by 24% for the GP2 reduced model it only decreased by 8% for the GP2 full model. Nevertheless, this decrease in GP2 full model error, albeit a small one, suggests that some optimization of NaF activation properties was still possible.

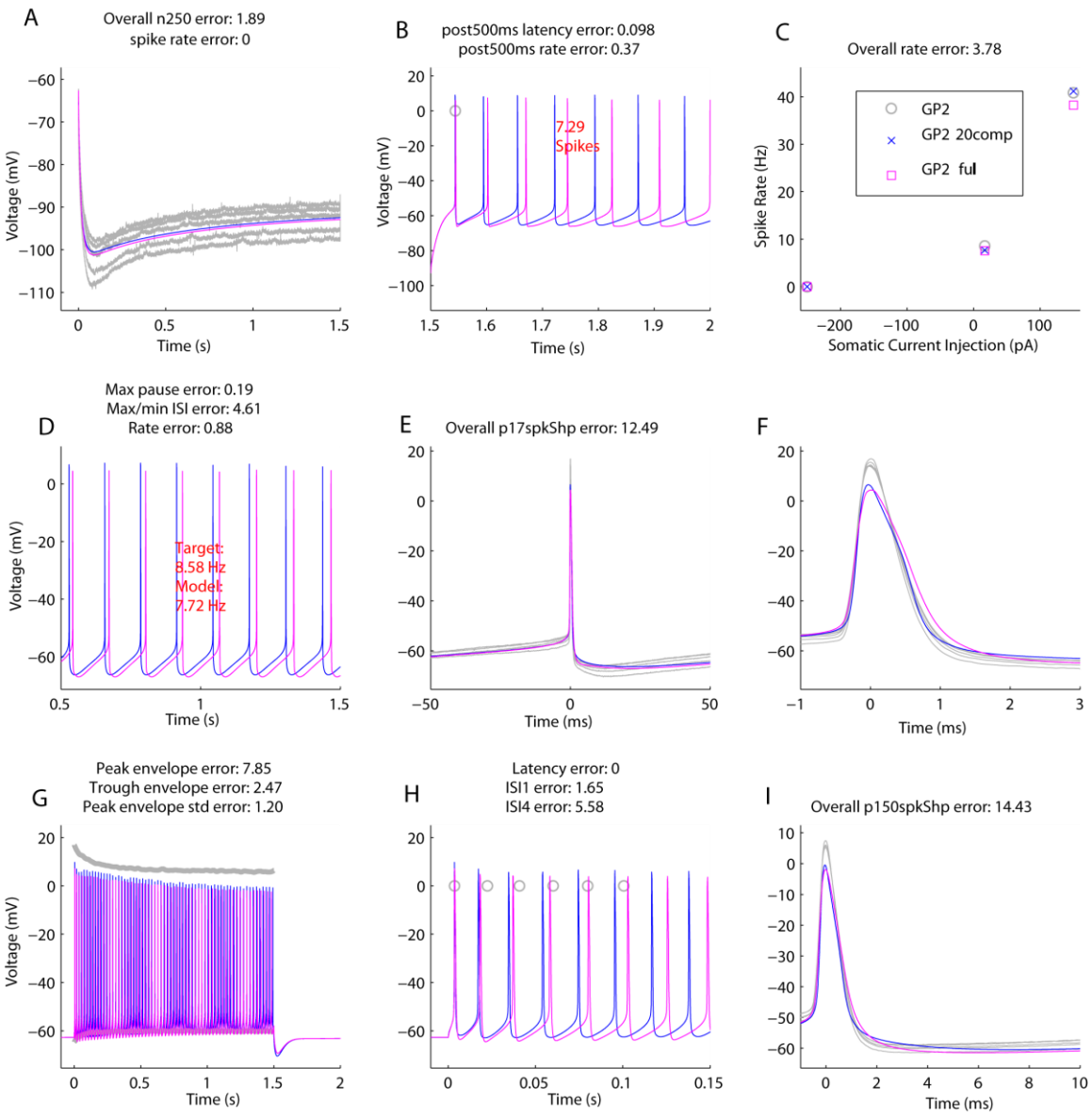

Figure 3.10: A typical example of how reduced model parameter sets can successfully map back into corresponding full models.

The output for the best parameter set found in the selected kinetic search for GP2 is shown in the reduced GP2 model (blue data) and the full GP2 model (magenta data). The overall fitness for the reduced model was 0.0190 (total combined error = 52.70) while the overall fitness for the full model was 0.0154 (total combined error = 65.11). Recordings are shown in gray to allow for easier comparison of full and reduced model output. Otherwise, panels A-I are identical to Figure 3.3.

In conclusion, most of the kinetic optimizations that we observed were necessary to improve both reduced and full models, which suggests that our channel models could be improved. Additionally, our results support that the reduced models are useful as fast search engines for improved full model kinetics.

3.5. Discussion

We have presented an analysis of the optimization of three GP neuron models. By performing successive stages of automatic parameter searches to match model output to recorded traces, we were able to attribute unavoidable data matching problems following density searches to limitations in our kinetic channel models. We were able to correct several of these limitations, such as mismatches to the p150 AHP, p150 spike rising phase, and p150 spike peak curve, by using kinetic searches with either all parameters free or only a small group selected by an error sensitivity analysis. In particular, we found that NaF and Kv4 time constants were consistently shifted in multiple parallel runs of our kinetic searches with both groups of free parameters, which indicates that our original channel models could be improved based on fitting voltage traces of recorded data while leaving kinetic parameters free. Finally, we demonstrated that these consistent shifts in parameter values were able to improve full model matches as well as reduced model matches, which suggests that kinetic optimization was necessary to compensate for incorrect kinetics rather than compensatory changes related to morphological reduction.

3.5.1. Alternatives to evolutionary searches

As an alternative to evolutionary searches, researchers have developed databases of parameter sets which can be mined for information about, for instance, correlations between parameters. The database approach is limited, however, by the number of free parameters that can be used because every additional parameter expands the size of the database multiplicatively. For example, a database including 8 conductance density parameters with 6 values each required the simulation of almost 2 million (6^8) parameter sets (Prinz et al., 2003). Because our models possessed a much larger number of free parameters, the development of a complete database would be prohibitively time consuming.

Another alternative to evolutionary searches is the gradient descent search method, which has been used to optimize simplified bursting neuron models, for example (Tien and Guckenheimer, 2008). However, due to the complexity of the parameter space of multi-compartmental conductance based neuron models (Achard and De Schutter, 2006), the gradient descent method can easily get stuck in local minima. Indeed, in several test runs of the gradient descent algorithm included with the Genesis simulation package, we found that the fitness achieved with all kinetics free was only 35% of that achieved by our staged evolutionary searches (results not shown).

3.5.2. Use of sensitivity analyses for neural modeling

In general terms, a sensitivity analysis can be either local or global in scope (i.e. either one parameter varied at a time or many) and measure either the sensitivity of error or of a model measure (such as firing rate) to parameter variation (Saltelli et al., 2000).

Sensitivity analyses of neuron models often vary parameters locally or globally in order to determine relationships between parameter values and output measures (like spike rate) (McIntyre and Grill, 1998; Tien and Guckenheimer, 2008; Weaver and Wearne, 2008). However, a different study employed global parameter variation to determine relationships between parameter values and error measures (Tabak and Moore, 1998). We used a local error sensitivity analysis, which employs elements of several of these previously used approaches, to analyze our neuron models. Due to the large computational requirements of evaluating parameter sets in compartmental neuron models, we chose a local strategy requiring many fewer simulations than would be required by a global analysis. We analyzed error sensitivity to parameter values because our goal was to find a subset of kinetic parameters most likely to improve the fitness of our density search matches. Finally, we evaluated sensitivity to individual error measures rather than overall error because this allowed us to segment parameters based on their specific capabilities and presented the opportunity to remove parameters with overlapping capabilities while keeping unique ones. As we have shown in the results, our local error sensitivity analysis successfully selected a small group of free kinetic parameters with much of the fitness improvement capability of the entire group of free kinetic parameters.

3.5.3. Implications of shifts in optimized channel kinetics

We have shown that unique shifts in fast sodium channel inactivation and A-type potassium channel (Kv4) activation kinetics were necessary to obtain optimized matches in our searches. What could explain the need for these new values?

The fast sodium channel that we include in our models is based on a recent characterization done in acutely dissociated mouse GP neurons (Mercer et al., 2007). Despite being the most thorough study of fast sodium channel kinetics in GP to date, the unavoidable use of dissociated neurons to prevent space clamp errors may have led to differences in channel kinetics compared to whole cell recordings. Indeed, it would not be surprising for fast sodium channel inactivation kinetics to differ between acutely dissociated and slice GP neurons because it has been shown that the gating properties of fast sodium channels can be altered by binding with multiple diffusible and membrane bound factors. For instance, calmodulin binding accelerates the fast inactivation of fast sodium channels (Herzog et al., 2003). Constitutive phosphorylation of fast sodium channels was found to underlie the inactivation kinetics necessary to produce resurgent sodium current (Grieco et al., 2002). And, recovery from inactivation of fast sodium channels is slowed by interaction with fibroblast growth factor homologous factor 2A (Rush et al., 2006). In addition to introducing variability between slice and dissociated neurons, modulations like these could also introduce kinetic variability between different neurons that were prepared in the same way. This possibility could explain why we did not observe shifts that were consistent across all three of our neurons.

In addition to the potential sources of kinetic variability discussed above, fast sodium channel gating property variability could arise from species differences. Indeed, while the gating properties of fast sodium channels have not been directly compared between species in the same cell type, a recent study showed that Ih gating kinetics vary between the CA1 pyramidal neurons of rats and mice (Routh et al., 2009). Therefore, species variability may necessitate the fine tuning of channel kinetics based on

electrophysiological recordings if channels were characterized in other species. In sum, setting the kinetics of the fast sodium channel free was motivated by: 1) differences in the recording and characterization environments (slice vs dissociated) which could lead to different modulation of the channel, 2) potential differences in modulation state between the three neurons (recorded on different days, from different animals, with subtle unavoidable variations in experimental protocol), and, 3) by potential species differences in kinetics.

The Kv4 channel that we include in our models is based on an electrophysiological characterization of A-type current in acutely dissociated rat GP neurons (Tkatch et al., 2000). Most likely due to experimental difficulties with characterizing kinetics in voltage regimes with low levels of channel activation, this otherwise thorough study was only able to provide activation time constants between -40 mV and +50 mV. In order to use the channel in our models, we extrapolated the Kv4 activation time constant curve into the hyperpolarized regime (e.g. -60 mV to -50 mV) which we have shown is important for shaping AHPs during fast spiking (Fig. 3.8*A*-*C*). Also, it was necessary to extrapolate channel kinetics based on temperature because the channel characterization was done at 20-22° C while our slice recordings were done at 32° C. Therefore, there are three likely reasons that our kinetic searches optimized the Kv4 time constant curve in the hyperpolarized regime: 1) the temperature dependent extrapolation of the channel's kinetics may have been imperfect, 2) hyperpolarized activation kinetics were difficult to experimentally constrain, and, 3) regulation of Kv4 channels may differ between dissociated GP neurons where the characterization was done and our recordings in slice GP neurons, or even between multiple slice neurons. Indeed,

Kv4 gating properties are known to depend on phosphorylation state as well as on interaction with other cellular factors. For instance, Kv4 channels are phosphorylated by protein kinases A and C which causes a depolarizing shift (~15 mV) in the voltage-dependent activation curve (Hoffman and Johnston, 1998). Dipeptidyl peptidase 10, a Kv4 accessory subunit expressed throughout the brain (Allen et al., 2003), was found to modify most gating properties of Kv4 channels (Jerng et al., 2004). Therefore, it would not be surprising for Kv4 gating properties in acutely dissociated GP neurons to differ from those properties in GP neurons recorded in slice. Also, we only observed shifts in Kv4 gating properties for one out of three neurons. As for fast sodium channel inactivation kinetics, modulations like those just discussed could introduce kinetic variability between different slice neurons, which could explain why we did not observe shifts that were consistent across all three of our neurons.

In sum, we suggest that: 1) the activation kinetics of Kv4 channels in the hyperpolarized regime are important for spike AHP shape and need to be characterized in slice GP neurons, 2) the inactivation kinetics of fast sodium channels may be slower in slice rat GP than in dissociated mouse GP neurons, and, 3) kinetics may need to be characterized for each recorded cell due to the possibility of unique modulation states for each neuron.

3.5.4. Conclusion

Compartmental conductance based models often use channel kinetics taken directly from experimental voltage clamp studies. While such studies cannot be replaced by computational experiments like ours, it is clear that channel kinetics provided by

voltage clamp recordings cannot be taken as a gold standard, particularly for other models of other cell types, species, or experimental preparations without careful validation. Because such validation would be extremely time consuming and labor intensive, it may be preferable for modelers to set kinetics free during model tuning in order to optimize channel kinetics from the solid starting point provided by voltage clamp experiments. Indeed, our findings indicate that setting kinetics free provides not only improved data matching over conductance density tuning but also additional information about what channel kinetics may have been present in the recorded cell.

3.6. Supplemental Material

3.6.1. Supplemental Text

3.6.1.1. Equations used to generate the shifts and scalars for the sensitivity analyses

To generate scalars between ~0.1 and ~10, the following equations were used:

$$scalar = \left\{ \begin{array}{l} (\tan x)^4 * 1.5 + 1, x > 0 \\ \dfrac{1}{(\tan x)^4 * 1.5 + 1}, x \le 0 \end{array} \right\} \text{ for x = -1:0.1:1}$$

shift = x^3 for x = -0.3:0.03:0.3

Based on these equations, the scalars were 0.10, 0.21, 0.37, 0.57, 0.75, 0.88, 0.95, 0.99, 0.9975, 0.9998, 1.0002, 1.0025, 1.01, 1.05, 1.13, 1.33, 1.76, 2.7, 4.8, and 9.8. The shifts were (in mV) -27, -19.7, -13.8, -9.3, -5.8, -3.4, -1.7, -0.73, -0.22, -0.027, +0.027, +0.22, +0.73, +1.7, +3.4, +5.8, +9.3, +13.8, +19.7, and +27.

3.6.1.2.The error function

The RMSE was used to compare voltage traces that were not rapidly changing. To compare the rapidly changing voltage trajectories during a spike, a 'phase plane' error measure was used. Briefly, we plotted the model and target voltage trajectories in a phase plane. We matched the points and summed the distances between matching points to generate the phase plane error. This error measure is visualized to aid comprehension (Supplemental Fig. 3-1).

Measures included in the error function (30 total):

Derived from the response to -250 pA injection (9 measures):

RMSE of Response from 0 ms to 100 ms

RMSE of Response from 100 ms to 200 ms

RMSE of Response from 200 ms to 300 ms

RMSE of Response from 300 ms to 500 ms

RMSE of Response from 500 ms to 1000 ms

RMSE of Response from 1000 ms to 1500 ms

Spike rate during injection

Latency to first spike following offset of injection

Spike rate for the 500 ms following offset of injection

Derived from the response to +16.66 pA injection (8 measures):

RMSE of spike shape from -50 ms to -1 ms

Phase plane error of spike shape from -1 ms to 0 ms

Phase plane error of spike shape from 0 ms to +1 ms

Phase plane error of spike shape from +1 ms to +2 ms

RMSE of spike shape from +2 ms to +50 ms

Maximum interspike interval (ISI) divided by minimum ISI

Maximum pause (time without a spike) during injection

Spike rate from 0.5 s to 1.5 s following onset of injection (~steady state)

Derived from the response to +150 pA injection (13 measures):

Phase plane error of spike shape from -1 ms to 0 ms

Phase plane error of spike shape from 0 ms to +1 ms

Phase plane error of spike shape from +1 ms to +2 ms

RMSE of spike shape from +2 ms to +10 ms

First ISI following onset of injection

Fourth ISI following onset of injection (chosen because it was a marker of doublets when coupled with the first ISI)

Coefficient of variation of the ISIs from 1 s to 1.5 s following onset of injection (~steady state)

Latency to first spike following onset of injection

Spike rate for the 500 ms following offset of injection

RMSE of the best fit curve to the spike peak voltages during injection

RMSE of the best fit curve to the spike trough voltages during injection

Standard deviation of the spike peaks from 1 s to 1.5 s following onset of injection (~steady state)

Spike rate from 1 s to 1.5 s following onset of injection (~steady state)

3.6.1.3.Particle swarm optimization algorithm

Our evolutionary algorithm (EA) modeled 'n' parameter sets as particles traveling through parameter space pursuing the fittest particle in their neighborhood. To avoid bias due to starting position, each search consisted of 3 runs with n = 1000 randomly generated particles. Each particle in each run was chosen independently of all others. An example in two dimensions of the initial distribution of particles can be seen in Supplemental Figure 3-2. Each particle had a memory of the highest fitness position that it had ever occupied, so we kept the fittest parameter sets. Each particle had a defined neighborhood with 'q' other particles in it (q = 100 for all searches in this paper). Particles started at their current position and spent the next 't' time steps traveling on a linear path with constant velocity. They traveled to a position overshooting the fittest position in their neighborhood by a percentage 'p' to reach a "temporary target", preventing our EA from converging too quickly (p = 43.34458…% for all searches in this paper). We chose p to be an irrational number less than 100% to avoid the repeat testing of points and to ensure that our EA eventually converged. t = 10 for all searches in this paper to simplify analysis of progress, calculations, and coding. We decided to use constant speed particles in our EA because the convergence behavior of variable speed particles can be difficult to predict (Clerc and Kennedy, 2002). We allowed our EA to proceed in this manner until 20 time steps passed with an improvement of less than 1%; this was our termination criterion. We found that it was worthwhile to perform two searches where the randomly generated parameter sets for the second search were generated based on the best parameter sets of the first search.

We compared the performance of our modified particle swarm EA to the simulated annealing algorithm preferred by Vanier and Bower for optimizing the parameters of neuronal models (Vanier and Bower, 1999). For this comparison, each algorithm was allowed to start fresh 10 times and test 10,000 parameter sets each time for a total of 100,000 tested parameter sets as was done by Vanier and Bower. Each algorithm required practically identical amounts of time because compartmental neuron calculations dominated CPU usage. The two algorithms produced solutions whose average quality was not significantly different ($p = 0.7449$, $n = 10$, Student's t-test). Therefore, for the purposes of optimizing the parameters of neuron models, our EA was just as effective as the simulated annealing algorithm preferred by Vanier and Bower.

3.6.1.4.Selection process for similar kinetic parameters

When multiple parameters had very similar capabilities, we only selected the best parameter for our searches. For example, three parameters which affect the fast inactivation time constant curve of the fast sodium channel exhibited very similar capabilities in our error sensitivity analysis for cell GP1 (Fig. 3.5*B*). These three parameters were not mathematically identical (Supplemental Fig. 3-6), but they all were capable of improving the same five spike shape related error measures with a shift in value that was consistent for each parameter. NaF_h_$K_{\tau 2}$ (which affects the slope of the time constant curve in the depolarized regime) had to scale up by about 2x to produce the improvements while NaF_h_τ_{min} (which determines the minimum time constant) had to scale up by about 3x and NaF_h_τ_{max} (which determines the minimum time constant) had to scale up by about 1.5x. In this case, NaF_h_$K_{\tau 2}$ was selected as the free parameter for

our GP1 sensitivity analysis guided kinetic searches because it had all of the spike shape improvement capabilities of NaF_h_τ_{min} and NaF_h_τ_{max} while also possessing the ability to improve the p150 spike rate, which could allow the search to find better matches.

3.6.2. Supplemental Figures

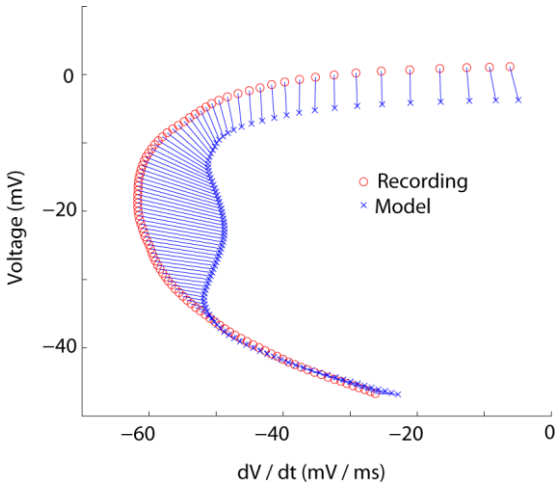

Supplemental Figure 3-1: Visual representation of our phase plane error measure.
To calculate the phase plane error for measures including spike voltage traces, we plotted the recorded and model voltage traces in two dimensional phase space. The ordinate of this space was voltage (in units of mV) while the abscissa was change in voltage with time (dV / dt in units of mV / ms). Each set of points was aligned by spike time. The error was equal to the sum of the Euclidean distances between all points in phase space.

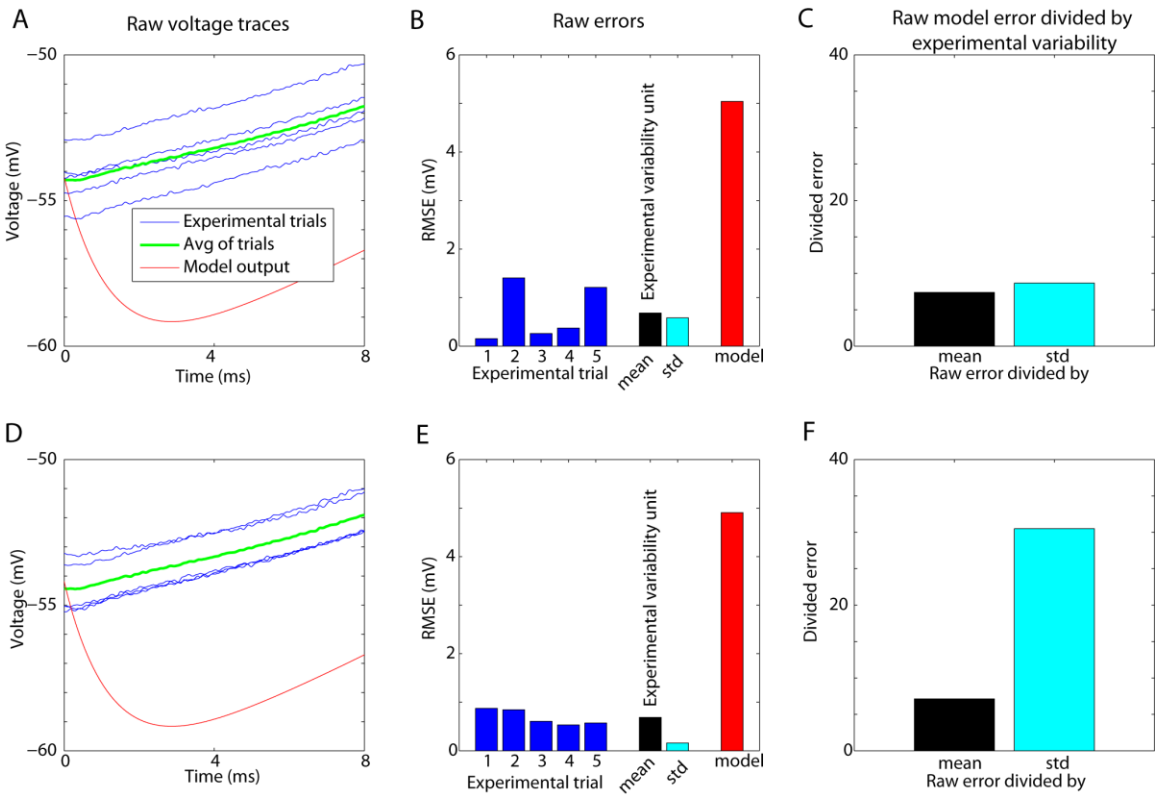

Supplemental Figure 3-2: Raw errors were divided by an experimental variability unit.

A, Raw voltage traces are plotted for 5 experimental trials (blue traces), for the average of these 5 trials (green trace) and for model output (red trace). B, The RMSE was calculated when comparing each of the five experimental trials (blue bars) or the model output (red bar) against the average of the experimental trials. Note the similarity between the mean experimental RMSE ('mean') and the standard deviation of the experimental RMSEs ('std'). C, The model RMSE was divided by either the mean RMSE or the standard deviation of the RMSEs. Note the similarity between the resulting divided errors. D, Same as panel A, except that the experimental traces were shifted up or down to change their distribution. E, With this set of experimental traces, the mean RMSE is similar to that in panel B while the standard deviation of the RMSEs is much smaller. F, The result when dividing the model RMSE by the mean RMSE is unchanged while the result when dividing the model RMSE by the standard deviation of the RMSEs is much larger than in panel C. Due to the consistency of the mean RMSE between different possible distributions of experimental data (panel A vs. panel D), the mean RMSE was used as the experimental variability unit.

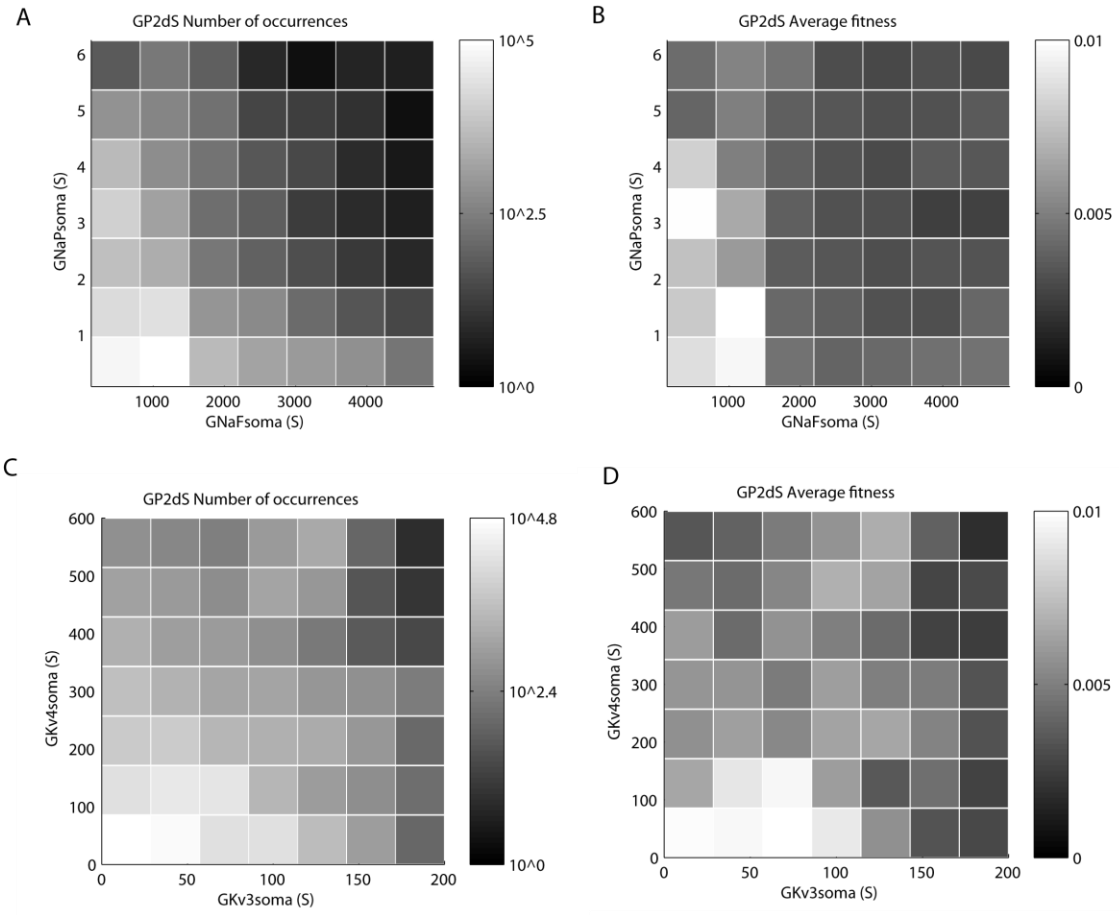

Supplemental Figure 3-3: Search algorithm spent more time in high fitness regions of parameter space.

Every parameter set that was simulated in the second set of GP2 density searches ('dS') was used to generate heat maps. *A*, Number of parameter sets simulated varied by region of the two dimensional parameter space formed by somatic NaP and NaF conductance densities. A logarithmic color scale was used due to the large variation between bins (see grayscale bar). *B*, Average fitness varied by region of parameter space for somatic NaP and NaF conductance densities. Average fitness tended to be higher in regions that were more heavily sampled (compare panels A and B). A linear color scale was used to highlight differences in fitness (see grayscale bar). *C-D*, These panels are identical to A and B, except that the two dimensional parameter space is formed by somatic Kv3 and Kv4 conductance densities.

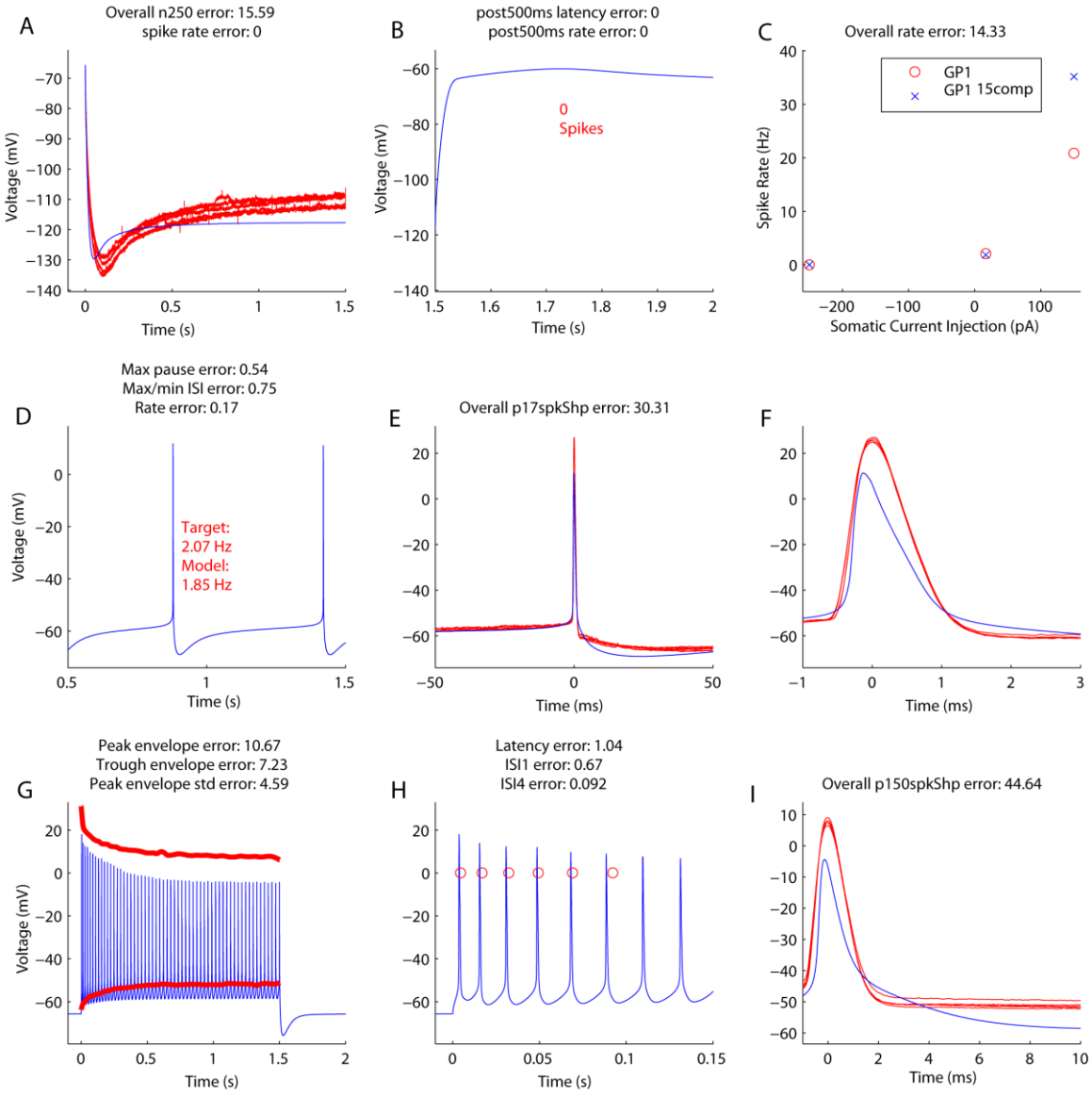

Supplemental Figure 3-4: An example of how optimized conductance densities could still allow many mismatches between reduced model output and electrophysiological recordings.

This figure shows the best parameter set found by the density searches for the GP1 reduced model (total combined error = 136.79, fitness = 0.0073) but is otherwise identical to Figure 3.3.

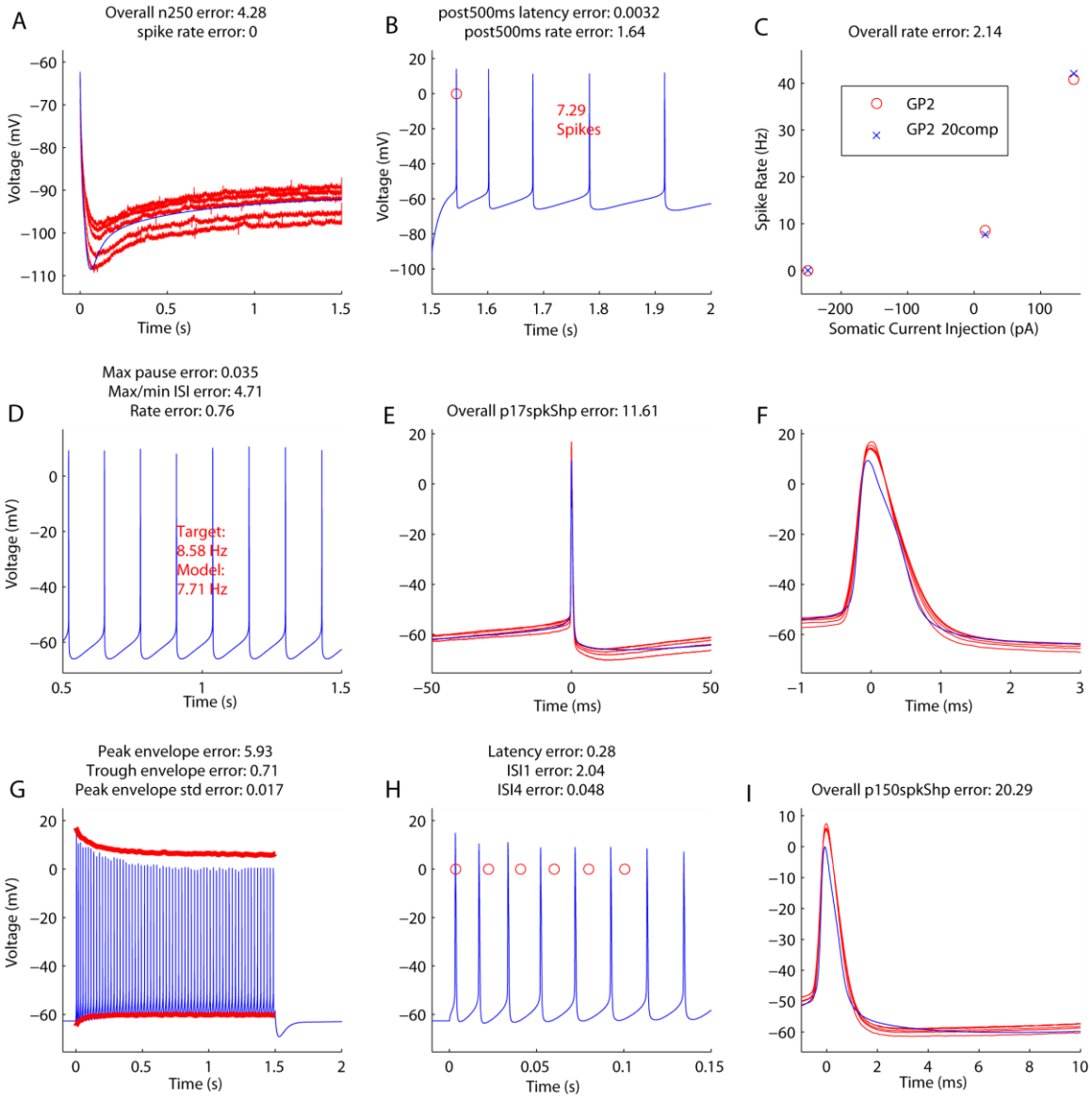

Supplemental Figure 3-5: An example of how optimized conductance densities could provide very close matches between reduced model output and electrophysiological recordings.

This figure shows the best parameter set found by the density searches for the GP2 reduced model (total combined error = 62.28, fitness = 0.0161) but is otherwise identical to Figure 3.3.

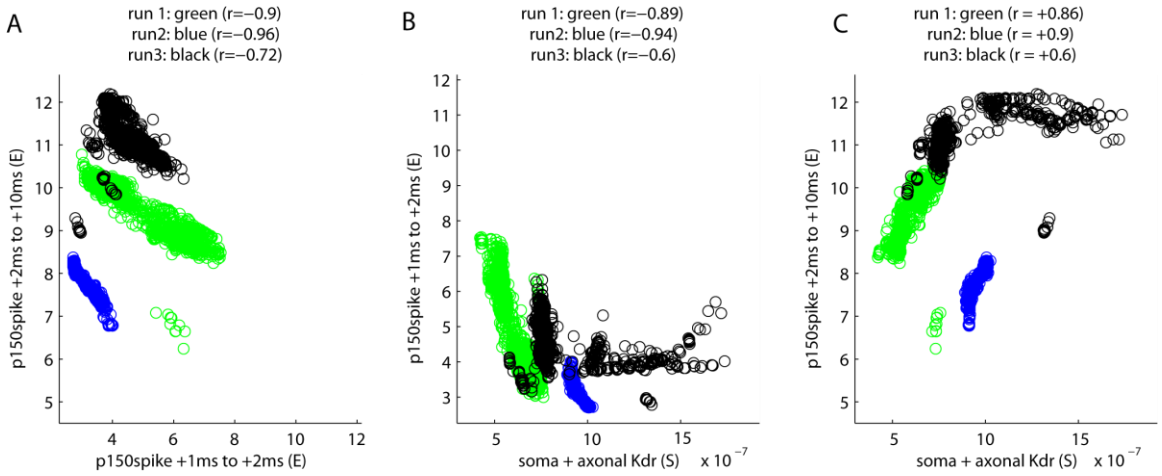

Supplemental Figure 3-6: Error tradeoffs were consistent between all three parallel density search runs despite different randomly generated populations of parameter sets.

This figure is similar to Figure 3.4 except that, in addition to parameter sets 95% as fit as the best set overall (still plotted in blue), we have also plotted the parameter sets from the other two parallel runs that were 95% as fit as the best set within that run (1868 parameter sets for run 1, 2109 parameter sets for run 2, and 3450 parameter sets for run 3). *A*, The error for the p150 AHP was negatively correlated with the error for the p150 falling phase for all three runs. *B*, The error for the p150 falling phase was negatively correlated with soma + axonal Kdr for all three runs. *C*, The error for the p150 AHP was positively correlated with soma + axonal Kdr for all three runs.

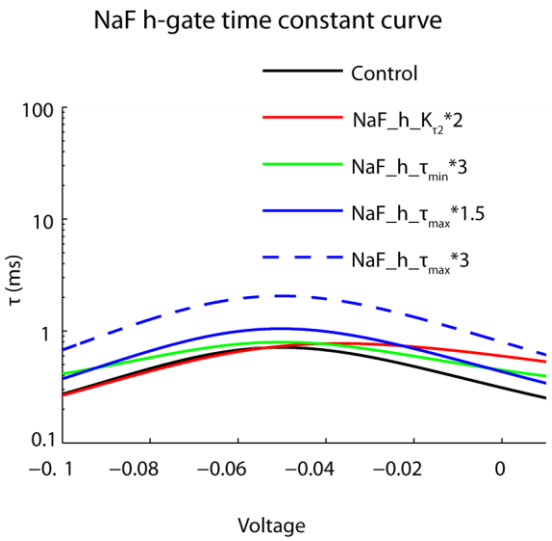

Supplemental Figure 3-7: Three parameters from the h-gate of the NaF conductance highlighted by error sensitivity analysis affect the time constant curve in unique ways.

The control time constant curve is shown for comparison. The parameter changes suggested by the error sensitivity analysis (panel B) are shown. Doubling NaF_h_$K_{\tau 2}$ decreased the slope of the curve at depolarized voltages but did not affect the curve at hyperpolarized voltages. Tripling NaF_h_τ_{min} decreased the slope of the curve at both hyperpolarized and depolarized voltages, but did not greatly affect the maximal time constant. Increasing NaF_h_τ_{max} by 50% shifted the time

constant curve upward but did not noticeably affect the slope of the curve. Similarly, tripling NaF_h_τ_{max} shifted the curve even further upward but still did not noticeably affect the slope of the curve.

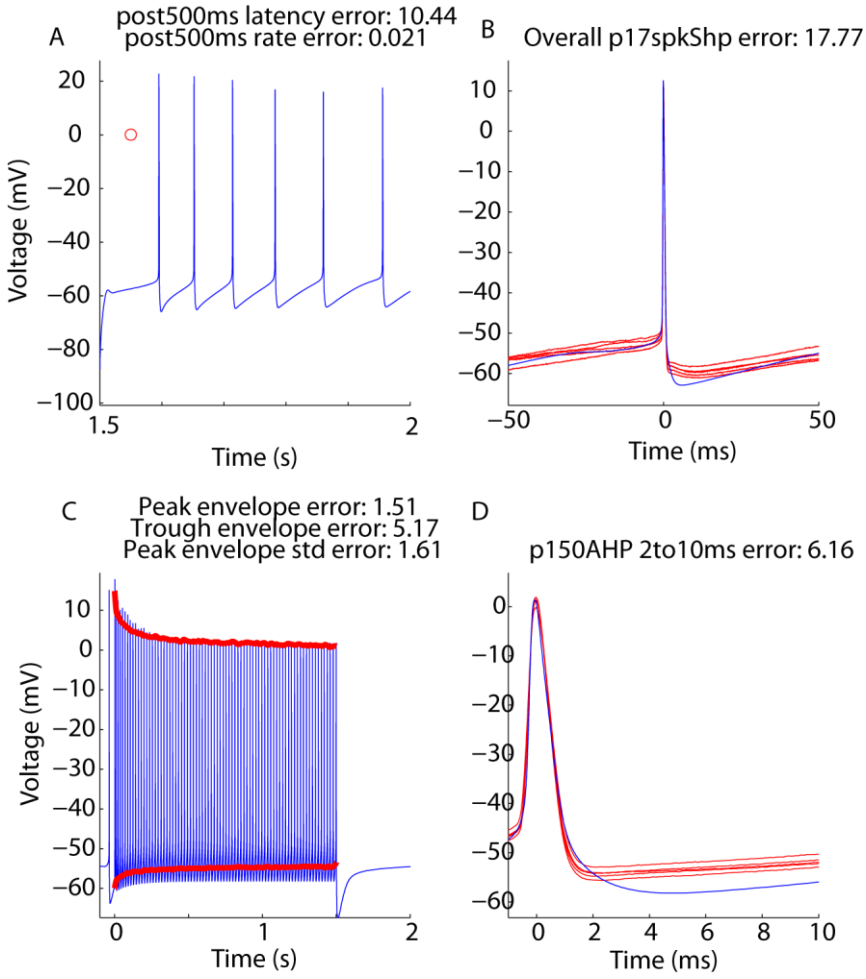

Supplemental Figure 3-8: A typical example of how optimized channel properties not selected based on the error sensitivity analysis failed to improve the density matches.

This figure shows the best parameter set found by the ineffective kinetic search for the GP3 reduced model (total combined error = 84.18, fitness = 0.0119). Only important differences with Figure 3.3 are shown. *A*, The reduced model fired later than did the recorded cell following offset of -250 pA injection. *B*, p17 spike shape. The reduced model failed to match the p17 spike shape during the first 10 ms of the AHP. *C*, Accommodation to +150 pA injection (p150). The peaks match those of the recordings but the troughs are still too hyperpolarized. *D*, p150 AHP. The reduced model AHP was still hyperpolarized relative to the recordings, with a mismatch that was comparable in magnitude to that shown in Figure 3.3.

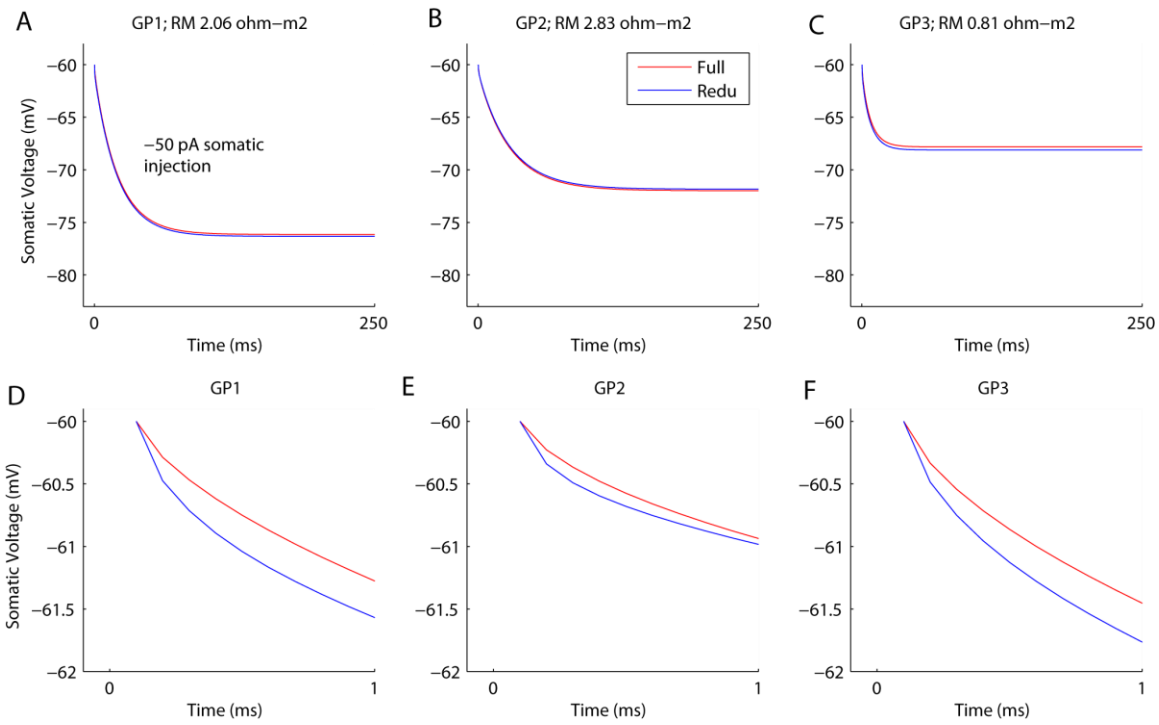

Supplemental Figure 3-9: Mapping success depended on the passive match between full and reduced models, particularly for fast events like spikes.

Negative current (-50 pA) was injected into the soma of each full and reduced model. *A-C*, The responses of the GP1, GP2 and GP3 models to negative DC injection. The full and reduced models have very similar steady state responses. *D-F*, The responses of the GP1, GP2 and GP3 models to negative current injection in the first 1 ms. The GP2 full and reduced model responses match more closely than do the GP1 and GP3 full and reduced model responses.

3.6.3. Supplemental Tables

Supplemental Table 3-1: Voltage-dependent gates.

Properties of the Na_P slow inactivation (s) gate:

$$\alpha(V_m) = [(A_\alpha * V_m) + B_\alpha] / [1 - \exp ((V_m + (B_\alpha / A_\alpha)) / K_\alpha)]$$

$$\beta(V_m) = [(A_\beta * V_m) + B_\beta] / [1 - \exp ((V_m + (B_\beta / A_\beta)) / K_\beta)]$$

$$\tau (V_m) = 1 / (\alpha(V_m) + \beta(V_m))$$

For a more detailed description of the voltage dependent gates used in this study, see (Gunay et al., 2008). The NaF conductance incorporates data from the recent characterization of the kinetics of fast sodium channels in GP (Mercer et al., 2007). Gates: m and n are activation gates; h is an inactivation gate; and, s is a slow inactivation gate (only present for NaF and NaP channels).

Channel	Gate	Pwr	Min_{inf}	$V_{0.5inf}$ mV	K_{inf} mV	τ_{min} ms	τ_{max} ms	$V_{\tau max}$ mV	$K_{\tau 1}$ mV	$K_{\tau 2}$ mV
Na_F	m	3	0	-38.8	7.3	0.033	0.49	-41.8	10	33
Na_F	h	1	0	-53.7	-5	0.25	4	-53.7	25	32
Na_F	s	1	0	-53.7	-5	1	2000	-53.7	60	16

Na_P	m	3	0	-57.7	5.7	0.03	0.146	-42.6	14.4	14.4
Na_P	h	1	0.154	-57	-4	10	17	-34	26	31.9
Na_P	s	1	0	-10	-4.9					
K_V2	n	4	0	-33.2	9.1	0.1	30	-33.2	21.7	13.9
K_V2	h	1	0.2	-20	-10	3400	3400	NA	NA	NA
K_V3	n	4	0	-26	7.8	0.1	14	-26	13	12
K_V3	h	1	0.6	-20	-10	7	33	0	10	10
K_V4_{fast}	n	4	0	-49	12.5	0.25	7	-49	29	29
K_V4_{fast}	h	1	0	-83	-10	7	21	-83	10	10
K_V4_{slow}	n	4	0	-49	12.5	0.25	7	-49	29	29
K_V4_{slow}	h	1	0	-83	-10	50	121	-83	10	10
KCNQ	n	4	0	-61	19.5	6.7	100	-61	35	25
Ca_{HVA}	m	1	0	-20	7	0.2	0.2	-20	NA	NA
HCN_1	m	1	0	-76.4	-3.3	0	3625	-76.4	6.56	7.48
HCN_2	m	1	0	-87.5	-4	0	6300	-87.5	8.9	8.2

Channel	A_α mV^{-1} ms^{-1}	B_α ms^{-1}	K_α mV	A_β mV^{-1} ms^{-1}	B_β ms^{-1}	K_β mV
Na_P	-2.88 X 10^{-6}	-4.9 X 10^{-5}	4.63	6.94 X 10^{-6}	4.47 X 10^{-4}	-2.63

Supplemental Table 3-2: Calcium-dependent gate.

SK channel calcium dependence (n = the Hill Coefficient):

$X_{inf}([Ca^{2+}]) = [Ca^{2+}]^n / ([Ca^{2+}]^n + (EC_{50})^n)$

SK channel kinetics:

--for $[Ca^{2+}] < [Ca^{2+}]_{Sat}$, $\tau([Ca^{2+}]) = \tau_{max} - ([Ca^{2+}] * [(\tau_{max} - \tau_{min}) / K_{\tau\text{-}Ca}])$

--for $[Ca^{2+}] > = [Ca^{2+}]_{Sat}$, $\tau([Ca^{2+}]) = \tau_{min}$

Channel	Gate	Pwr	$[Ca^{2+}]_{Sat}$ (µM)	EC_{50} (µM)	$K_{\tau\text{-}Ca}$ (ms/µM)	Hill Coeff
SK_{Ca}	m	1	5	0.35	14.4	4.6

Supplemental Table 3-3: Selected and ineffective kinetic parameters.

Property parameters selected based on error sensitivity analysis. Kinetic parameters are referred to in the following way: channel (underscore) gate (underscore) parameter. Selected parameters were chosen because they met our criteria for error measure improvement without large decreases in overall fitness. Ineffective parameters were chosen from the same channel and gate (whenever possible) as the selected parameters, but unlike the selected parameters, they were usually unable to improve error measures by enough to meet our criteria. Exceptions are italicized. '$B_{CaGPconc}$' is a parameter that determine the relationship between calcium current and concentration.

GP1 sKS	GP1 iKS	GP2 sKS	GP2 iKS	GP3 sKS	GP3 iKS
NaF_m_τ_{max}	NaF_m_K_{inf}	NaF_m_$K_{\tau 2}$	NaF_m_$V_{0.5in}$	NaF_m_$K_{\tau 2}$	NaF_m_$V_{0.5in}$

			$_f$		$_f$
NaF_h_$K_{\tau 2}$	*NaF_h_K_{inf}*	NaF_h_K_{inf}	*NaF_h_$V_{0.5inf}$*	NaF_h_τ_{min}	NaF_h_$V_{0.5inf}$
NaF_s_τ_{max}	*NaF_s_τ_{min}*	NaF_h_$K_{\tau 1}$	*NaF_h_τ_{max}*	NaF_s_K_{inf}	NaF_s_$K_{\tau 2}$
Kv2_n_$K_{\tau 1}$	Kv2_n_$K_{\tau 2}$	NaF_s_τ_{max}	NaF_s_τ_{min}	Kv2_n_$K_{\tau 1}$	Kv2_n_τ_{min}
Kv2_n_τ_{max}	Kv2_n_τ_{min}	Kv4_n_τ_{max}	Kv4_n_$V_{0.5inf}$	$Kv4_{fast}$_n_$K_{\tau 1}$	Kv4_n_$V_{0.5inf}$

Cell	Density search	Selected kinetic search	Ineffective kinetic search	All kinetic search	
Kv4_n_τ_{max}	Kv4_n_K_{inf}	HCN_1_m_$K_{\tau 1}$	HCN_1_m_K_{inf}	$Kv4_{slow}$_h_τ_{min}	Kv4_h_$V_{0.5inf}$
SK_m_τ_{max}	SK_m_$Hill_{coef}$	HCN_2_m_$K_{\tau 2}$	HCN_2_m_K_{inf}	HCN_1_m_$K_{\tau 1}$	HCN_1_m_ $V_{0.5inf}$
Ca_{HVA}_m_$V_{0.5inf}$	$B_{CaGPconc}$	gNaF	gNaF	HCN_2_m_$K_{\tau 2}$	HCN_2_m_$K_{\tau 1}$
HCN_2_m_$V_{0.5inf}$	HCN_2_m_$K_{\tau 2}$	gKv4	gKv4	gNaF	gNaF
gNaF	gNaF	gHCN	gHCN	gKv2	gKv2
gKv2	gKv2			gKv4	gKv4
gKv4	gKv4			gHCN	gHCN
gSK	gSK				
gCaHVA	gCaHVA				
gHCN	gHCN				

GP1	0.0055 (82.3%)	0.0082 (86.5%)	0.0058 (82.5%)	0.0096 (82.2%)
GP2	0.0147 (91.6%)	0.0177 (101%)	0.0137 (101%)	0.0172 (83.7%)
GP3	0.0074 (75.0%)	0.0083 (62.7%)	0.0080 (67.2%)	0.0109 (67.1%)

Supplemental Table 3-4: Mapped full model fitness.

Mapping back to full model success. For each run of the second set of each stage, the best reduced model parameter set was mapped back into the full model and the fitness was calculated. The percentage of the reduced model's fitness maintained by the full model is listed in parentheses after the full model's raw fitness score for the parameter sets which mapped most successfully (ranked by full model fitness score).

CHAPTER 4: GENERAL DISCUSSION

4.1.Thesis Summary

The overall goal of my thesis was to first improve our understanding of the capabilities of models with reduced branching structure and then to build on that understanding to improve channel kinetics using automated searches. To improve our understanding of the capabilities of reduced models, I developed morphological reduction methods which either preserved or did not preserve branching structure and carefully compared each type of reduced model to the original GP full model. One of the results of these comparisons was that unbranched models could maintain most of the somatic input output functionality of the full model from which they were derived while greatly decreasing computational cost. This result allows unbranched reduced model parameter sets found by automated searches to 'map back' those same parameter sets into a full model. I built on this result by using unbranched reduced models as a computationally efficient replacement for full models in order to improve channel kinetics with automated searches. During optimization to match recorded data, my automated searches consistently shifted certain channel properties. This result suggested that those properties should change from their original experimentally determined values, possibly due to modulation in our recorded cells.

The goal of aim 1 was to improve our understanding of which features of neuronal processing require detailed dendritic branching structures. To this end, I analyzed the processing capabilities of branched or unbranched reduced models which were created by collapsing the dendritic tree of a morphologically realistic full GP neuron

model. I found that somatic input processing into somatic output was well preserved by both types of reduced model. In contrast, I found that the processing of dendritic inputs was better preserved by branched than unbranched reduced models. However, if dendritic inputs caused strong local nonlinearities (e.g. dendritic sodium spikes), then neither type of reduced model was able to adequately preserve full model processing capabilities. Based on my analyses, I provided recommendations for reduced model construction and indicated which level of reduction is most suitable for different applications. I finally demonstrated that unbranched reduced models were ideally suited for automated searches of full model parameter space if only somatic inputs and outputs were available, as is frequently the case experimentally.

The goal of aim 2 was to detect potential improvements to channel properties by matching model output to experimental recordings. To this end, I analyzed the optimization of the parameters of unbranched reduced models of three electrophysiologically characterized and morphologically reconstructed GP neurons. To allow an analysis of potential channel property improvements, I used different sets of free parameters in two stages of automatic parameter searches. In the first stage, conductance densities were set free. I found that even the best density matches exhibited unavoidable problems which were due to limitations in our channel models. To correct these limitations, I set channel kinetics free in second stage searches. I found that the unavoidable mismatches exhibited after the first stage searches were greatly improved after the second stage searches. Additionally, I found that some channel properties consistently shifted to new values in multiple cells, which suggested that our channel models could be improved. I concluded that, while there is no substitute for experimental

channel property data, such data should be considered a starting point rather than a gold standard for modelers. This is particularly true when channels were characterized under different experimental conditions than recorded data to be matched by a model.

4.2. Recommendations for Modelers Regarding Morphological Complexity

Computational studies of neurons and neural networks often use models with reduced morphological complexity but infrequently justify this choice. With aim 1 of my thesis, I strove to offer modelers principles upon which to make more rational choices of model complexity based on comparisons between models with different levels of morphological reduction. One of my strongest recommendations is that the complexity of a model should be appropriate for the hypothesis being tested. There are several broad categories of hypotheses for which models with different levels of morphological reduction are appropriate.

The first type of hypothesis does not involve complex dendritic processing; such hypotheses are ideally suited for unbranched reduced models both because their reduced dendritic morphologies still allow for the faithful reproduction of somatic input output functions and because their small number of compartments allow for fast simulations. Their speed is particularly important when simulating a large number of neuron models, as in a network, and when testing a large number of parameter combinations, as in my automated searches of aim 2. For such applications, unbranched reduced models are preferable to branched reduced models to the extent that they require fewer compartments in order to match the somatic input-output function of a full model. In aim 1, I showed

that unbranched reduced models with > 10 compartments can replicate the somatic responses of a full morphological globus pallidus model while branched models required > 40 compartments. Therefore, for automated searches or network models which do not involve complex dendritic processing, these unbranched models with few compartments would be preferable to the branched models possessing many more compartments.

The second category of hypothesis involves some type of complex dendritic processing like synaptic coding with active dendritic conductances. In aim 1, I showed that such a hypothesis requires the use of branched reduced models in order to approximate the activity of a full model because the activation of dendritic conductances depends on local voltage responses which themselves depend on dendritic branching structure. Therefore, while unbranched reduced models were not completely incapable of accurate processing, they were clearly inferior to the branched models due to important differences with the full model in their dendritic branching structure and therefore in their dendritic voltage responses.

The third category of hypothesis involves highly non-linear dendritic activity such as the generation of dendritic sodium spikes. In aim 1, I found that even branched reduced models failed to preserve full model dendritic dynamics in the presence of a high level of dendritic fast sodium conductance which allowed dendritic spike initiation. Indeed, I found full model dendritic spike initiation depended so sensitively on the amplitude of local dendritic voltage fluctuations that no reduced model was able to maintain it. This was because dendritic high frequency input impedance was imperfectly matched by the branched reduced models and poorly matched by the unbranched models. I found that dendritic input impedance was a key determinant of the local voltage

response to synaptic or axial events (like bAPs) and therefore the amount of local voltage-gated conductance activation. Indeed, in the presence of a medium level of dendritic fast sodium conductance capable of amplification of voltage events but not dendritic sodium spike generation, maximal full model bAP amplitudes could not be matched by even the branched reduced models. However, these bAP amplitude mismatches were confined to limited regions of the dendritic tree suggesting that branched reduced models can be employed in studies where bAPs occur but do not need to be perfectly replicated. Unbranched reduced models are less suitable for this purpose, although they are not completely inaccurate.

Overall, unbranched reduced models provide the most computationally efficient solution for studies of somatic input-output relationships. Branched reduced models provide a compromise solution for studies which involve moderate dendritic processing, including synaptic input with active conductances. And, full models must still be used if there is significant nonlinear dendritic processing.

4.3. Hypothesized improvements to channel kinetics

Based on the search results of aim 2, I made several predictions about shifts in the kinetic properties of the fast sodium channel used in my models. These shifts could be necessary due to species differences between rats (that we recorded) and mice (that provided the characterization of GP fast sodium channel properties (Mercer et al., 2007)). Indeed, while species differences for sodium channel properties in GP neurons have not yet been shown, a recent study showed that HCN channel properties in CA1 pyramidal neurons vary between rats and mice (Routh et al., 2009). Therefore, it could be

interesting to test for potential species differences by repeating the voltage clamp experiments done in dissociated mouse GP neurons by Mercer et al using dissociated rat GP neurons, which have previously been used to characterize Kv4.2 channels (Tkatch et al., 2000). By performing such experiments, one may be able to show that the shifts in fast sodium channel kinetics that we found with our automated searches were necessary due to species differences. However, another important potential reason for shifts in channel kinetics is that fast sodium channels in slice neurons with intact dendritic trees could have a very different modulation environment from dissociated neurons which lack dendritic trees. Unfortunately, due to space clamp errors, it is not possible to characterize channel properties directly in neurons with intact dendritic trees, particularly if they are as extended as those in GP neurons. Therefore, we are unlikely to be able to experimentally determine whether the kinetic properties of the fast sodium channel vary between dissociated neurons and those recorded in slice. Additionally, in aim 2 I found that many shifts in kinetic properties were consistent for a particular neuron but were not consistent between cells. This lack of consistency could be due to the unique modulation environment that each cell experiences due to its particular history or potentially due to its position within GP. Cell to cell variability could be tested using voltage clamp protocols with dissociated neurons, although not with neurons in slice (unfortunately).

In sum, it may not be possible to develop 'gold standard' channel models which perfectly describe channels for a particular cell type. For this reason, it could be interesting for modelers of other cell types to set kinetics free (starting from the experimentally determined channel properties, of course). I predict that they will find some consistent shifts in kinetic properties away from the current experimentally based

channel models that they are using, thereby improving the biological accuracy of their models.

4.4. Limitations of Evolutionary Algorithms

In aim 2, I made extensive use of the particle swarm evolutionary algorithm in order to optimize conductance density and kinetic parameters. However, there are important issues which apply to all evolutionary algorithms that I have not dealt with. One of these issues is that no evolutionary algorithm can guarantee convergence to the globally optimal solution. Indeed, it is almost certainly the case that there exist globally optimal solutions which are better than the locally optimal solutions found by my search algorithm in aim 2. However, this problem is not limited to evolutionary algorithms: for any continuous parameter space, it is impossible to sample every possible point because there are an infinite number of them. This means that, no matter how good the solution found by a search algorithm or parameter sampling scheme, there could be a better solution which was not sampled.

Another issue with, or feature of, evolutionary algorithms is that they do not sample parameter space uniformly, as does a database approach. Evolutionary algorithms give up uniform sampling of parameter space in favor of concentrated sampling of high fitness regions, which presumably allows them to find optimized (if not optimal) solutions faster than uniform sampling approaches. Unfortunately, this behavior can leave entire regions of parameter space, which could very well contain the global optimum, unsampled. Non-uniform sampling also makes it more difficult to perform controlled comparisons of model behavior in different regions of parameter space. The

ability to perform such comparisons is a particular strength of the database approach, and if this is a desired outcome then that approach should be used in favor of evolutionary algorithms.

4.5. Reduced Modeling in the Future

In many ways, the field of computational neuroscience is still in its infancy. This is because a prerequisite for conductance based compartmental neuron modeling is computational power which has only recently become available and affordable in large quantities. Therefore, it is only recently that it has been possible to implement large networks of morphologically realistic neuron models (as in the Blue Brain project at http://bluebrain.epfl.ch/), or even large networks of models with reduced branching structures. Even as computational power continues to expand with ever increasing numbers of cores, graphics processors, or FPGAs (for instance), modelers will still be faced with the question of which level of morphological reduction to use in network models because the computational demands of network modeling can be extremely large. This is because there are many more neurons in the human brain (10-100 billion) than we will ever be likely to be able to model with any degree of realism. Therefore, the trade off between computational cost and biological realism will almost certainly still be an important issue for a long time to come. For this reason, I suspect that aim 1 of my thesis work will continue to be relevant to computational neuron modelers for the foreseeable future.

Network models using reduced or simpler models often avoid attributing emergent phenomena to dendritic processing. This is partly because of the computational

cost of incorporating full morphological models into networks and partly because of the incomplete understanding of which dendritic phenomena can be faithfully preserved by reduced models. Aim 1 of my thesis should allow modelers to more confidently decide when to incorporate reduced models into their networks. Furthermore, aim 1 of my thesis should allow network modelers to more confidently ask questions about how dendritic processing contributes to network phenomena because they will have a clearer understanding of which level of morphological reduction is ideally suited to their question.

Neural networks incorporating compartmental conductance based models often connect many identical copies of a standard neuron model due to the difficulty of generating a large diverse set of neuron models with appropriate dynamics. Parameter variation approaches, including the one that I presented in aim 2, should allow network modelers to begin incorporating a larger range of intrinsic model properties in the component models of their networks. Incorporating realistic intrinsic variability in this way should provide more realistic results from network models, which may currently be handicapped by the uniform properties of their component neuron models.

Finally, a very long term goal of computational neuroscience is the automated creation of neuron models. The methods and analyses that I present in both of my aims should contribute to our eventual ability to automatically create neuron models from experimental recordings. Perhaps this ability will manifest itself in a well designed program which can be provided with relevant experimental data. The program should be able to figure out if there are serious problems with the data, what those may be, and either figure out ways to minimize the impact of such errors or provide the

experimentalist with feedback on ways to improve their experimental design. The program should also suggest additional pieces of data that would improve its ability to make a model. Finally, the program should perform extensive self-checking on its model generation attempts, and the results of these analyses should be easily understandable by an experimentalist. We are not there yet, but one day it may be possible to generate neuron models in this way, thus allowing much greater access to neuron modeling than currently exists. Hopefully, improved access to computational models will lead to a much wider appreciation for the complexities of neural processing and an improved understanding of neural dynamics.

REFERENCES

Abbott LF (1999) Lapicque's introduction of the integrate-and-fire model neuron (1907). Brain Research Bulletin 50:303-304.

Achard P, De Schutter E (2006) Complex parameter landscape for a complex neuron model. Plos Computational Biology 2:794-804.

Allen M et al. (2003) Positional cloning of a novel gene influencing asthma from Chromosome 2q14. Nature Genetics 35:258-263.

Andreasen M, Lambert JDC (1998) Factors determining the efficacy of distal excitatory synapses in rat hippocampal CA1 pyramidal neurones. Journal of Physiology-London 507:441-462.

Antic SD (2003) Action potentials in basal and oblique dendrites of rat neocortical pyramidal neurons. Journal of Physiology-London 550:35-50.

Bar-Yehuda D, Korngreen A (2008) Space-clamp problems when voltage clamping neurons expressing voltage-gated conductances. Journal of Neurophysiology 99:1127-1136.

Bean BP (2007) The action potential in mammalian central neurons. Nature Reviews Neuroscience 8:451-465.

Burke RE (2000) Comparison of alternative designs for reducing complex neurons to equivalent cables. Journal of Computational Neuroscience 9:31-47.

Bush K, Knight J, Anderson C (2005) Optimizing conductance parameters of cortical neural models via electrotonic partitions. Neural Networks 18:488-496.

Bush PC, Sejnowski TJ (1993) Reduced Compartmental-Models of Neocortical Pyramidal Cells. Journal of Neuroscience Methods 46:159-166.

Cajal SR (1911) Histologie du Systeme Nerveux de l'Homme et des Vertebres. Paris: Maloine.

Caporale N, Dan Y (2008) Spike timing-dependent plasticity: A Hebbian learning rule. Annual Review of Neuroscience 31:25-46.

Cardoso MF, Salcedo RL, DeAzevedo SF (1996) The simplex-simulated annealing approach to continuous non-linear optimization. Computers & Chemical Engineering 20:1065-1080.

Clerc M, Kennedy J (2002) The particle swarm - Explosion, stability, and convergence in a multidimensional complex space. Ieee Transactions on Evolutionary Computation 6:58-73.

Cummins TR, Dib-Hajj SD, Black JA, Akopian AN, Wood JN, Waxman SG (1999) A novel persistent tetrodotoxin-resistant sodium current in SNS-null and wild-type small primary sensory neurons. Journal of Neuroscience 19.

Davison AP, Feng JF, Brown D (2000) A reduced compartmental model of the mitral cell for use in network models of the olfactory bulb. Brain Research Bulletin 51:393-399.

Deschutter E, Bower JM (1994) An Active Membrane Model of the Cerebellar Purkinje-Cell .1. Simulation of Current Clamps in Slice. Journal of Neurophysiology 71:375-400.

Destexhe A (2001) Simplified models of neocortical pyramidal cells preserving somatodendritic voltage attenuation. Neurocomputing 38:167-173.

Destexhe A, Rudolph M, Pare D (2003) The high-conductance state of neocortical neurons in vivo. Nature Reviews Neuroscience 4:739-751.

Destexhe A, Neubig M, Ulrich D, Huguenard J (1998) Dendritic low-threshold calcium currents in thalamic relay cells. Journal of Neuroscience 18:3574-3588.

Druckmann S, Berger TK, Hill S, Schurmann F, Markram H, Segev I (2008) Evaluating automated parameter constraining procedures of neuron models by experimental and surrogate data. Biological Cybernetics 99:371-379.

Gauck V, Jaeger D (2000) The control of rate and timing of spikes in the deep cerebellar nuclei by inhibition. Journal of Neuroscience 20:3006-3016.

Gauck V, Jaeger D (2003) The contribution of NMDA and AMPA conductances to the control of spiking in neurons of the deep cerebellar nuclei. Journal of Neuroscience 23:8109-8118.

Gentet LJ, Stuart GJ, Clements JD (2000) Direct measurement of specific membrane capacitance in neurons. Biophysical Journal 79:314-320.

Gerken WC, Purvis LK, Butera RJ (2006) Genetic algorithm for optimization and specification of a neuron model. Neurocomputing 69:1039-1042.

Golding NL, Spruston N (1998) Dendritic sodium spikes are variable triggers of axonal action potentials in hippocampal CA1 pyramidal neurons. Neuron 21:1189-1200.

Golding NL, Jung HY, Mickus T, Spruston N (1999) Dendritic calcium spike initiation and repolarization are controlled by distinct potassium channel subtypes in CA1 pyramidal neurons. Journal of Neuroscience 19:8789-8798.

Goldstein SS, Rall W (1974) CHANGES OF ACTION POTENTIAL SHAPE AND VELOCITY FOR CHANGING CORE CONDUCTOR GEOMETRY. Biophysical Journal 14:731-757.

Grieco TM, Afshari FS, Raman IM (2002) A role for phosphorylation in the maintenance of resurgent sodium current in cerebellar Purkinje neurons. Journal of Neuroscience 22:3100-3107.

Gulledge AT, Kampa BM, Stuart GJ (2005) Synaptic integration in dendritic trees. Journal of Neurobiology 64:75-90.

Gunay C, Edgerton JR, Jaeger D (2008) Channel Density Distributions Explain Spiking Variability in the Globus Pallidus: A Combined Physiology and Computer Simulation Database Approach. J Neurosci 28:7476-7491.

Hanson JE, Smith Y (2002) Subcellular distribution of high-voltage-activated calcium channel subtypes in rat globus pallidus neurons. Journal of Comparative Neurology 442:89-98.

Hanson JE, Smith Y, Jaeger D (2004) Sodium channels and dendritic spike initiation at excitatory synapses in globus pallidus neurons. Journal of Neuroscience 24:329-340.

Harmar AJ et al. (2009) IUPHAR-DB: the IUPHAR database of G protein-coupled receptors and ion channels. Nucleic Acids Research 37:D680-D685.

Herz AVM, Gollisch T, Machens CK, Jaeger D (2006) Modeling single-neuron dynamics and computations: A balance of detail and abstraction. Science 314:80-85.

Herzog RI, Cummins TR, Waxman SG (2001) Persistent TTX-resistant Na+ current affects resting potential and response to depolarization in simulated spinal sensory neurons. Journal of Neurophysiology 86:1351-1364.

Herzog RI, Liu CJ, Waxman SG, Cummins TR (2003) Calmodulin binds to the C terminus of sodium channels Na(v)1.4 and Na(v)1.6 and differentially modulates their functional properties. Journal of Neuroscience 23:8261-8270.

Hille B (2001) Ionic Channels of Excitable Membranes. Sunderland, MA: Sinauer.

Hodgkin AL, Huxley AF (1952) A quantitative description of membrane current and its application to conduction and excitation in nerve. Journal of Physiology-London 117:500-544.

Hoffman DA, Johnston D (1998) Downregulation of transient K+ channels in dendrites of hippocampal CA1 pyramidal neurons by activation of PKA and PKC. Journal of Neuroscience 18:3521-3528.

Hoffman DA, Magee JC, Colbert CM, Johnston D (1997) K+ channel regulation of signal propagation in dendrites of hippocampal pyramidal neurons. Nature 387:869-875.

Huys QJM, Ahrens MB, Paninski L (2006) Efficient estimation of detailed single-neuron models. Journal of Neurophysiology 96:872-890.

Izhikevich EM (2004) Which model to use for cortical spiking neurons? Ieee Transactions on Neural Networks 15:1063-1070.

Jerng HH, Qian Y, Pfaffinger PJ (2004) Modulation of Kv4.2 channel expression and gating by dipeptidyl peptidase 10 (DPP10). Biophysical Journal 87:2380-2396.

Johnston D, Wu SMS (1995) Foundations of Cellular Neurophysiology. Cambridge, MA: The MIT Press.

Keren N, Peled N, Korngreen A (2005) Constraining compartmental models using multiple voltage recordings and genetic algorithms. Journal of Neurophysiology 94:3730-3742.

Keren N, Bar-Yehuda D, Korngreen A (2009) Experimentally guided modelling of dendritic excitability in rat neocortical pyramidal neurones. Journal of Physiology-London 587:1413-1437.

Kita H, Kitai ST (1994) The Morphology of Globus-Pallidus Projection Neurons in the Rat - an Intracellular Staining Study. Brain Research 636:308-319.

Kuznetsov AS, Kopell NJ, Wilson CJ (2006) Transient high-frequency firing in a coupled-oscillator model of the mesencephalic dopaminergic neuron. Journal of Neurophysiology 95:932-947.

Lai HC, Jan LY (2006) The distribution and targeting of neuronal voltage-gated ion channels. Nature Reviews Neuroscience 7:548-562.

Lapicque L (1907) Recherches quantitatives sur l'excitation e´lectrique des nerfs traite´e comme une polarization. J Physiol Pathol Gen 9:620-635.

Larkum ME, Waters J, Sakmann B, Helmchen F (2007) Dendritic spikes in apical Dendrites of neocortical layer 2/3 pyramidal neurons. Journal of Neuroscience 27:8999-9008.

Letzkus JJ, Kampa BM, Stuart GJ (2006) Learning rules for spike timing-dependent plasticity depend on dendritic synapse location. Journal of Neuroscience 26:10420-10429.

Lipowsky R, Gillessen T, Alzheimer C (1996) Dendritic Na+ channels amplify EPSPs in hippocampal CA1 pyramidal cells. Journal of Neurophysiology 76:2181-2191.

Llinas RR (1988) THE INTRINSIC ELECTROPHYSIOLOGICAL PROPERTIES OF MAMMALIAN NEURONS - INSIGHTS INTO CENTRAL NERVOUS-SYSTEM FUNCTION. Science 242:1654-1664.

London M, Hausser M (2005) Dendritic computation. Annual Review of Neuroscience 28:503-532.

Losonczy A, Makara JK, Magee JC (2008) Compartmentalized dendritic plasticity and input feature storage in neurons. Nature 452:436-U433.

Maex R, De Schutter E (2003) Resonant synchronization in heterogeneous networks of inhibitory neurons. Journal of Neuroscience 23:10503-10514.

Mainen ZF, Sejnowski TJ (1996) Influence of dendritic structure on firing pattern in model neocortical neurons. Nature 382:363-366.

McCormick DA, Shu YS, Yu YG (2007) Hodgkin and Huxley model - still standing? Nature 445:E1-E2.

McIntyre CC, Grill WM (1998) Sensitivity analysis of a model of mammalian neural membrane. Biological Cybernetics 79:29-37.

Mercer JN, Chan CS, Tkatch T, Held J, Surmeier DJ (2007) Nav1.6 sodium channels are critical to pacemaking and fast spiking in globus pallidus neurons. Journal of Neuroscience 27:13552-13566.

Michels G, Brandt MC, Zagidullin N, Khan IF, Larbig R, van Aaken S, Wippermann J, Hoppe UC (2008) Direct evidence for calcium conductance of hyperpolarization-activated cyclic nucleotide-gated channels and human native I-f at physiological calcium concentrations. Cardiovascular Research 78:466-475.

Migliore M, Shepherd GM (2002) Emerging rules for the distributions of active dendritic conductances. Nature Reviews Neuroscience 3:362-370.

Migliore M, Ferrante M, Ascoli GA (2005) Signal propagation in oblique dendrites of CA1 pyramidal cells. Journal of Neurophysiology 94:4145-4155.

Myers JL, Well AD (2003) Research Design and Statistical Analysis, 2nd Edition. Mahwah, NJ: Lawrence Erlbaum Associates, Inc.

Naundorf B, Wolf F, Volgushev M (2006) Unique features of action potential initiation in cortical neurons. Nature 440:1060-1063.

Newton AC (1995) PROTEIN-KINASE-C - STRUCTURE, FUNCTION, AND REGULATION. Journal of Biological Chemistry 270:28495-28498.

Oltedal L, Veruki ML, Hartveit E (2009) Passive membrane properties and electrotonic signal processing in retinal rod bipolar cells. Journal of Physiology-London 587:829-849.

Park KS, Mohapatra DP, Misonou H, Trimmer JS (2006) Graded regulation of the Kv2.1 potassium channel by variable phosphorylation. Science 313:976-979.

Park KS, Yang JW, Seikel E, Trimmer JS (2008) Potassium channel phosphorylation in excitable cells: Providing dynamic functional variability to a diverse family of ion channels. Physiology 23:49-57.

Price K, M. SR, A. LJ (2005) Differential evolution: a practical approach to global optimization. New York, NY: Springer.

Prinz AA, Billimoria CP, Marder E (2003) Alternative to hand-tuning conductance-based models: Construction and analysis of databases of model neurons. Journal of Neurophysiology 90:3998-4015.

Prinz AA, Bucher D, Marder E (2004) Similar network activity from disparate circuit parameters. Nature Neuroscience 7:1345-1352.

Rall W (1959) Branching Dendritic Trees and Motoneuron Membrane Resistivity. Experimental Neurology 1:491-527.

Rall W (1960) MEMBRANE POTENTIAL TRANSIENTS AND MEMBRANE TIME CONSTANT OF MOTONEURONS. Experimental Neurology 2:503-532.

Rall W (1962) THEORY PHYSIOLOGICAL PROPERTIES OF DENDRITES. Annals of the New York Academy of Sciences 96:1071-&.

Rall W (1964) Theoretical significance of dendritic trees for neuronal input-output relations. In: Reiss RF, ed Neural Theory and Modeling Stanford University Press, Stanford, CA:73-97.

Rall W (1967) DISTINGUISHING THEORETICAL SYNAPTIC POTENTIALS COMPUTED FOR DIFFERENT SOMA-DENDRITIC DISTRIBUTIONS OF SYNAPTIC INPUT. Journal of Neurophysiology 30:1138-&.

Rall W (1969) Time Constants and Electrotonic Length of Membrane Cylinders and Neurons. Biophysical Journal 9:1483-&.

Rall W, Rinzel J (1973) BRANCH INPUT RESISTANCE AND STEADY ATTENUATION FOR INPUT TO ONE BRANCH OF A DENDRITIC NEURON MODEL. Biophysical Journal 13:648-688.

Rall W, Burke RE, Holmes WR, Jack JJB, Redman SJ, Segev I (1992) Matching Dendritic Neuron Models to Experimental-Data. Physiological Reviews 72:S159-S186.

Rossie S (1999) Regulation of voltage-sensitive sodium and calcium channels by phosphorylation. In: Ion Channel Regulation, pp 23-48.

Roth A, Hausser M (2001) Compartmental models of rat cerebellar Purkinje cells based on simultaneous somatic and dendritic patch-clamp recordings. Journal of Physiology-London 535:445-472.

Routh BN, Johnston D, Harris K, Chitwood RA (2009) Anatomical and Electrophysiological Comparison of CA1 Pyramidal Neurons of the Rat and Mouse. Journal of Neurophysiology 102:2288-2302.

Rubchinsky LL, Kopell N, Sigvardt KA (2003) Modeling facilitation and inhibition of competing motor programs in basal ganglia subthalamic nucleus-pallidal circuits. Proceedings of the National Academy of Sciences of the United States of America 100:14427-14432.

Rush AM, Wittmack EK, Tyrrell L, Black JA, Dib-Hajj SD, Waxman SG (2006) Differential modulation of sodium channel Na(v)1.6 by two members of the fibroblast growth factor homologous factor 2 subfamily. European Journal of Neuroscience 23:2551-2562.

Rusnak F, Mertz P (2000) Calcineurin: Form and function. Physiological Reviews 80:1483-1521.

Saltelli A, Chan K, Scott EM (2000) Sensitivity Analysis. New York, NY: John Wiley & Sons, LTD.

Schaefer AT, Larkum ME, Sakmann B, Roth A (2003) Coincidence detection in pyramidal neurons is tuned by their dendritic branching pattern. Journal of Neurophysiology 89:3143-3154.

Schulz DJ, Goaillard JM, Marder E (2006) Variable channel expression in identified single and electrically coupled neurons in different animals. Nature Neuroscience 9:356-362.

Shirahata E, Iwasaki H, Takagi M, Lin CQ, Bennett V, Okamura Y, Hayasaka K (2006) Ankyrin-G regulates inactivation gating of the neuronal sodium channel, Nav1.6. Journal of Neurophysiology 96:1347-1357.

Smith RD, Goldin AL (1998) Functional analysis of the rat I sodium channel in Xenopus oocytes. Journal of Neuroscience 18:811-820.

Srinivas M, Patnaik LM (1994) GENETIC ALGORITHMS - A SURVEY. Computer 27:17-26.

Stuart G, Spruston N (1998) Determinants of voltage attenuation in neocortical pyramidal neuron dendrites. Journal of Neuroscience 18:3501-3510.

Stuart G, Schiller J, Sakmann B (1997) Action potential initiation and propagation in rat neocortical pyramidal neurons. Journal of Physiology-London 505:617-632.

Suh BC, Hille B (2005) Regulation of ion channels by phosphatidylinositol 4,5-bisphosphate. Current Opinion in Neurobiology 15:370-378.

Tabak J, Moore LE (1998) Simulation and parameter estimation study of a simple neuronal model of rhythm generation: Role of NMDA and Non-NMDA receptors. Journal of Computational Neuroscience 5:209-235.

Takigawa T, Alzheimer C (2002) Phasic and tonic attenuation of EPSPs by inward rectifier K+ channels in rat hippocampal pyramidal cells. Journal of Physiology-London 539:67-75.

Taylor AL, Goaillard JM, Marder E (2009) How Multiple Conductances Determine Electrophysiological Properties in a Multicompartment Model. Journal of Neuroscience 29:5573-5586.

Terman D, Rubin JE, Yew AC, Wilson CJ (2002) Activity patterns in a model for the subthalamopallidal network of the basal ganglia. Journal of Neuroscience 22:2963-2976.

Tien JH, Guckenheimer J (2008) Parameter estimation for bursting neural models. Journal of Computational Neuroscience 24:358-373.

Tkatch T, Baranauskas G, Surmeier DJ (2000) Kv4.2 mRNA abundance and A-type K+ current amplitude are linearly related in basal ganglia and basal forebrain neurons. Journal of Neuroscience 20:579-588.

Tobin AE, Van Hooser SD, Calabrese RL (2006) Creation and reduction of a morphologically detailed model of a leech heart interneuron. Journal of Neurophysiology 96:2107-2120.

Traub RD, Wong RKS, Miles R, Michelson H (1991) A model of a CA3 hippocampal pyramidal neuron incorporating voltage-clamp data on intrinsic conductances. Journal of Neurophysiology 66:635-650.

Traub RD, Kopell N, Bibbig A, Buhl EH, LeBeau FEN, Whittington MA (2001) Gap junctions between interneuron dendrites can enhance synchrony of gamma oscillations in distributed networks. Journal of Neuroscience 21:9478-9486.

Trimmer JS, Rhodes KJ (2004) Localization of voltage-gated ion channels in mammalian brain. Annual Review of Physiology 66:477-519.

Urban NN, Henze DA, Barrionuevo G (1998) Amplification of perforant-path EPSPs in CA3 pyramidal cells by LVA calcium and sodium channels. Journal of Neurophysiology 80:1558-1561.

Van Geit W, De Schutter E, Achard P (2008) Automated neuron model optimization techniques: a review. Biological Cybernetics 99:241-251.

Vanier MC, Bower JM (1999) A comparative survey of automated parameter-search methods for compartmental neural models. Journal of Computational Neuroscience 7:149-171.

VanRullen R, Guyonneau R, Thorpe SJ (2005) Spike times make sense. Trends in Neurosciences 28:1-4.

Vervaeke K, Hu H, Graham LJ, Storm JF (2006) Contrasting effects of the persistent Na+ current on neuronal excitability and spike timing. Neuron 49:257-270.

Ward LM (2003) Synchronous neural oscillations and cognitive processes. Trends in Cognitive Sciences 7:553-559.

Weaver CM, Wearne SL (2006) The role of action potential shape and parameter constraints in optimization of compartment models. Neurocomputing 69:1053-1057.

Weaver CM, Wearne SL (2008) Neuronal Firing Sensitivity to Morphologic and Active Membrane Parameters. PLoS Computational Biology 4:e11.

Williams SR, Stuart GJ (2000) Site independence of EPSP time course is mediated by dendritic I-h in neocortical pyramidal neurons. Journal of Neurophysiology 83:3177-3182.

Wilson M, Bower JM (1992) Cortical oscillations and temporal interactions in a computer-simulation of piriform cortex. Journal of Neurophysiology 67:981-995.

Yelnik J, Percheron G, Francois C (1984) A GOLGI ANALYSIS OF THE PRIMATE GLOBUS PALLIDUS .2. QUANTITATIVE MORPHOLOGY AND SPATIAL ORIENTATION OF DENDRITIC ARBORIZATIONS. Journal of Comparative Neurology 227:200-213.